Materials & Design 223 (2022) 111245

Contents lists available at ScienceDirect

Materials & Design

journal homepage: www.elsevier.com/locate/matdes

Electron and laser-based additive manufacturing of Ni-based superalloys: A review of heterogeneities in microstructure and mechanical properties

Nana Kwabena Adomako, Nima Haghdadi *, Sophie Primig *

School of Materials Science & Engineering, UNSW Sydney, NSW 2052, Australia

HIGHLIGHTS

- The heterogeneities in the microstructure and mechanical properties of AM Ni-based superalloys are reviewed.
- The origins of heterogeneities are linked to the variations in thermal conditions throughout the build.
- A short case study is presented.
- Strategies to minimize microstructure heterogeneity are discussed.

GRAPHICAL ABSTRACT

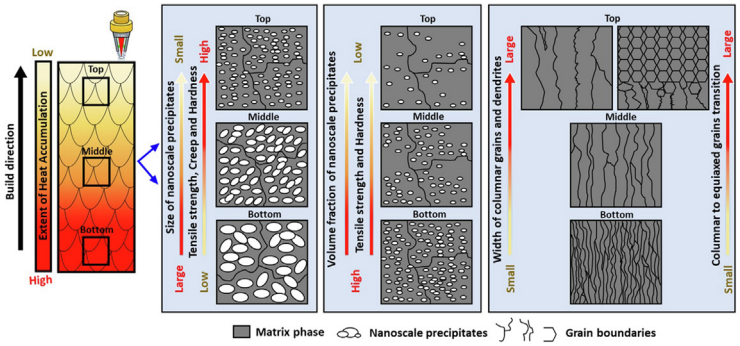

ARTICLE INFO

Article history:
Received 17 February 2022
Revised 3 October 2022
Accepted 8 October 2022
Available online 10 October 2022

Keywords:
Additive manufacturing
Ni-based superalloys
Heterogeneity
Directed energy deposition
Electron beam powder bed fusion
Laser powder bed fusion

ABSTRACT

The adaptation of additive manufacturing (AM) for Ni-based superalloys has gained significance in aerospace and power-generation industries due to the ability to fabricate complex, near-*net*-shape components on-demand and with minimal material waste. Besides its advantages, challenges remain in metal AM, especially for printing complex alloys such as superalloys. These challenges are often linked to heterogeneity in the as-fabricated parts and continue to limit the practical applications of AM products. A thorough understanding of the relationship between the complex AM process and the resulting microstructure heterogeneity needs to be established before mitigation strategies can be developed. The ability to fabricate more homogeneous Ni-based superalloy parts is expected to unlock not only better mechanical properties but also additional fields of applications.

This review aims to summarize the current understanding of heterogeneities in the microstructure and mechanical properties of AM Ni-based superalloys. Microstructure heterogeneities discussed include heterogeneity in the chemical composition, phase constitution, porosity, grain and dendrite morphology, and solid-state precipitates. Related heterogeneities in hardness, tensile, creep, fatigue, and residual stress are discussed to represent mechanical properties, and mitigation strategies are summarized. The origins of heterogeneity in the as-fabricated parts are linked to the variations in AM thermal conditions caused by the complex thermal histories.

* Corresponding authors.
E-mail addresses: nima.haghdadi@unsw.edu.au (N. Haghdadi), s.primig@unsw.edu.au (S. Primig).

https://doi.org/10.1016/j.matdes.2022.111245
0264-1275/

1. Introduction

1.1. AM of Ni-based superalloys and the resultant microstructure

The pursuit for higher performance turbine engines has necessitated the development of alloys that can endure the mechanical stresses during service at temperatures as high as 650 °C and beyond [1]. Ni-based superalloys are ideal candidates for such a purpose, owing to the exceptional combination of high strength, creep resistance, corrosion properties, and microstructural stability they offer at elevated service temperatures. They are, therefore, widely used in aircraft turbines, rocket engines, and nuclear power plants [2–7]. For example, they make up>30 % of the total weight of modern aircraft engines as they are used in many critical areas such as supporting structures, rotating structures, rotating parts, pressure vessels, and airfoils [8,9]. The common and established manufacturing methods for these parts are casting, forging, and powder metallurgy [10]. The microstructure of Ni-based superalloys consists of a face-centered cubic (FCC) γ-matrix with various solute elements. Depending on the composition and processing route, precipitates such as ordered intermetallic γ′- (Ni_3(Al, Ti)) and γ″- (Ni_3(Nb)), Laves, δ, and various carbides can be formed in the matrix [11]. Standard heat treatments techniques such as homogenization, solution treatment, and aging are often employed to eliminate compositional segregation and achieve the appropriate γ′ and/or γ″ nanoscale precipitates distribution in order to optimize mechanical properties for any particular application [12,13]. Despite the excellent properties imposed by the unique microstructure, machining of these alloys is challenging owing to their high strength and significant rate of work hardening, which causes low material removal rates and excessive tool wear. This has made fabrication of part with complex geometries via conventional manufacturing techniques of casting and forging time-consuming or sometimes even impractical [14].

3D printing which is also known as additive manufacturing (AM), nowadays allows manufacturers to produce complex, near-*net*-shape objects from a variety of alloys with minimal material waste in relatively short periods [15]. It is an advanced manufacturing technique that permits fabricating 3D components in a layer-by-layer manner using powder or other types of feedstocks. Different AM methods, namely directed energy deposition (DED), electron beam powder bed fusion (PBF-EB), and laser powder bed fusion (PBF-LB), have been used to print various types of alloys [5,16–23]. For simplicity reasons, the acronym E-PBF and L-PBF will be used throughout the manuscript for PBF-EB and PBF-LB (as defined in ASTM standards), respectively. The increased interest in metal AM in the aerospace, nuclear, and power generation industries is due to its many advantages over conventional manufacturing techniques [15,24]. Although incredible progress has been made in metal AM field to date, a complete understanding of the microstructural evolution of additively manufactured metals is currently lagging. Obtaining optimized and reproducible microstructures that consistently offer the desired in-service mechanical performance remains a significant challenge [24,25]. The majority of the as-built microstructures are often heterogeneous owing to the variation in thermal conditions (thermal gradient and cooling rates) in the build during the deposition of several layers upon each other [26–28]. For instance, there are significant variations in the non-equilibrium solidification microstructure and the solid-state phases along the build direction of parts [29–32], which may lead to heterogeneities in other properties such as mechanical, corrosion, and oxidation. Several studies have shown the heterogeneity in solidification microstructure (grain and dendrite morphologies) of AM processed Ti-6Al-4V [33–35], CoCr [36,37], 304L stainless steel [38], and IN718 [39,40]. The microstructures were generally finer at the top region compared to the bottom of builds. Heterogeneity in solid-state phase morphologies is also frequently reported. Various comprehensive studies have recently shown a heterogeneity in the distribution of nanoscale precipitates in IN738 by some of the current authors [41,42], IN718 [43], and CMSX-4 [31,44] superalloys during E-PBF which is due to thermal cycle variations. Also, for martensitic steel produced by L-PBF, the microstructure investigated consisted of a fully martensitic structure in the upper layers, while the middle and bottom regions had a high fraction of retained austenite [45]. Similar microstructure heterogeneity in phase distribution (e.g., α and β phases) has also been reported in titanium alloys [33,34].

The heterogeneity in an as-built microstructure leads to several uncertainties in the resultant mechanical and other properties. This includes non-uniformity in the distribution of strength, hardness, creep, fatigue, wear, and corrosion properties throughout a build [44,46–48]. For example, certain areas of a build will have higher strength or hardness than others. Heterogeneity in AM parts is therefore a crucial issue, limiting the widespread application of AM in fabricating critical engineering parts. Hence, a detailed insight into the mechanism of microstructure heterogeneities is needed to advance knowledge on how AM can be leveraged to fabricate parts with homogeneous and reproducible properties, and to unlock new fields of applications for AM.

1.2. Aim and structure of the review

So far, extensive effort has been made in investigating AM of Ni-based superalloys and there have been several papers reviewing this field. Most of these review papers focused on the processability of the alloys in various AM systems [5,49,50], the resulting microstructure [5,51], mechanical properties [5,8,52], defect formation [50,53], post-AM heat treatments schedules [8,51], and the effect of the AM processing parameters on the microstructure and mechanical properties [54,55]. The most comprehensive review by Attallah et al. [5] centers on the critical issues (e.g., residual stress, defects formation, and anisotropy) in AM fabricated Ni-based superalloys by discussing the key challenges, proposing mitigation methods, and outlining directions of using AM to tailor the microstructure. This valuable review, however, has not looked at the heterogeneity in microstructures and their impact on the mechanical properties. In most other reviews, the most common Ni-based superalloy, IN718, has been the sole focus of attention where authors have investigated its microstructural features, followed by a summary of the mechanical properties (tensile strength, fatigue strength, hardness, and high-temperature creep behavior) of AM IN718 for different types of AM techniques and various process and post-processing conditions [8,54,56,57]. Similarly, the heterogeneity in microstructures, which is also of critical importance, is discussed in less detail. To the best of our knowledge, the only reviews available on this important aspect of AM have focused on titanium alloys [58,59] and stainless steels [59] with a limited comprehensive evaluation of heterogeneity currently existing on Ni-based superalloys. Hence, the current review intends to fill this gap by summarizing recent studies on AM Ni-based superalloys to fully understand the heterogeneity in microstructure and its corresponding effect on mechanical properties. This paper mainly concentrates on the heterogeneity in microstructure properties such as the dendritic structure, grain morphology, porosity, chemical composition, phases formed during solidification, and the solid-state precipitates. The heterogeneity in mechanical properties discussed includes hardness, tensile, creep, and residual stress where there are enough data in the literature. Anisotropy in mechanical properties such as creep, tensile,

and fatigue is also discussed since the microstructure of AM Ni-based superalloy is significantly different in directions parallel and perpendicular to the build direction. However, the detailed effects on properties such as corrosion, oxidation resistance, and wear are not covered in this review.

The current review begins with a brief introduction on the general microstructural features of different types of Ni-based superalloys and their applications. It is followed by a brief overview of the techniques used for AM of metals, with particular focus on DED and PBF processes. A detailed assessment of published literature concerning the heterogeneity in microstructure and mechanical properties of AM Ni-based superalloys, and a case study will be provided. The review is concluded with a chapter on strategies to minimize heterogeneity.

2. Ni-based superalloys

2.1. Overview

Ni-based superalloys belong to a unique class of metallic materials that can maintain an exceptionally high strength, creep, fatigue, and corrosion resistance at elevated temperatures (usually in the range of 540–1000 °C) [5]. They are typically composed of Ni as the base element alloyed with typically 30–40 wt% of a combination of at least eight other major and minor alloying elements. Polycrystalline Ni-based superalloys are traditionally produced via casting and forming routes or via powder metallurgy. Based on the processing method, they may exhibit a variety of microstructures and, in turn, mechanical and other technological properties. Single crystal Ni-based superalloys are produced via directional solidification methods whereby the final part ideally contains only a single grain. The absence of grain boundaries gives the alloy a superior creep and thermal fatigue resistance compared to polycrystalline superalloys [60]. Ni-based superalloys are extensively used in high-temperature applications such as gas-turbines, jet engines, and other challenging environments such as chemical processing and nuclear power plants [5,61].

2.2. Constituents of Ni-based superalloys

Ni is the primary alloying element and the main constituent of the face-centered cubic (FCC) matrix phase (γ). Fig. 1a displays the elements typically alloyed with Ni to create a superalloy. Al and Ti provide the potential for precipitation hardening mechanism as they contribute to forming a coherent intermetallic phase, Ni_3(Al, Ti) (γ'), with an ordered $L1_2$ crystal structure [62]. When present, Ta can replace Al in γ' and serve as a γ' strengthener [63]. Examples of γ'-strengthened alloys include CM247, Rene148, IN738, CMSX-4, Rene N5, and Mar M247. Nb is added to some Ni-based superalloys (e.g. IN718 and IN625), where it plays a similar role as Al and Ti through the precipitation of the Ni_3Nb (γ'') intermetallic phase with a $D0_{22}$ structure [64,65]. High-volume fractions of either or both phases in their respective alloys are desirable for high temperature strengthening.

During aging treatments, the precipitation of γ' and γ'' occurs in the solid-state upon cooling of the supersaturated solid solution of γ–matrix below the respective equilibrium solvus temperature [66]. This indicates that the rate at which the alloy cools will determine the precipitation and growth kinetics of γ' and γ''. A higher cooling rate results in a unimodal distribution of fine γ' or γ'' precipitates, whereas a slower cooling rate promotes the precipitation of multiple populations of these precipitates. γ' form mostly in spherical shape and transform into cuboidal during aging, whereas γ'' form as plate-like particles. The precipitation kinetics of γ' is faster than that of γ''. Also, γ' are stable up to temperatures close to the melting temperature of the alloy compared to γ'', which are metastable and may transform to δ with an orthorhombic $D0_a$ structure at elevated temperatures (>850 ℃) [11,62].

Additions of Al, Cr, La, Y, Ce, and Mo typically enhance the oxidation and corrosion resistance by forming protective oxide layers [3]. Cr, Fe, Co, V, and Mo are usually added as solid solution strengtheners. Other elements may be introduced in small amounts to control the grain structure, which may improve mechanical properties at elevated temperatures. These include B, C, Ta, Ti, Mo, Hf, W, and Cr, which form borides and carbides and tend to segregate at the interfaces [67,68]. These secondary phases are formed during solidification and aging treatments and must be carefully controlled since they can lead to cracking and other issues under certain circumstances (e.g., hot tearing). Adding excessive refractory elements such as Nb, Mo, Re, and W promotes the precipitation of hard intermetallic Topologically Closed Packed (TCP) phases (e.g., μ, σ, and Laves) and the δ phase [69–71]. These phases are primarily formed in the aged condition and large fractions of them are generally considered detrimental to mechanical properties because they consume γ' and γ'' precipitation elements from the γ-matrix, and serve as a source for crack-initiation during cyclic loading [72–74]. Fig. 1b shows a schematic of the microstructure of a typical Ni-based superalloy depicting γ', γ'', and δ phase after direct aging as reported in [75] by some of the current authors.

2.3. Types of Ni-based superalloys

Some of the most common Ni-base superalloys discussed in this review, along with information on their composition and selected applications, are listed in Table 1 [1,2,10,77,78].

3. Metal additive manufacturing

Metal additive manufacturing (AM) is an advanced manufacturing technique enabling the fabrication of metallic components with intricate geometries from three-dimensional (3D) model data. It is also known as 3D printing, freeform fabrication, rapid prototyping, layer-based manufacturing, digital fabrication, or automated fabrication [15]. AM has recently gained substantial interest in both industry and academia, with its global market value forecast to grow at a rate of 14.4 % from $8.35 billion in 2019 to reach $23.75 billion in 2027 [79]. For leading aerospace and automobile manufacturers such as Mercedes, Airbus, and Volkswagen, AM is remarkably-well adopted for producing small, complex, and lightweight components [80]. Among the first researchers who developed AM were Brown et al. [81] in 1979 and Chuck Hull [82] in 1983. They describe AM as a process for depositing successive layers of material, one on top of another following a certain design pattern. A computer-aided design (CAD) program is used to draw the design pattern, which is then translated into model data. The model data is transferred to the 3D printer, which slices it into several finite layers with instructions on where to deposit material in each layer. The feedstock material is usually metallic powder or wire, which is melted or sometimes sintered using a highly focused heat source, and metallurgically bonded to the previous layer [83]. The heat source can be an electron or laser beam.

3.1. Metal additive manufacturing techniques

Metal additive manufacturing can be categorized into several methods based on the feedstock used for the manufacturing. Two of the most versatile methods include the powder bed fusion (PBF) and directed energy deposition (DED) processes. The PBF

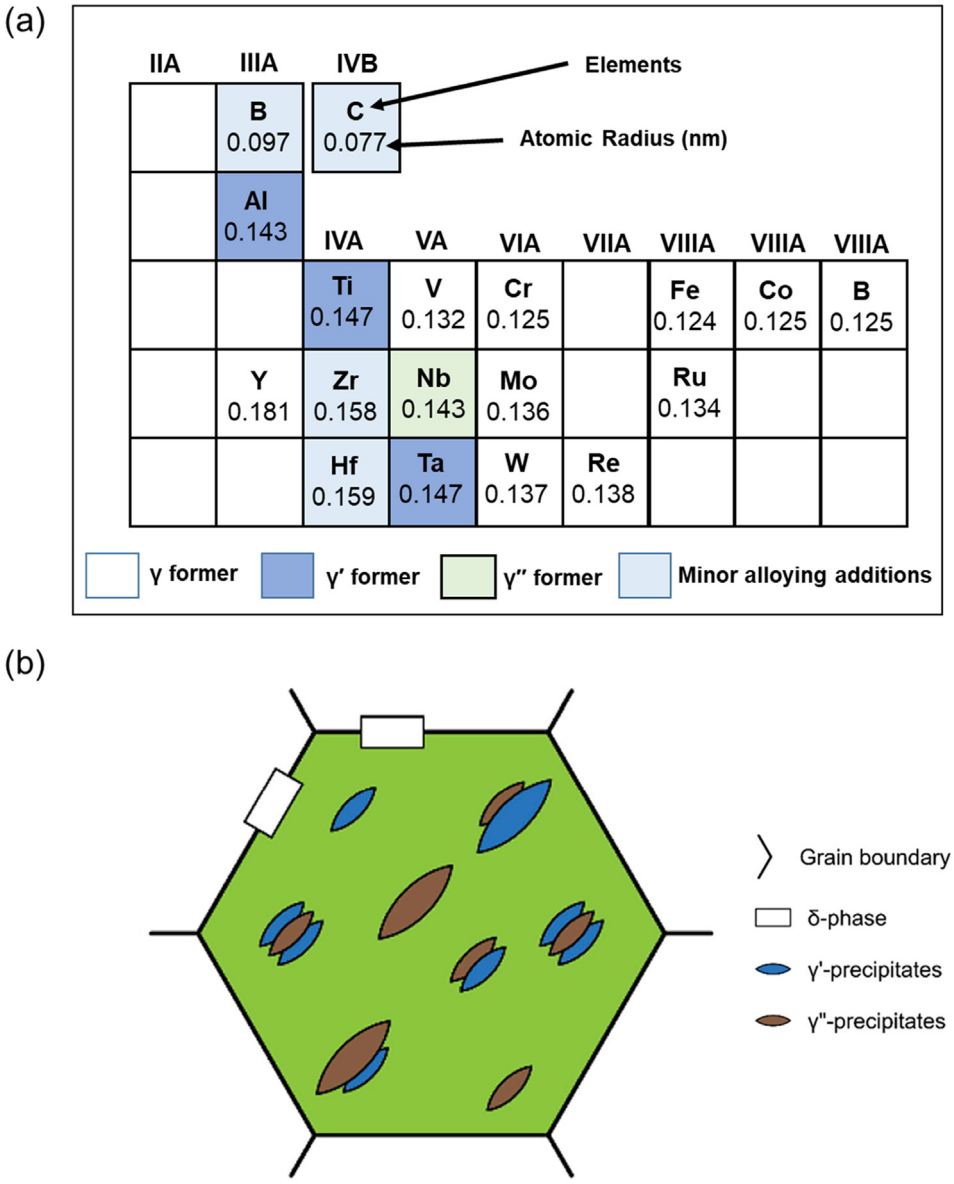

Fig. 1. (a) Alloying elements present in Ni-based superalloys. (b) Schematic showing the distribution and morphology of typical phases in the microstructure of a typical Ni-based superalloy (e.g., IN718) after aging. (a) is adapted from Ref. [76] and (b), from Ref. [75] with permission.

route is currently the most widely used in the AM industry. In a PBF process, parts are manufactured by depositing thin layers of fine metallic powder on a platform or substrate using a distribution mechanism such as a rake [84]. A laser or electron beam source scans across this layer and melts or sinters the powder, comprising the build's first layer. Then, the building platform is lowered one layer height to spread the next layer of powder to be melted on top of the previously deposited layer. This process is repeated until the required shape is completed. A schematic of a PBF machine is shown in Fig. 2a. The common types of PBF process are Electron Beam Powder Bed Fusion (E-PBF) and Laser Beam Powder Bed Fusion (L-PBF). In the E-PBF process, an electron beam is used to melt and fuse the powder particles under a vacuum atmosphere. A powder bed temperature, depending on the material, is pre-set and maintained during deposition. Preheating is primarily used to prevent build failure caused by charging of electrons, reduce residual stresses, and to achieve sintering between the individual powder granules [85,86]. For Ni-based superalloys, this temperature is around 1000 °C [16]. The preheat causes a reduction in the cooling rate of the so-called melt pool, leading to a decrease in the residual stress in the final part. However, preheating has been reported to reduce the recyclability of the remaining powder [87]. The L-PBF process, also referred to as selective laser melting (SLM), uses a high power-density laser to melt and fuse metallic powders under an inert atmosphere. It does not employ a high preheat temperature to the powder bed and hence, the process generally has a higher cooling rate than E-PBF. There are other PBF processes (e.g., Direct Metal Laser Sintering (DMLS) and selective laser sintering) which are less common and not discussed further in this review.

In the DED process route, parts are created by the simultaneous melting and fusing of feedstock material during deposition. The feedstock metallic material is either a powder or wire passed through a feed nozzle, which is melted by a laser, electric arc, or electron beam source. In the current review, unless explicitly specified, the metallic feedstock used in the DED process is powder. The melted material is added onto the build platform while following the building path directed by the CAD model. Both the feed nozzle

Table 1
Chemical composition (wt%) and applications of selected Ni-based superalloys discussed in this review [1,2,10,77].

Alloy	Ni	Cr	Co	Mo	Nb	Ti	Al	Fe	W	C	Other
IN718	50.0–55.0	17.0–21.0	–	2.8–3.3	4.75–5.50	0.65–1.15	0.2–0.8	Bal	–	≤ 0.08	≤0.35Si, ≤0.006B
	Mainly used in aircraft engines, high-speed airframe parts, cryogenic tankage, petrochemical applications, nuclear power plants, and turbochargers for cars.										
CMSX-4	Bal	6.4–6.6	9.3–10	0.5–0.7	≤0.1	0.9–1.1	5.45–5.75	–	6.2–6.6	≤0.08	2.8–3.0-Re, 6.3–6.5Ta, 0.07–0.12-Hf
	Second generation Ni-based superalloy suitable for high-pressure blades and vanes of jet engines, helicopter engines, high-pressure turbine shrouds, and gas turbines for power generation.										
Udimet 720	55.2–59.7	15.5–16.5	14.0–15.5	2.75–3.25	–	4.75–5.25	2.25–2.75	–	1.0–1.50	0.01–0.02	≤0.02-B, ≤0.05-Zr
	Used for gas turbine hot section components.										
Waspaloy	Bal	18.0–21.0	12.0–15.0	3.50–5.0	–	2.75–3.25	1.20–1.60	≤2.0	–	0.02–0.10	≤0.1-B ≤0.12-Zr
	Jet engine applications (mostly for cast turbine disks, shafts, low-pressure rings, and seal rings).										
Rene N6	Bal	4.2	12.5	1.4	–	–	5.8	–	6.0	0.05	7.2-Ta, 0.15-Hf
	A single crystal alloy used for high pressure blades, for example used for military aeroengines.										
IN625	≥58	20.0–23.0	–	8.0–10.0	3.15–4.15	≤0.4	≤0.4	≤5.0	–	≤0.1	≤0.5Si
	Suitable for nuclear reactors and oceanographic equipment due to high corrosion resistance. Also used for structures in thermal power plants, armoring in aeroengines, and plugs in aeroengines.										
Haynes 242	Bal	7.0–9.0	≤1.0	24.0–26.0	–	–	≤0.5	≤2.0	–	≤0.03	≤0.8-Mn, ≤0.5-Cu, ≤0.03-P
	Suitable for a variety of applications in aircraft and industrial gas turbines.										
MAR-M247	Bal	8.0–8.5	9.0–9.50	0.7	–	1.0	5.4–5.7	–	9.3–9.7	0.06–0.09	3-Ta, 1.0-Hf, 0.05-Zr
	Commonly used for blades and vanes and integral wheels of APUs/helicopter engines and, turbochargers.										
IN738	Bal	15.7–16.3	8.0–9.0	1.5–2.0	0.6–1.1	3.20–3.70	3.20–3.40	≤0.05	2.40–2.80	0.15–0.2	1.50–2.0-Ta, 0.05–0.15-Zr, ≤0.015-B
	Mainly used in gas turbine blades and vanes applications.										

and heat source are mounted onto a robotic arm. The DED process is ideal for repairing high-value components with little material wastage [88]. In comparison to the PBF process, the particle size of the powder feedstock is relatively coarse to enable the smooth flow of the powder which result in much bigger melt pool size. Fig. 2b shows a schematic of the DED machine. DED processes can be categorized to laser beam-directed energy deposition (L-DED), electron beam-directed energy deposition (E-DED), and arc-directed energy deposition (A-DED).

3.2. AM processing parameters

During metal AM process, various key process parameters play a role including beam power, scan speed, scan strategy, spot size, pre-heat temperature, and energy density. These parameters vary with the material and the AM technique. During fabrication, they need to be controlled as they affect the process outcomes such as build quality (lack of fusion, porosity, defects formation), microstructure, and mechanical properties [58,89–95]. For example, the size and shape of the molten region in the build (melt pool), cooling rate, and thermal gradient during fabrication mostly depend on the scan speed, beam power, hatch spacing, powder particle size distribution, spot size, and scan strategy [96]. At the same time, the material's properties such as the thermal conductivity also play a role, for example by changes in the melt pool shape. The next paragraph briefly introduces some of these key processing variables.

3.2.1. Beam power

The beam power is a measure of the amount of energy input per unit time. For the E-PBF process, the energy input rate is measured by the input beam current (mA). The energy input rate in L-DED and L-PBF processes is the laser power and is measured in W.

3.2.2. Scan speed and scan strategy

These parameters are highly critical parameters of the AM process in terms of manipulating microstructures. Scan speed is the speed at which the energy source moves over the build platform. It has a unit of m/s or mm/s. When the scan speed is high, the energy source does not get adequate time and this may cause incomplete powder melting [15,97]. Scan strategy defines the route of the energy source in the build platform. Examples of scanning strategies used in DED and PBF include bi-directional, raster scanning, contour scanning, hybrid, rotational, and checker box.

3.2.3. Hatch spacing

It is the spacing between the centers of two adjacent beams. It is also called scan spacing or hatch distance and is expressed in units of length. During fabrication, a high hatch spacing increases the production rate as it takes less time for the beam to scan each layer.

3.2.4. Energy Density

The energy density is the total energy delivered, divided by the length, area, or volume (energy per unit length, area, or volume). It is typically expressed in J/m^3, J/m^2, and J/m, and calculated using two or more of the above-listed parameters [98].

3.2.5. Spot size

Laser or electron beam spot size is the width of the beam and is roughly proportional to the beam current. It is also called "beam diameter.".

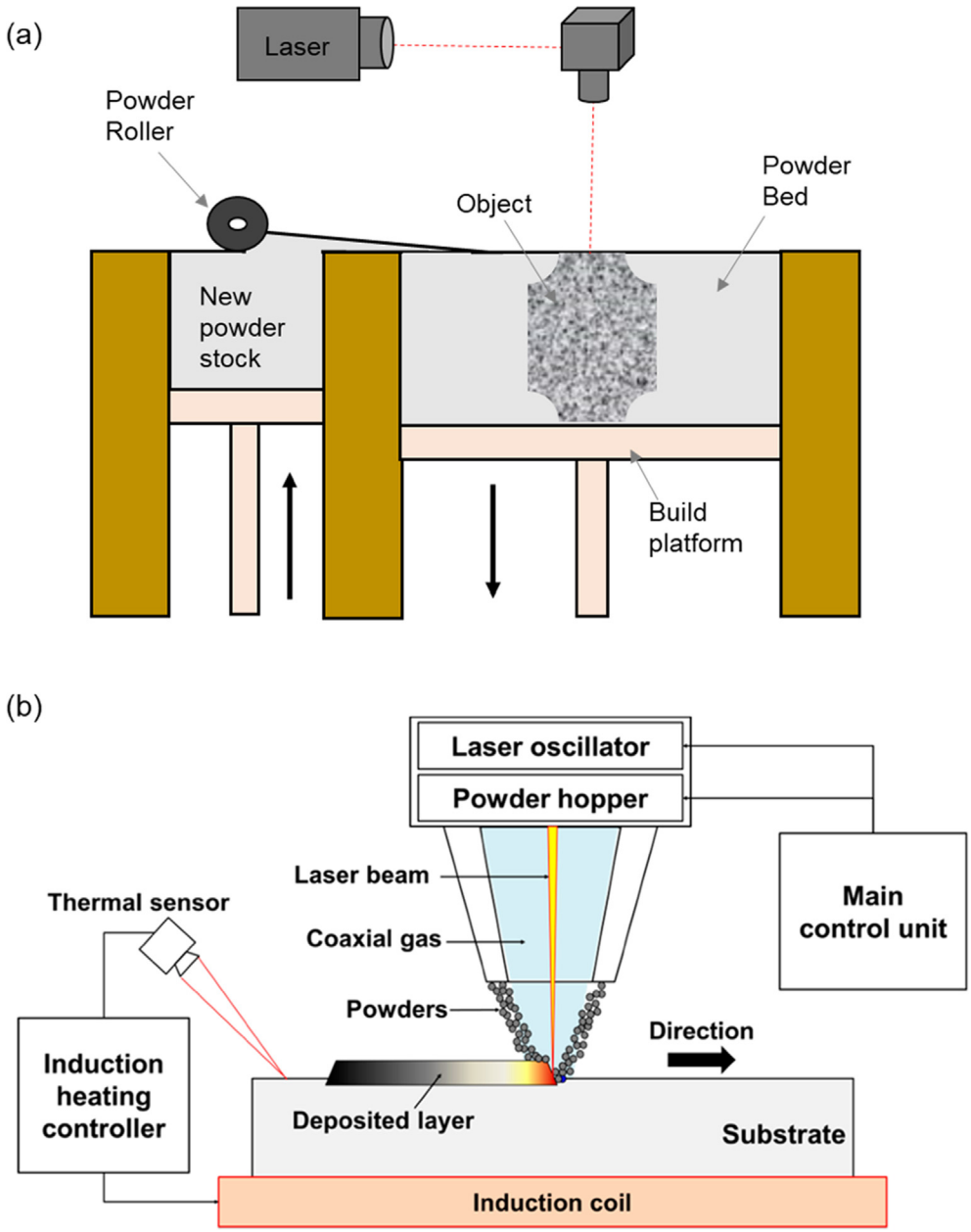

Fig. 2. Schematic of examples of (a) PBF and (b) DED processes. Adapted from Ref. [88] with permission.

3.2.6. Preheat temperature

This is the temperature of the powder bed immediately before the deposition is started, and it is kept constant until the end of built fabrication. In E-PBF, the temperature can be as high as 1200 °C dependent on the material.

3.3. Advantages and challenges of metal additive manufacturing

The advantages of AM processes include producing complex geometries close to the desired final shape, which are sometimes impossible to manufacture by the conventional manufacturing process. The rapid heating and cooling cycles further enable the fabrication of parts with refined microstructures which is sometimes laborious or even impossible to achieve via traditional manufacturing methods [99,100]. In addition, the processing steps and amount of resources needed to produce components are significantly reduced, which leads to a reduction in material wastage and eventually saves cost [15]. This also results in an increased speed of production via enabling on-demand printing of parts. Metal AM techniques, especially the E-PBF process, can act as intrinsic heat treatment and cause *in-situ* phase transformations in Ni-based superalloys, thus eliminating traditional heat treatments needed for precipitation of strengthening phases [16,41,42]. Also, the manufacturing process is flexible, and the technique can produce functionally graded materials which is ideal for the rapid exploration of new alloys [101,102].

Despite the above advantages, the AM process comes with challenges and is therefore not yet widely adopted by many industrial sectors. The challenges include the relatively low deposition rate that limits industrial adaptations for producing a high volume of parts. This is specific to PBF processes, as DED processes can overcome this limitation. Furthermore, the wide range of process parameters such as laser power, scan pattern, scan speed, and preheating makes it challenging to specify comparable experimental

conditions for different materials [103]. Also, the metallic powders used for printing are still relatively expensive. Another issue with AM is the difficulty in controlling and eliminating defects such as lack of fusion defects, inclusions, and porosities. These defects are caused mainly by the inappropriate control of the AM process parameter and the fabrication technique [104]. Also, the presence of residual stress is another challenge faced by AM components. The residual stress generation in printed components results from the large thermal gradients due to the highly localized and rapid heating and cooling [105]. The buildup of residual stress is responsible for the distortion and even failure of parts in cases where the yield strength of the material is approached. However, it has been shown that advanced scanning strategies can be used to control the thermal gradient during printing which reduces residual stresses in printed parts [106–108].

Lastly, the microstructure and resulting mechanical properties, especially in as-built Ni-based superalloy parts, are generally anisotropic and heterogeneous, which is undesirable in most applications. Anisotropy in AM refers to situations where the properties of components vary in different directions mainly due to the rapid solidification and the vertical direction of heat flow towards the substrate [109]. Regarding microstructure heterogeneity, the properties of the fabricated components most frequently vary along the deposition (build) direction. This means that important mechanical properties such as the yield and tensile strength, young's modulus, creep resistance, and ductility in an as-built component are inferior in certain regions of the built compared to others. Due to these challenges, researchers have developed a high interest in better understanding the processing-structure–property relationship in AM to improve the printing strategy and in turn the quality and reproducibility of the products to gain industry acceptance. As microstructure heterogeneity remains a critical factor in this regard, the following sections contribute to this effort by addressing the various heterogeneities and their source in the printed component of Ni-based superalloys.

4. Heterogeneity in AM Ni-based superalloys

As mentioned above, the adaptation of AM as a suitable manufacturing method for Ni-based superalloys is limited by heterogeneity in the microstructure along the build direction, which leads to heterogeneities in mechanical properties throughout a part. The microstructure heterogeneities observed in printed Ni-based superalloys include differences in the chemical composition, phase constitution, dendrite and grain morphology, and the morphology of the solid-state precipitates across a built. Variations in hardness, residual stress, creep, fatigue, and tensile properties are prominent mechanical heterogeneities observed in AM fabricated Ni-based superalloys. These heterogeneities are caused by the complex thermal cycle characteristics of different AM processes [2,5,26,27]. Additionally, the type of Ni-based superalloy plays a prominent role in these heterogeneities as certain alloys exhibit higher extents of heterogeneities compared to others, even when the same AM technique is used. The following sub-section briefly introduces the complex AM thermal cycle characteristics and how they affect the microstructure evolution.

4.1. Influence of thermal cycle characteristics on the microstructure evolution

The complex thermal cycle in AM starts with the melting and solidification of the first layer on a substrate. The heat source that accompanies the deposition of the second layer causes the previous layer to re-melt partially [110]. The previous layer is, therefore, thermally affected (and in turn subjected to a short heat treatment), which may cause solid-state phase transformations. This process is repeated for several cycles until the final layer is deposited. AM components experience non-equilibrium solidification owing to the fast-cooling rates [111]. The high cooling rate in AM is due to the small melt pool size, which leads to a shorter solidification time compared to other fusion joining processes such as welding. The solidification microstructure of AM Ni-based superalloys therefore generally consists of fine dendrites, micro-segregated elements, and solidification phases such as Laves and carbides [99,100,112]. The dendrite arm spacing is a critical microstructure feature that affects the segregation behavior and the precipitation of secondary phases within interdendritic regions. It is mainly determined by the extent of heat emission at the solidification interface during solidification [113]. A faster heat emission, equivalent to a high cooling rate, promotes small dendrite arm spacing. A small dendrite arm spacing is characterized by fine or discrete secondary phases, low elemental segregation, and fine precipitates, which are beneficial to mechanical properties. In contrast, large dendrite arm spacing under a low cooling rate produces a coarser microstructure.

Due to differences in the operation condition, the microstructures of AM Ni-based superalloys are process dependent. For example, during solidification, cooling occurs rapidly at a high rate of 10^3 to 10^4 K/s for L-DED, 10^4 to 10^6 K/s for E-PBF, and 10^5 to 10^8 K/s for L-PBF in a small localized volume [15,26,114]. The higher cooling rate of the PBF processes compared to DED is due to the more rapid scanning and smaller melt pool size. Therefore, the solidification microstructure in DED is coarser than that of PBF processes. A coarser dendritic structure (large dendrite arm spacing), Laves phase, and micro-segregation of elements are usually observed in these microstructures [115]. Within PBF processes, the high preheat temperature in E-PBF leads to a much lower cooling rate than that of L-PBF [15,26]. In E-PBF, due to the elevated preheat temperature (>1000 °C), parts usually undergo longer aging at high temperatures, which promotes the dissolution of secondary phases such as Laves, micro-segregated element, and homogenization of elemental distribution [116].

The upward layer-wise deposition leads to a variation in the thermal conditions within a build. This is responsible for most of the heterogeneities in as-built Ni-based superalloys. For instance, the cooling rate during deposition varies along the build height. A higher cooling rate and thermal gradient are usually achieved for the bottom layers than for the top layers [117]. This is due to the direct contact of the bottom layers with the build substrate plate, leading to a faster heat transfer rate at the bottom. An increase in distance from the substrate increases the difficulty of heat transfer from the melt pool into the substrate. This result in a larger melt pool and high peak temperatures at the upper layers leading to a slower cooling rate. Therefore, the top layers exhibit coarser microstructures with coarser dendrites, a higher percentage of Laves phase, a thick and continuous Laves network, and a higher degree of segregation of elements in comparison to those of the bottom layers. It should also be noted that the uppermost layer of some printed materials may experience a faster cooling rate than the middle layers [40].

There is a transition of dendrite and grain morphology from columnar at the bottom to equiaxed at the top [118]. The above-mentioned heterogeneities mainly occur in DED due to slow cooling rate and high deposition rate. This has also been occasionally seen in L-PBF, but only to a very limited extent in E-PBF. The high preheat temperature in E-PBF causes a slight change in cooling rate and thermal gradient along the build. Intentional variation of parameters which influence the thermal condition, such as scan speed, scan strategy, and beam power during deposition, have been reported to cause such variations in E-PBF microstructures [39,92]. The high susceptibility of the DED process to columnar

to equiaxed transitions can also be attributed to the high deposition rate, leading to inadequate melting of feedstock (powder or wire). This causes heterogenous nucleation within the melt pool, promoting fine equiaxed grains alongside the columnar grains. Among the DED processes, wire-based DED is likely to exhibit high heterogeneity due to the very high deposition rate, forming a large melt pool and slow cooling rate [119].

After solidification, previously deposited layers are thermally affected by the heat introduced during the deposition of several successive layers, causing a complex thermal history in each voxel. The thermally affected layers undergo a solid-state transformation if the temperature and exposure time fall within the solid-state phase transformation window. The bottom layers are exposed to more thermal cycles than the layers at the top, leading to a gradient along the build height. In Ni-based superalloys, this gradient in thermal exposure of layers leads to a gradient in the size and distribution of strengthening γ' and γ'' precipitates [31,32]. For DED and L-PBF, there is a variation in the volume fraction of strengthening γ' and γ'' precipitates. However, in certain conditions such as a low deposition rate and high cooling rate for DED and L-PBF respectively, no significant phase transformation occurs [120]. For E-PBF, the intense thermal cycle due to the elevated build temperature leads to a significant variation in the morphology and size distribution of γ' and γ'' [121,122]. Extent of heterogeneities is also influenced by the type of Ni-based superalloy, which is discussed later in the manuscript.

The following sections provide an overview of the existing observations of heterogeneities in the microstructure and mechanical properties of Ni-based superalloys fabricated with AM.

4.2. Microstructure heterogeneity

The heterogeneity in the as-fabricated microstructure of Ni-based superalloys is usually manifested by the heterogeneity in the dendritic structure, grain morphology, chemical composition, porosities, and phases formed during solidification, and the solid-state precipitates:

4.2.1. Dendrite structure

Additively manufactured Ni-based superalloys and other alloys commonly form a fine dendritic solidification microstructure, although cellular and planar front solidification have also been reported based on solidification conditions [16]. The dendritic structure, which is also observed in welding and casting processes, may be equiaxed, columnar, or of a mixed morphology depending on the AM processing parameters such as laser/electron beam power, scan speed, scanning strategy, spot size, powder feed rate, and preheat temperature [90–93]. A sub-grain cellular structure, defined by segregation of alloying elements and a network of dislocations at their boundaries, can be found within the dendritic structure [29,123–125]. The generally accepted mechanism for its formation is via thermal stress, which develops due to the local rapid heating/cooling cycles. Fig. 3a shows a solidification map, which is made using a combination of thermal gradient (G) and liquid (L)-solid (S) interface velocity (R= $\dot{T}$/G) [126]. $\dot{T}$ is the cooling rate. The solidification map is used to decide what structures can form during solidification. The mode of solidification is defined by the ratio G/R while the scale of the solidification microstructure is governed by the product G×R [127].

Fig. 3b-h depicts the different modes of solidification (i.e., planar, cellular, and dendrite) of a typical Ni-based superalloy. The figure shows the quenched S/L interface morphologies of CMSX-10 at various solidification rates during directional solidification. Planar S/L interface forms at the slowest solidification rate and high temperature gradient. With a gradual increase in solidification rate (decrease in G/R value, Fig. 3a), the S/L interphase morphology of the alloy changes from planar to cellular, and from cellular to dendrite. A further increase in the solidification rate leads to a dendritic structure with well-developed secondary dendrite arms. Cellular and dendritic microstructures are obtained over most commercial directional solidification processes. There has been no significant commercial interest in plane front superalloys due to their high processing cost [128]. In AM, due to the fast cooling, the planar solidification front is unstable, and the solidification structure is mainly dendritic or cellular. This is proven in the work of Blecher et al. [129], where it is shown that the G/R values during AM are far below that of the lower limit for planar solidification to occur. They calculated the G/R values at mid-length and mid-height along the longitudinal mid-section of L-PBF IN718 in the range of 20 Ks mm to 100 Ks mm^{-2}. The minimum G/R value necessary for planar solidification to occur is estimated by Kou [126] as 7000 Ks mm^{-2}. Increasing G×R values leads to coarser microstructures [15].

Fig. 4a and b show typical microstructures of AM IN718 with fine columnar dendritic morphologies [131] and sub-grain cellular dislocation structures [132]. This microstructure is much finer than an as-cast microstructure which is attributed to the rapid cooling rates [111]. In general, during solidification, local changes in the cooling rate and thermal gradient will alter the dendritic structure, which can affect the size and morphology of phases such as Laves and the distribution of micro-segregating elements. A coarser dendritic structure is mainly observed at lower cooling rates, while a more refined dendritic structure is observed at higher cooling rates [112]. The dendritic microstructure of AM fabricated Ni-based superalloys will therefore exhibit substantial heterogeneity due to different solidification or cooling rates at various locations throughout the AM build (especially along the build height).

Wang and Chou [117] confirmed this by comparing the microstructure of the top layer of IN718 during L-PBF to the middle and bottom layers. They report an increase in the dendrites' width with build height due to this cooling rate variation. A comparably high cooling rate is usually reported during the initial stage (layers) of the fabrication process, which decreases with build height. The high cooling rate at the initial layers results from the higher heat conduction between the substrate and melt pool. Fig. 4c shows a typical variation of cooling rate vertically throughout the build of L-DED IN718, which is computed from the primary dendrite arm spacing in [115]. The cooling rate decreases with an increment in build height. In another study, it has been shown that the primary dendrite arm spacing of IN718 fabricated with E-PBF increases along the build height, as seen in Fig. 4d, which is also due to the faster heat conduction at the bottom compared to the top layers [43]. Similar observations are also reported in [133,134] for L-DED. In instances where the uppermost layer experience a faster cooling rate compared to the immediate middle layers, a change in the dendrite structure transition occurs. An example is depicted in [40], where the average width of the dendrite in the middle layers of a printed Ni-based superalloy decreases from 147 μm to 113 μm at the topmost layer due to its faster cooling rate compared to the middle. The width of the bottom layer is 75 μm. The top layers are in direct contact with the chamber environment since they are formed closer to the end of the deposition process. Therefore, direct exposure to the environment contributes to the higher cooling rate.

The reason for these variations has been explained by Kumara et al. [112] during their investigation of the effect of cooling rate and thermal gradient on the dendritic structure and Laves phase formation in IN718 alloy fabricated with L-PBF. They hypothesize that increasing the cooling rate causes the amount of undercooling encountered by the liquid within each period to increase. A high undercooling will generate a high excess free energy in the liquid that is eventually used up by the created liquid–solid (L-S) inter-

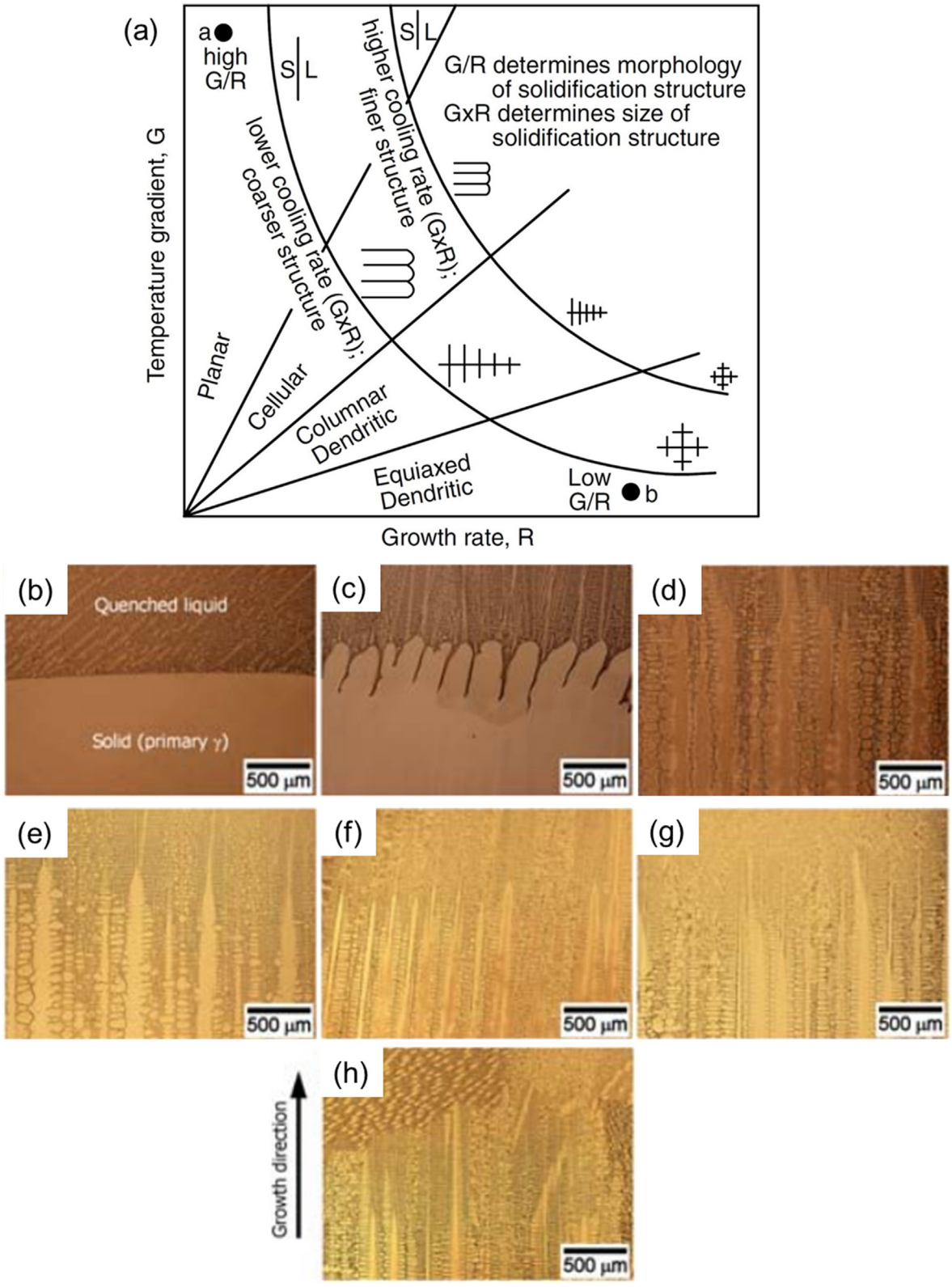

Fig. 3. (a) Effect of G and R on the morphology and size of solidification microstructure. The S/L interface morphologies of CMSX-10 quenched at various solidification rates with an increase in solidification rate from (b) to (h). The solidification rate is (b) 0.5 μm/s, (c) 1.0 μm/s, (d) 5.0 μm/s, (e) 10 μm/s, (f) 25 μm/s, (g) 50 μm/s, and (h) 100 μm/s. The morphologies of the interface changed from (b) planar to (c) cellular, and to (d) – (h) dendritic with an increase in solidification rate. (a) is adapted from Ref. [15,126] and (b-h) adapted from Ref. [130] with permission.

face through nucleation or growth. The continuous increase in extra free energy progressively creates more L-S interfaces per unit area, resulting in a finer dendritic structure. An opposite sequence occurs for a comparably slower cooling rate.

The columnar to equiaxed transition (CET) of dendritic structures is another source of microstructure heterogeneity in AM Ni-based superalloys. This transition usually takes place due to the variations in solidification conditions with build height. An

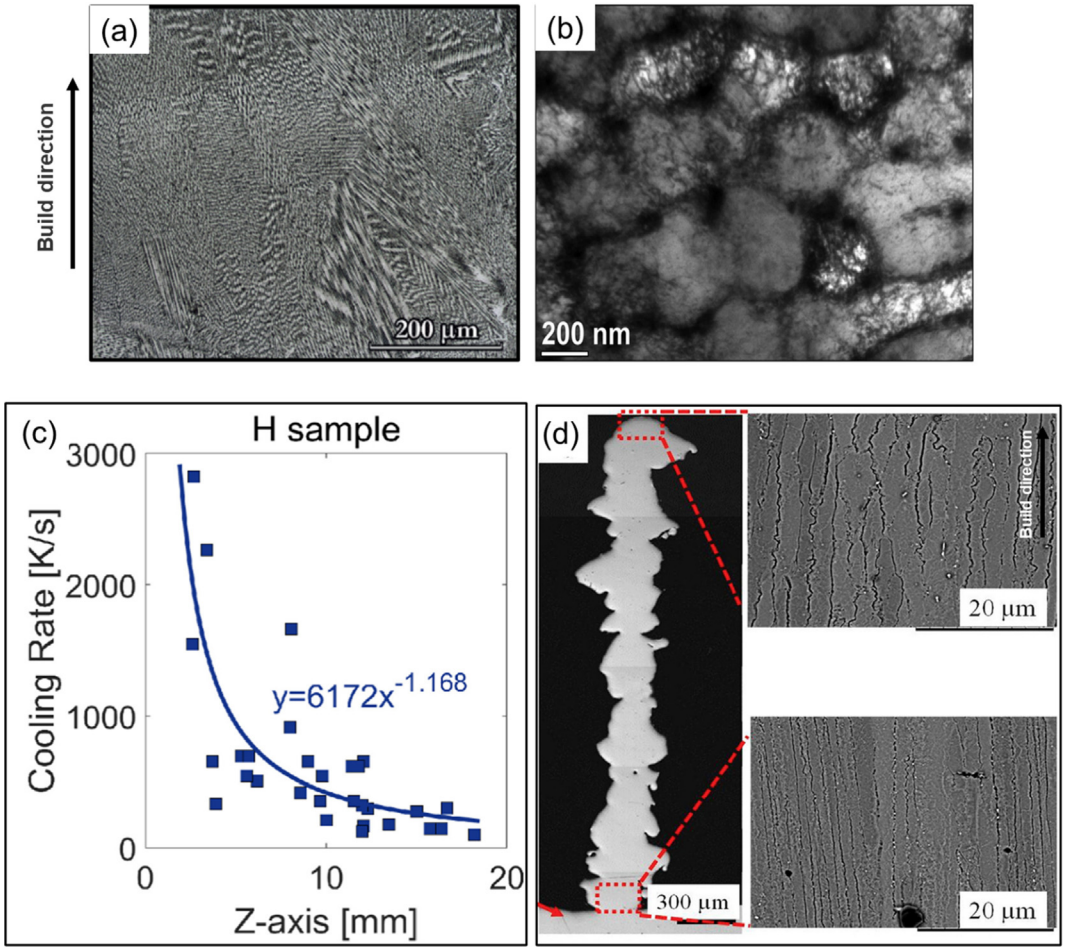

Fig. 4. (a) Microstructure of IN718 showing fine dendrites after L-DED, (b) sub-grain cellular dislocation structures in L-PBF IN718. (c) The computed cooling rate along the build of IN718 showing a decreasing trend. (d) High magnification scanning electron microscopy (SEM) images of the primary dendrite arm spacing in the top and bottom layer of IN718 build fabricated with E-PBF. (a) is adapted from Ref. [131], (b) is adapted from Ref. [132], (c) is adapted from Ref. [115], and (d), adapted from Ref. [43] with permission.

example of such transition or non-uniform microstructure can be seen in Fig. 5 for a high Cr Ni-based superalloy fabricated with L-DED [118]. The microstructure consists of epitaxially grown columnar dendrites at the middle and bottom regions in both longitudinal and transverse directions, whereby the top area consists of equiaxed dendrites. The columnar to equiaxed transition occurs due to the lower temperature gradient in the upper layer, resulting in a smaller G/R value.

4.2.2. Grain morphology

In metal AM, unique grain morphologies are created due to the layer-by-layer material deposition, rapid solidification, and heat loss towards the substrate (thermal gradient direction) [5]. Grains are mostly columnar and extend across many re-melt layers [51,135,136]. Single crystal type microstructures are desirable for components operating at elevated temperatures. However, such parts are susceptible to cracking, especially during laser-based processing, where minimal preheating is applied [24,137]. Also, columnar grains are responsible for the anisotropy in the tensile and creep behavior of some printed DED components using a wire feedstock [109]. This is similar to the tension/creep behavior of directionally solidified Ni-based superalloys like DS200 + Hf [138]. Alongside columnar grains, fine equiaxed grains may be embedded within columnar grain regions depending on the solidification conditions, such as the cooling rate ($\dot{T}$), thermal gradient (G), and liquid–solid interface velocity (R= $\dot{T}$/G) [91,92,126]. This is similar to that of the dendritic structure.

During AM, there is a spatial variation of G and R in the melt pool since the heat source is moving, which may lead to a variation of solidification mode [139,140]. This variation implies that some regions, especially at the melt pool surface, will experience a low G/R ratio inducing equiaxed grain formation besides the primary columnar grains formed in high G/R regions. This microstructure heterogeneity, i.e. the presence of both columnar and equiaxed grains, has been witnessed in several AM studies. For example, in an L-PBF fabricated CM247LC Ni-based superalloy (Fig. 6a), growth of columnar grains towards the melt pool and along the build direction is reported while some regions show equiaxed grains [18]. Also, the use of a chessboard scanning strategy during L-PBF of CM247LC resulted in equiaxed grains embedded within the regions of primarily columnar grains [135]. This heterogeneity in grain morphology is also observed in other both L-PBF and E-PBF fabricated Ni-based superalloys, and is attributed to local alterations in the solidification conditions during deposition [92,93,135,141,142].

Further, significant differences in the size and width of columnar grains along the build direction is another microstructural heterogeneity usually observed in the microstructure of AM fabricated Ni-based superalloys. A typical example is observed in a non-weldable Ni-based superalloy fabricated with E-PBF, where the

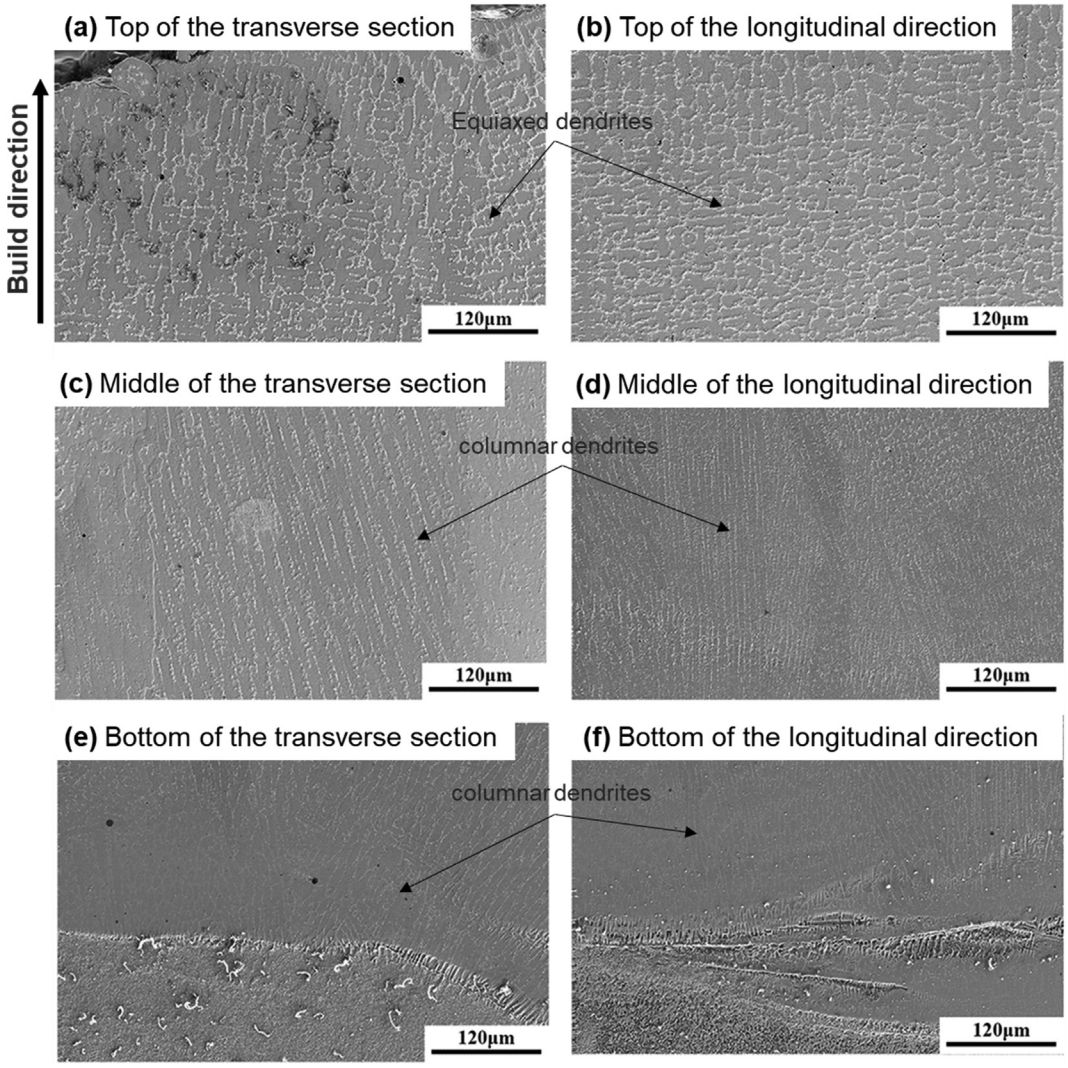

Fig. 5. SEM images of L-DED K648 superalloy at the transverse and longitudinal directions indicating dendritic structure changes along the build height. (a), (b) Equiaxed dendrites at the top of the build while (c), (d) and (e), (f) reveal columnar dendrites at the middle and bottom region, respectively. Adapted from Ref. [118] with permission.

width of the epitaxially grown columnar grains increases along the build direction and across several layers [44]. This is shown in Fig. 6b where the width of the columnar grain increases from ~ 30 μm at the bottom to 150 μm at the middle of the build. At the top layer, a substantial increase in the grain width to ~ 1 mm is observed. Correspondingly, the grain boundary density has been reported to decrease from the bottom to the top of the build, as shown in the plot in Fig. 6c. The regions with higher grain boundary density are characterized by a reduction in the degree of compositional segregation, while the lower grain boundary density regions exhibit an increase in the degree of compositional segregation during solidification. The gradient in the width of the columnar grains is similar to that observed in Bridgman's technique for single crystal growth, which is solely based on directional solidification [143]. In the AM microstructure in Fig. 6b, the relatively small columnar grains in the first few layers result from the initial melting of powders and heat flow away from the melt pool, through the substrate [135]. The deposition of subsequent layers causes the columnar grains to grow epitaxially and competitively across several layers [144]. Also, it should be noted that each previously melted layer acts as a seed for the subsequently deposited layers to grow and expand further epitaxially [44]. Similar heterogeneity in columnar grain size along the build is seen in a study by Helmer et al. [129] using E-PBF, which authors attributed to the growth competition between grains with different orientations.

The columnar grain microstructure formation observed in [44] (Fig. 6b) has also been attributed to the applied printing parameters. Chauvet et al. [145] were able to produce fine equiaxed grains or columnar grains with smaller width (<100 μm) in the same alloy simply by changing the build parameters [145]. Manipulating the AM processing parameters may significantly influence the solidification conditions and affect the grain morphology. This is proven in the study by Raghavan et al. [93], who developed a plot of the spatiotemporal variation of the G vs R on the solidification map of IN718 for different values of processing parameters. These plots were attained based on the analytical model for the columnar to equiaxed transition in casting processes by Hunt [146], which was extended by Gäumann et al. [27] using the Kurz-Giovanola-Trivedi (KGT) model for rapid solidification processes. The sensitivity of G and R with respect to different processing parameters is shown in Fig. 7. Increasing the pre-heat temperature, beam current, spot-ON time, and beam diameter moves the microstructure from the columnar towards the equiaxed region in the map by reducing the temperature gradient. Based on this, several authors have reported heterogeneities in grain morphology of Ni-based

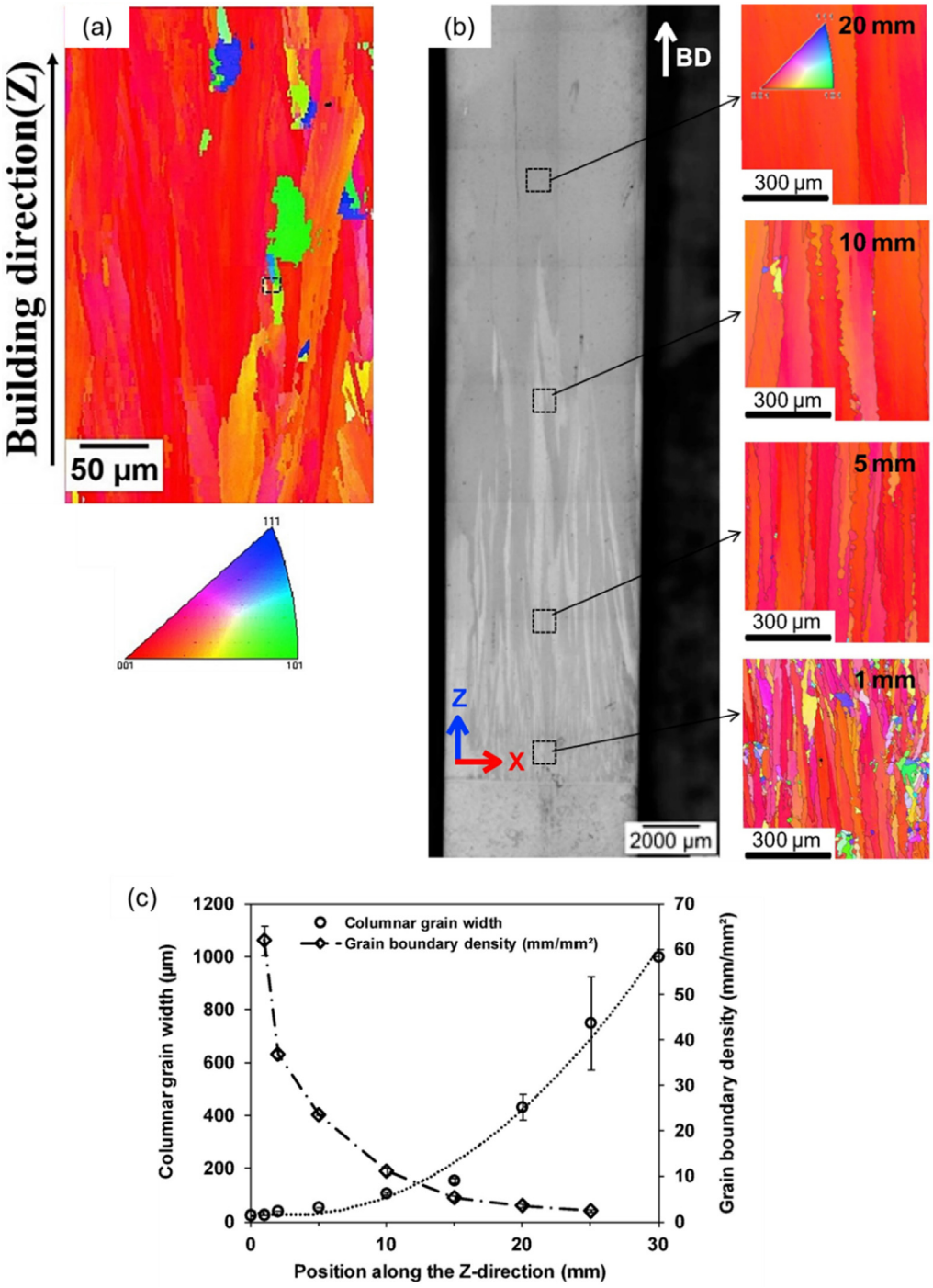

Fig. 6. (a) Electron backscatter diffraction (EBSD) maps of as-fabricated CM247LC showing columnar grains growing towards the melt pool along the build direction with regions of equiaxed grains. (b) Optical micrograph and EBSD inverse pole figure (IPF) maps of an as-built high γ′ superalloy showing the columnar grain size evolution along the build direction. (c) Evolution of the columnar grain width and grain boundary density along the build direction of (b). (a) is adapted from Ref. [18], and (b), (c) from Ref. [44] with permission.

superalloys fabricated with E-PBF by simply changing process parameters. Fig. 8a shows the microstructure of E-PBF fabricated IN718, where a significant variation of the grain structure is observed [39]. It changes from columnar to equiaxed and back when the scanning strategy changes after the 40th layer. This alters the direction of the thermal gradient during solidification. In another study, Popovich et al. [17] used L-PBF to fabricate functionally graded IN718 by changing the laser scanning strategy and laser source parameters. As seen in Fig. 8b, these authors report a transition from fine grains to coarse grains. Also, during E-PBF of IN718, changing the scanning strategy from raster to a multi-spot melting strategy, changes the grains from columnar to equiaxed morphology (Fig. 8c) [92]. The melting of adjacent domains with different strategies leads to the development of interfaces with a sharp microstructural transition [92].

Another transition in grain morphology has been observed in L-DED fabricated K465 Ni-based superalloy where columnar grains are reported in both the middle and bottom regions of the build,

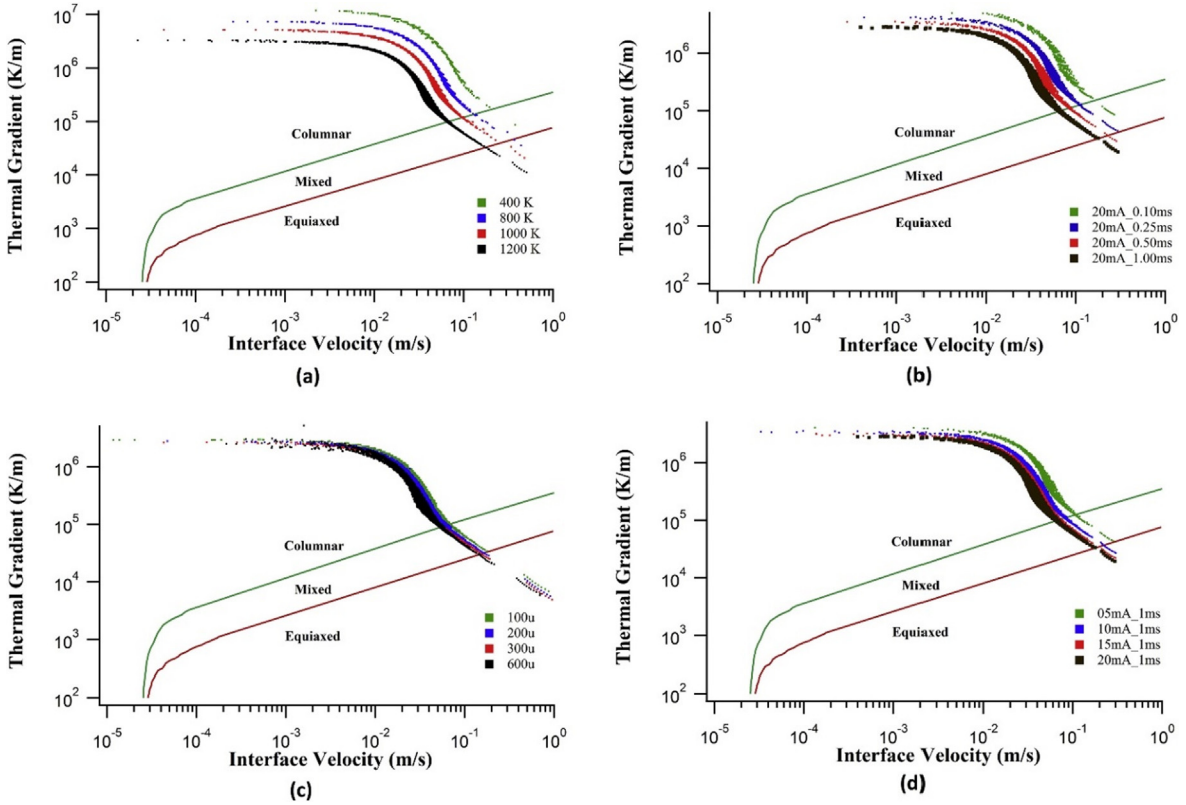

Fig. 7. Change in G and R of the melt pool as a function of (a) preheat temperature, (b) spot ON time, (c) beam diameter, and (d) spot beam current. Adapted from Ref. [93] with permission.

while equiaxed grains are seen in the top layer [147]. Fig. 8d shows a similar columnar to equiaxed grain transition for a Ni-based single crystal superalloy fabricated with L-DED [148]. The grain transition from columnar to equiaxed in the top layer is attributed to a change in solidification conditions during deposition. In the top layer, there is a decrease in temperature gradient and an increase in the interface velocity. Also, in fabricating a single crystal CMSX-4 Ni-based superalloy using L-DED, Gäumann et al. [27] observed a transition from columnar to equiaxed at the top of the build owing to a certain change in solidification conditions caused by non-remelted powder particles therein. In an L-PBF IN718 build, Liu et al. [149] used a multiscale phase field model to study the mechanism that govern CET. They attributed CET in the build to the heterogeneous nucleation due to the constitutional supercooling at the end of the melt pool and a lower G/R value. It should be noted that columnar grains generally have planar, cellular or columnar dendritic substructures while equiaxed grains have equiaxed dendritic substructures [15,59].

4.2.3. Chemical composition

Chemical (compositional) heterogeneity is a common microstructural feature witnessed in AM Ni-based superalloys. Its occurrence in AM builds is significant as it might degrade the mechanical properties and corrosion resistance, especially when the elemental loss or variation is in Cr, Nb, Al, and Ti [150,151]. Compositional heterogeneity in AM build originates mainly from the processing condition during solidification or, under certain circumstances, heat induced by the high preheat or substrate temperatures. The following paragraph elaborates on these three sources of chemical composition heterogeneity in AM builds:

In an AM build, there is a high possibility for the loss of certain elements during deposition, which depends on the processing condition or the type of alloying element in the fabricated material. In cases where a high vacuum atmosphere is created, highly volatile elements tend to evaporate [87], leading to an elemental loss in AM builds. In addition, a high laser power density or deposition rate, coupled with the several re-melting cycles, could lead to evaporation. The evaporation of elements is quite common in Ni-based superalloys due to the wide melting range created by multiple alloying elements [152,153]. Fig. 9 shows the vapor pressure as a function of temperature for various elements in Ni-based superalloys. It shows that Al, Cr, Fe, and Co are prone to vaporize first in the superalloy system. Mukherjee et al. [154] reported Cr as the element to evaporate significantly in IN625 using the Langmuir equation model for DED. Panwisawas et al. [155] used inductively coupled plasma optical emission spectroscopy (ICP-OES) alongside combustion techniques to measure the elemental loss of different Ni-based superalloys after AM. Al, Co, and Cr were found to vaporize easily in the build with individual loss of up to 1.2 at% compared to other elements.

As different regions across a build each experience a unique thermal history, it is expected that the variation in chemical composition due to vaporization will be location-specific and vary along the build height. The use of optimized processing parameters such as the scanning speed and laser power density during AM will help alleviate the vaporization of highly volatile elements. Also, another possible solution is to adjust the feedstock composition by adding excess of highly volatile elements [158]. The compositional heterogeneity that occurs during solidification of AM Ni-based superalloys is based on the degree of elemental segregation. During solidification, the degree of segregation of alloying elements is based on each element's partition coefficient in the matrix, and is alloy specific [159,160]. Fig. 9b shows a plot of the partition coefficient of elements in the matrix of various Ni-based superalloys such as IN738, WASPAOY, IN718, and CMSX-4. Elements with partition coefficients lower than one are mostly enriched in the liquid,

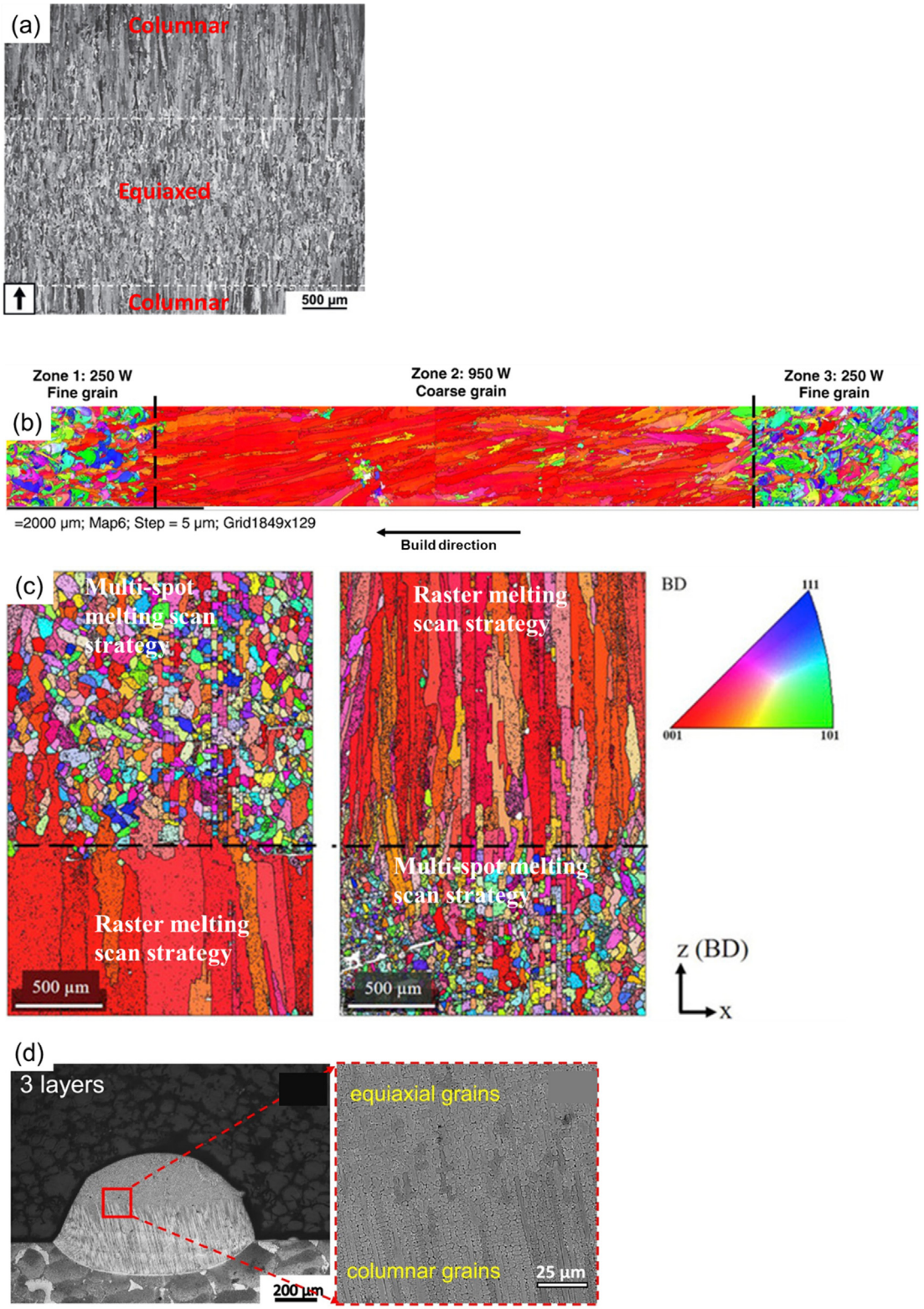

Fig. 8. (a) Local variation of the grain structure from columnar to equiaxed grains and back in a L-DED IN718. (b) EBSD analysis of a graded IN718 sample featuring a single coarse columnar grained zone embedded into a fine-grained matrix. (c) EBSD map showing local variations in grain structure in E-PBF IN718 by changing the scanning strategy (from raster to multi-spot melting strategy and back). (d) Cross-section view of the columnar to equiaxed grain transition of a Ni-based single crystal superalloy fabricated with AM. (a) is adapted from Ref. [39], (b) is adapted from Ref. [17], (c) is adapted from Ref. [92], and (d), adapted from Ref. [148] with permission.

whereas those with values higher than one or close to one are enriched in the solid during solidification. For example, in IN718, elements such as Mo, Nb, and Ti tend to segregate into the liquid, whereas Co, Al, Cr, and Ni get trapped in the γ–matrix.

Figure 10a-j shows SEM images and electron probe microanalysis (EPMA) maps of the dendritic regions of IN718 fabricated with L-DED [161]. EPMA reveals the segregation of Nb and Ti to the interdendritic regions, whereas the Ni, Cr, and Fe are concentrated

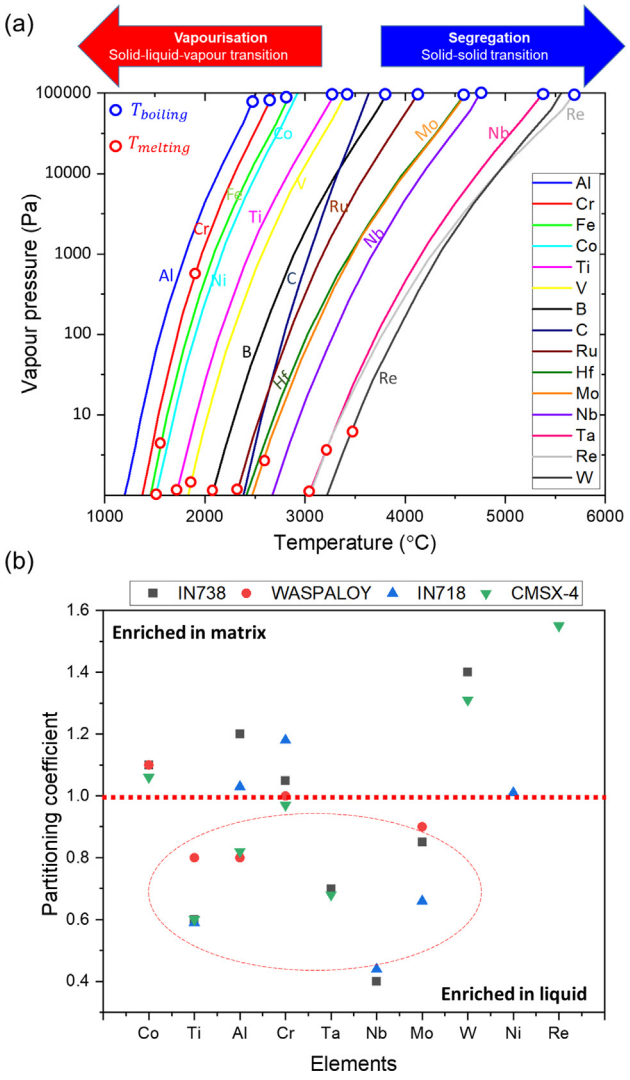

Fig. 9. (a) Vapor pressure as a function of temperature for major elements of Ni-based superalloys. (b) A plot of the partitioning coefficients of alloying elements in the matrix phase of a few selected Ni-based superalloys. (a) is adapted from Ref. [155], and (b) from Refs. [156,157] with permission.

in the core of each dendrite. The degree of elemental segregation or chemical partitioning is highly dependent on the local solidification conditions, such as the cooling and solidification rates. A rapid solidification or cooling rate causes more solute to be trapped in the core of the dendrites since there is insufficient time available for diffusion from the solid to the liquid phase. This results in a lower degree of elemental segregation in the interdendritic regions. As the cooling rate during fabrication varies with build height, the degree of elemental segregation will also change. This has been confirmed in [117], where authors measured the volume fraction of Laves phase along the build height of IN718 after L-PBF. They observed an 1 at.% increase in the volume fraction of Laves in the top of the build compared to the bottom, which is mainly ascribed to the much higher degree of Nb segregation to the interdendritic regions in the top section compared to the bottom. A similar case is also observed for a L-DED IN718 build where the Nb content in the dendrite core decreases along the build direction [115]. The Nb content decreases from ~ 4 wt% in the bottom to ~ 2.8 wt% in the top layer. The distribution of Mo in the build is expected to behave similarly as it is also segregated to interdendritic regions and contributes to Laves phase formation.

The *in-situ* heat treatment that the material experiences during E-PBF may also cause chemical heterogeneity in the microstructure of Ni-based superalloys. During E-PBF, the powder bed temperature is usually kept at or above 1000 °C, hence each layer of the build is exposed to a specific heat treatment. This elevated temperature may change the elemental composition of the solidified microstructure through the melting of various primary phases with low melting points such as Laves in alloys such as IN625 and IN718. The melting of such phases releases elements back into the matrix which may be used for solid solution or precipitation strengthening. A typical example of compositional heterogeneity caused by an *in-situ* heat treatment is observed by Deng et al. [162], where authors measured the weight percentage of Nb in the center of dendrite cores at various distances from the top surface of the build to the bottom of E-PBF IN718. Fig. 10k shows the measured weight percent of Nb in the dendrite core (dendrite core is shown in Fig. 10*l*) from the top surface of the sample. A decrease in Nb content from the bottom of the build towards the top is observed. This variation is attributed to the extent of trapped Nb in the Laves phase released back into the dendrite during the *in-situ* heat treatment. The bottom region underwent extensive homogenization as it is directly exposed to the elevated substrate temperature when compared to the middle and top regions. The Nb content at the topmost layer (between 0 and 200 μm) is higher even though it experienced a less pronounced in-situ heating effect. This is due to the increase in solidification velocity at the top, which trapped more elements, especially Nb, inside the dendrites with lower segregation to interdendritic regions.

It should be noted due to the fast solidification rate, most E-PBF Ni-based superalloys have no secondary dendrite arms, and the primary dendrite arm spacings are about two orders of magnitude finer than in standard solidification microstructures [26]. A small equiaxed dendrite arm spacing (DAS) is beneficial for forming discrete Laves phase particles, while large columnar DAS tends to produce continuously distributed coarse Laves phase particles. This makes it possible for the build to undergo shorter homogenization heat treatments due to the elevated build temperature. However, the microstructural changes during E-PBF in-situ heat treatment are much more subtle than during traditional (post-AM) homogenization and solution heat treatments of AM Ni-based superalloys, which are much longer and cause uniform dissolution of the Laves phase, and redistribution of elements in a build. One should also consider that subjecting the build to longer hours of heat treatment may deteriorate some of the unique features of the AM microstructure, such as the elemental segregation and high dislocation content in the sub-grain cellular structure.

4.2.4. Porosities

Two types of pores (spherical and non-spherical) are generally associated with AM of Ni-based superalloys. The formation of these pores is attributed to several mechanisms, including processing gas entrapped during deposition, shrinkage during solidification, pre-existing voids in the powder, inadequate melting, and lack of fusion (LOF) between layers [163,164]. Many studies have reported the presence of these porosities in L-DED [9,165,166], L-PBF [167–169], and E-PBF [170,171] fabricated Ni-based superalloys. Spherical pores form because of gas entrapped in the powder particles during deposition or pre-exist in the powder feedstock. These gases are released during melting and get locked in the melt pool during solidification. Non-spherical pores, also referred to as LOF pores, are irregular-shaped and usually form owing to insufficient laser or electron energy density to completely melt the powder [9]. A high energy density, however, can lead to a keyhole-induced porosity that can either be spherical or irregular. Pores in AM builds are detrimental to the mechanical performance by acting

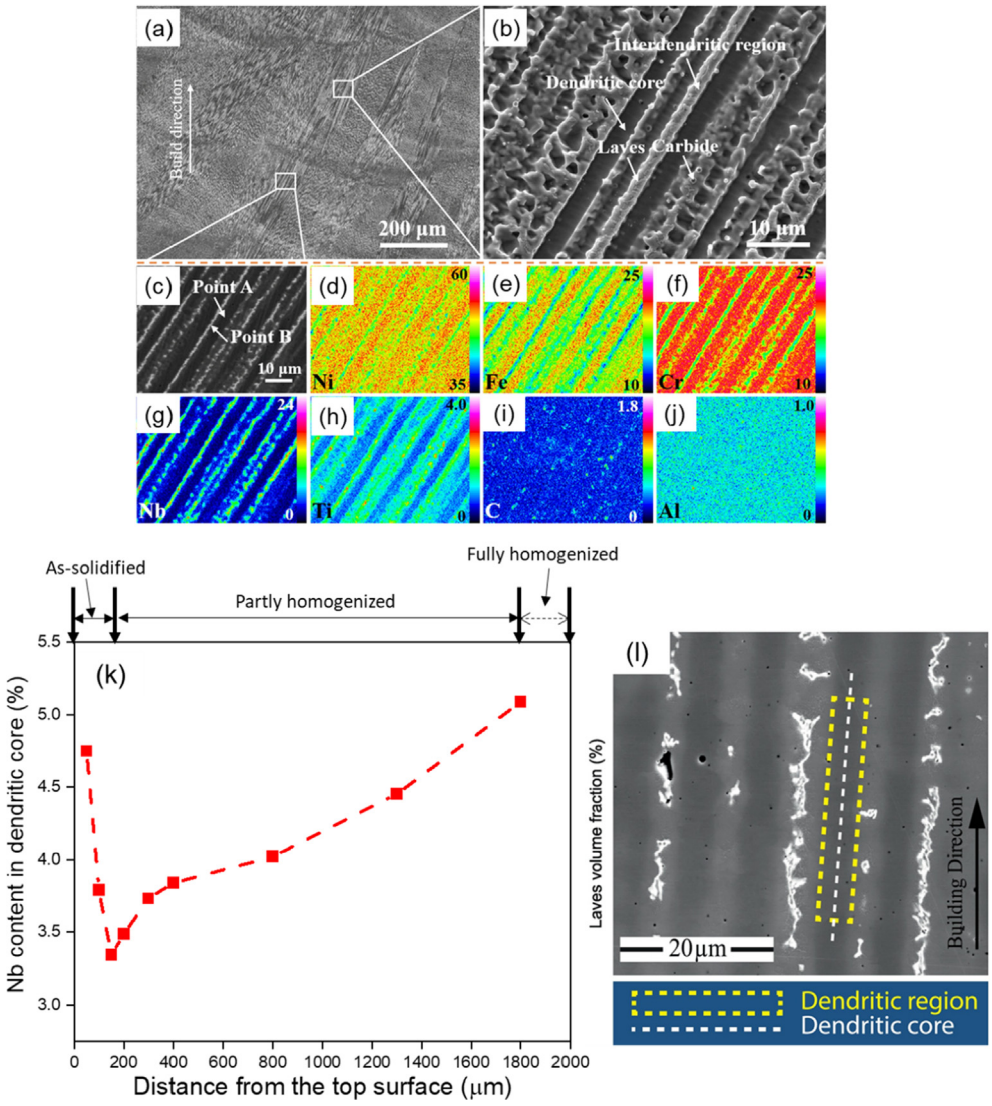

Fig. 10. (a-j) Microstructure and elemental distribution in an as-built IN718 showing elemental segregation. (k) Nb content measured at the dendritic cores of IN718 fabricated with E-PBF as a function of distance from the top surface. (l) SEM image showing a dendritic region and dendritic core where Nb was measured. (a-j) are adapted from Ref. [161] and (k) and (l), adapted from Ref. [162] with permission.

as stress concentrators. A schematic of formation of typical pores is illustrated in Fig. 11a.

The distribution of pores within AM builds is usually inhomogeneous. Spherical pores are mostly located closer to the interior of the melt pools, while LOF pores or irregular-shaped pores are found on the fusion lines between layers and at the boundaries of individual melt pools [172]. A typical example is shown in Fig. 11b, where LOF and spherical pores are distributed along the fusion boundaries and within the melt pool of a L-PBF IN718 build, respectively [163]. A similar occurrence can also be seen in [173,174]. Also, along the build height, the pore distribution is reported to vary, with the extent of variation being linked to the processing parameters. This was also seen in a study by Parmini et al. [166], where they observed a slight increase in porosity level from the top to the bottom of a L-DED IN718 build. It was ascribed to the cold substrate that led to untimely freezing of the melt pool, causing several unmelted powders at the bottom. A similar result was reported by Holland et al. [175]. However, a contrasting result is shown in [176], where the authors observed a decreasing trend in porosity towards the bottom of the build with no solid explanation for this observation.

Interestingly, the distribution of pores along the edges of builds is reported to be much more pronounced in some studies [169] and minimal in others [166], when compared to the middle. This is reasoned considering the applied laser toolpath during deposition where the application of an inside and outside contour strategy leads to regions of high porosity between the contours [169]. When using a hatched tool path, the build's edges usually remain hotter, which promotes bonding compared to the center.

4.2.5. Phase constituents

This section discusses the solid-state phase transformation and phases that form during solidification of Ni-based superalloy fabricated with AM and the various heterogeneities observed in the phase distribution in the build. The main solidification phase examined here is Laves which is mostly observed in IN718 superalloy. The nanoscale precipitates are the phases mainly observed during solid-state phase transformations. This section is concluded with a review of thermal cycles in AM of Ni-based superalloys.

4.2.5.1. Phases formed during solidification. AM processed samples undergo a predominantly non-equilibrium solidification process

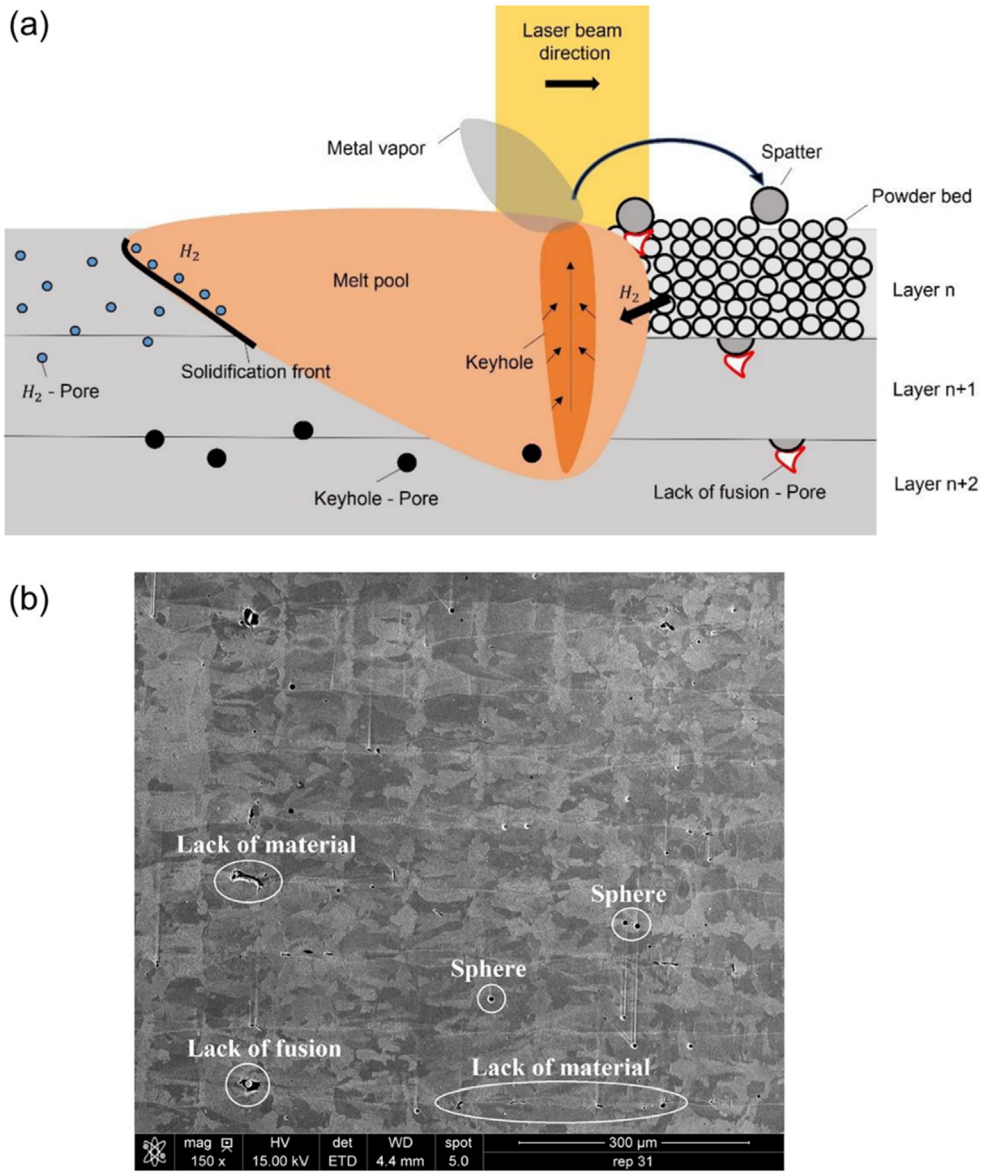

Fig. 11. (a) Schematic of the formation of gas-induced, lack of fusion, and keyhole pores during L-PBF. (b) SEM micrographs showing the different types and distribution of defects of L-PBF IN718. (a) is adapted from Ref. [177], and (b) is adapted from Ref. [163] with permission.

due to the high-speed cooling after deposition. For most Ni-based superalloys, multiple phase transformations occur during solidification. First, the primary γ phase is formed as the temperature drops below the liquidus temperature. In conditions where oxidation occurs during solidification, oxide particles might nucleate before the γ–matrix is fully solidified. This is detrimental to the properties [51,178]. Following this, TCP phases such as the Laves will precipitate in the interdendritic liquid regions of alloys such as IN718, IN625, and others mainly due to the presence of Nb. In addition, various carbides and sometimes borides form in the grain boundary and inter-dendritic regions [50,86,179]. As the solidification proceeds, most particles coarsen, and some small ones may dissolve.

The distribution of secondary phases, especially Laves, in the build after solidification is mostly heterogeneous, either within a grain or along the build height. Several authors report a high volume fraction of Laves phase in the middle of the build when compared to the bottom and top layers during L-DED, L-PBF, and plasma A-DED of IN718 and IN625 [180–183]. This microstructure heterogeneity is different from that of a typical as-cast microstructure during traditional manufacturing. Fig. 12a shows an example of this phenomenon where authors report a high volume fraction of Laves in the middle region compared to the top and bottom [181]. This microstructure observation is mainly attributed to the high cooling rate at the bottom and top layer compared to the middle, since the evolution of Laves phase formation depends on the local thermal history, especially the cooling rate. Also, aside from the volume fraction, the size distribution of Laves phase in a build has been reported to coarsen with the build height [19,134,183,184]. It should be noted that a higher volume fraction of Laves phase in the build tends to deteriorate the mechanical properties [185,186]. Laves phase is brittle and its formation also depletes beneficial alloying elements like Nb, Mo, and Ti. However, it is to be noted that a small amount of Laves phase in a granular morphology may improve the mechanical properties at elevated temperatures by promoting a pinning effect on cell and grain boundary migration [125,187–190].

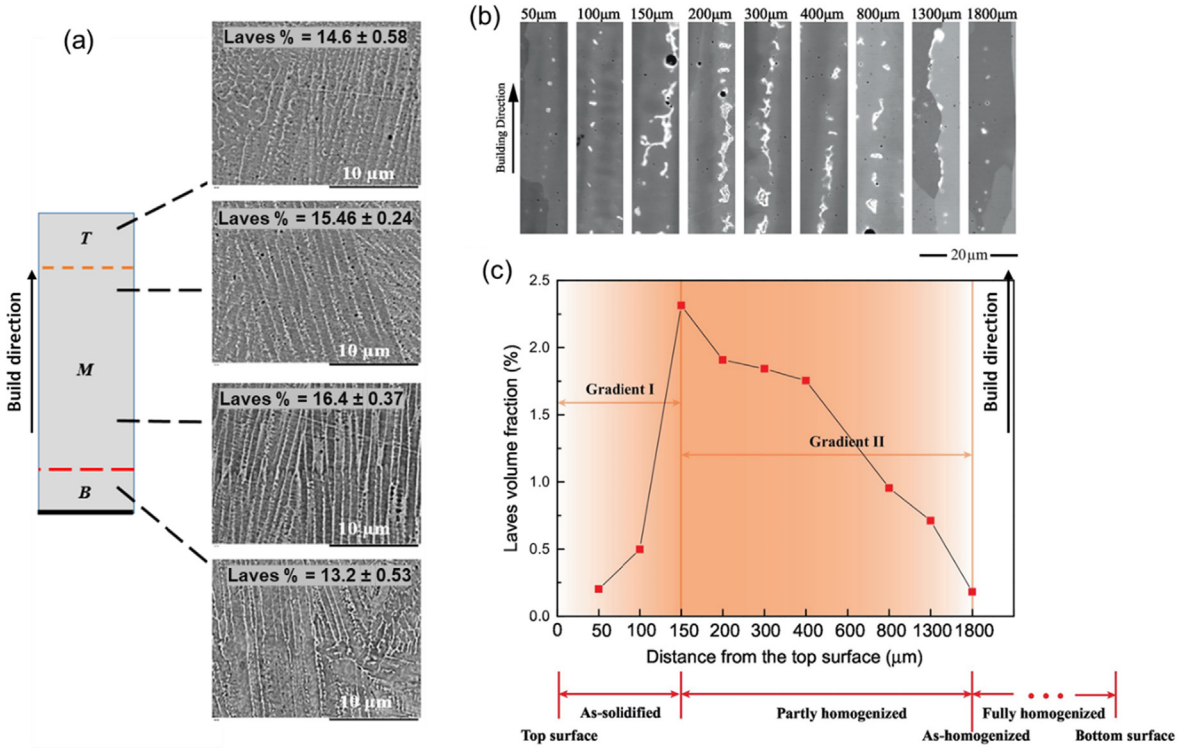

Fig. 12. (a) Laves phase fraction variation along the height of IN718 fabricated with L-DED. (b) Typical morphology and size of Laves at different distances from the top surface of IN718 fabricated with E-PBF. (c) Laves volume fraction found in the corresponding regions shown in (b). (a) is adapted from Ref. [181] and (b) and (c), adapted from Ref. [162] with permission.

The substrate preheating associated with E-PBF may also cause heterogeneity in phase distribution after solidification if the build temperature is high enough to cause melting or dissolution of selected phases. Fig. 12b-c shows the gradient in Laves morphology and volume fraction of E-PBF fabricated IN718 in different regions of the build height [162]. The Laves phase has a fine and blocky morphology of lower volume fraction close to the top surface. The size and volume fraction of Laves phase particles increases at a distance closer to the middle layers exhibiting a chain-like morphology. The chain-like Laves morphology becomes more fragmented within 500–1000 μm away from the bottom regions, and its volume fraction decreases. At the bottom where no more chain-like particles are found, the volume fraction of few blocky precipitates approaches zero. These authors attributed the gradient in Laves morphology to the corresponding gradient in *in-situ* annealing history induced by the elevated build temperature (1200 °C) of the E-PBF process. The region closer to the substrate undergoes significant homogenization compared to the regions away from the substrate. At the very top surface, the lower volume fraction is due to the increase in solidification velocity, which resulted in trapping more elements inside the dendrites, thereby reducing the formation of Laves at interdendritic regions.

A different trend in Laves phase distribution has been reported by Chandra et al. [191] in the build of an E-PBF Ni-based superalloy with a first-generation single crystal re-free composition. The authors show the precipitation of Ta-rich C14 Laves along the grain boundaries and interdendritic regions, which decrease in population density along the build direction. This phase precipitates after solidification while the layers are exposed to elevated temperatures. The higher volume fraction of the Laves phase at the bottom of the build is due to the extended periods of exposure to the high substrate temperature compared to the top. Also, in an E-PBF IN718 where the substrate temperature is set at 945 °C, a higher amount of detrimental Laves and δ phase particles is observed at the bottom compared to the middle and top of the build [192]. The low substrate temperature (945 °C), which is below the solvus temperature of Laves and δ phases, favored their precipitation. The extended periods of exposure of the bottom region to the substrate temperature led to the higher volume fractions observed at the bottom.

So far, and to the best of our knowledge, there has not yet been any report on the heterogeneity of primary phases such as carbides throughout the build. Most studies, including one by some of the current authors, show carbide distributions in AM Ni-based superalloys seem to be homogenous throughout the builds [16,42,122].

4.2.5.2. Solid-state precipitates. Immediately after the solidification of Ni-based superalloys, solid-state phase transformations occur as the temperature continues to decrease. The main phases precipitated during solid-state phase transformations are γ′ and/or γ″ nanoscale precipitates as shown in various previous studies including by some of the current authors [10,123,193]. These solid-state phase transformation processes are diffusion-controlled. In AM, the precipitation and distribution of these phases in the build is complex and heterogeneous, mainly determined by the amount of time the deposited layer spends in the nanoscale precipitates precipitation temperature window [2,5,112]. A longer holding time in a precipitation window leads to a higher phase fraction of the precipitates.

The most common microstructure heterogeneity observed after solid-state phase transformations is an increase in the volume fraction of the nanoscale precipitates away from the dendrite core, towards the area closer to the interdendritic regions [7,25,166,194]. During cooling, the nanoscale precipitates that first nucleate in the interdendritic regions grow at much higher rates compared to those within the dendritic core [112,195]. Fig. 13a-d

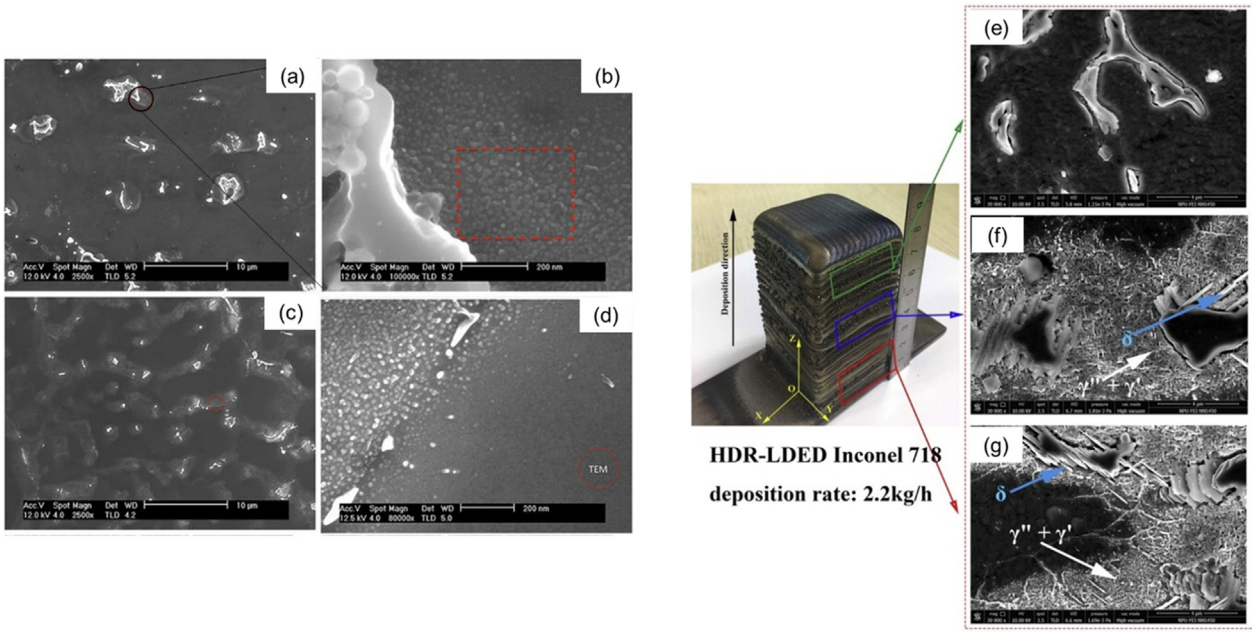

Fig. 13. (a-d) Morphology of precipitates in an IN718 fabricated with DED. (a) Low-magnification image of the top layer. (b) High-magnification image of precipitates in (a). These precipitates surround the Laves phases (lightest grey particles). (c) Low-magnification image of the bottom region showing bright contrast regions existing both near eutectic products and along interdendritic boundaries. (d) High-magnification image of the boundary between the interdendritic region and dendritic core of (a), showing a gradual decrease in particle size from the interdendritic region to the dendritic core. (e-g) Typical microstructures of L-DED fabricated IN718 samples from (e) top, (f) middle, and (g) bottom. The middle and bottom regions show higher volume fractions of γ' and γ'' precipitates than the top. (a-d) are adapted from Ref. [25] and (e),(f) from Ref. [32] with permission.

shows an example of the microstructure of L-DED IN718 where the nanoscale precipitates are distributed mainly next to the eutectic products (Laves phase in this case) (Fig. 13b) and at the interdendritic regions (Fig. 13d), compared to the core of the dendrite [25]. This microstructural feature is attributed to the high availability of γ' and γ'' forming elements (e.g., Ti, Al and Nb) in the interdendritic and adjacent regions compared to the dendrite core. This is due to the multiple thermal cycles that causes remelting and dissolution of Laves phase.

Further, a gradient in the volume fraction of nanoscale precipitates occurs along the build direction of printed superalloys due to thermal cycle variations. For the DED process, the variations in the thermal cycles through the build lead to a variation in the time a component or section spends in the nanoscale precipitates window. Li et al. [32] verified this by comparing the microstructure of the top layer of L-DED IN718 to that of the middle and bottom layers. As shown in Fig. 13e-g, these authors observed a high-volume fraction of γ' and γ'' precipitates in the bottom and middle regions of the built, while the top region exhibited a lower volume fraction of γ'' precipitates only. The high-volume fraction of γ' and γ'' in the bottom and middle is attributed to the comparably long holding time (>904 s) where the thermal cycle curve remained in the γ'/γ'' precipitation window, which is far greater than the minimum required holding time for γ' (124 s) and γ'' (57 s) to precipitate. For the upper region, a shorter holding time (88 s), which is slightly greater than the minimum holding for γ'' precipitation, is recorded, which explains the much lower degree of precipitation and growth of γ''. In the case of the γ' precipitates, the holding time is shorter than the minimum for γ' precipitation initiation, which explains the absence of this phase. This shorter holding time is a result of the lower number of thermal cycles in the top layer. Similar results are observed in [24,25,196,197].

Additionally, the thermal cycle caused by the elevated build temperature during E-PBF is known to cause a variation in the size of nanoscale precipitates distribution along the build direction. Some examples have been reported in our own previous study by Lim et al. [42] (Fig. 14 a-c), the studies by Rampsperger et al. [31] (Fig. 14 d-g), and Chauvet et al. [44], who measured the size variation of γ' precipitates along the build direction in E-PBF-manufactured high γ' Ni-based superalloys. In all these studies, the authors reported an increase in γ' size from the build top to bottom due to the *in-situ* aging treatment from the thermal cycle where layers closer to the substrate experience longer exposures. This leads to slower cooling rates and longer aging times, enabling significant coarsening of the precipitates. A similar heterogeneity in γ' size distribution has also been reported in [121,122] after E-PBF. However, in the build of E-PBF Ni-based superalloy with a first-generation single crystal re-free composition, an opposite trend in γ' size distribution has been reported [191]. An ultra-fine γ' size (~20 nm) is observed at the bottom layers compared to the top or subsequent layers (~100 nm) even though the bottom layers are subjected to longer re-heating times and have more pre-heat temperature exposure. This is ascribed to the higher cooling rate at the initially deposited layers during solidification compared to subsequent layers. The initial deposited layer is different from subsequent layers as it represents the fusion zone between the stainless-steel substrate and the build, and hence, the large volume of the substrate plate causes better heat dissipation from the first layer in comparison to the consecutive layers [191]. Also, the nanoscale precipitate distribution in most E-PBF IN718 decreases in volume fraction from the build bottom to the top [24,43,198]. This behavior is similar to that of the DED process.

Further, the thermal cycle during E-PBF is reported by some of the current authors to develop a multimodal size distribution of γ' (sizes in the range of 5–50 nm and 400–600 nm) at the middle and bottom sections of IN738 with the upper layer showing a unimodal distribution [41,42]. The formation mechanisms of these features are attributed to the occurrence of a eutectic reaction and multiple nucleation, growth, coarsening, and dissolution bursts during thermal cycling [41]. It should be noted that this same alloy (IN738)

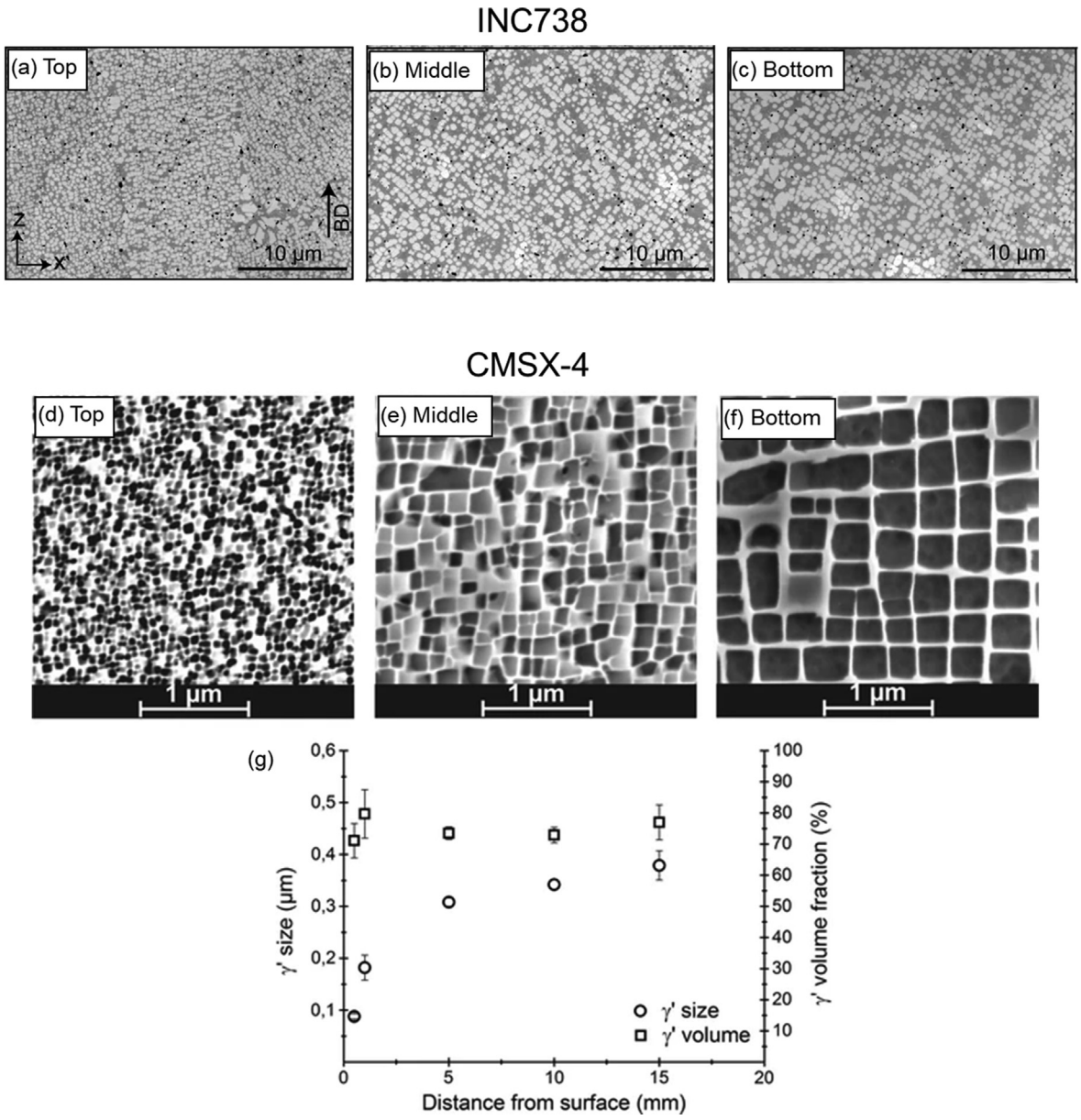

Fig. 14. Microstructures of γ/γ′ in (a,d) top, (c,e) middle, and (c,f) bottom cross-sections of (a-c) IN738 and (d-f) CMSX-4 builds fabricated with E-PBF respectively. (e) Size and volume fraction of γ′ as a function of the build height in CMSX-4. (a-c) are adapted from our own previous study Ref. [42] and (d),(e) from Ref. [31] with permission.

during L-PBF process shows no traces of γ′ precipitates in the as-fabricated state owing to the rapid-cooling rates and small thermal cycles with short duration of the L-PBF process [120].

4.2.5.3. AM thermal cycles in Ni-based superalloys. As obvious from the results discussed above, the multiple thermal cycles experienced by Ni-based superalloys during AM are responsible for the microstructure evolution, especially the solid-state phase transformation and related heterogeneities [2,5,18,25,31,32,44,112,118,121,122,133,134,162,181]. Hence, this section introduces the typical thermal cycles that Ni-based superalloys experience during AM and elaborates further on how they influence the solid-state transformation process.

Fig. 15a shows a schematic diagram of three different thermal cycles encountered during L-DED [112], and Fig. 15b illustrates typical thermal cycles for an E-PBF process [7]. In the L-DED process, thermal cycle A portrays a condition where the deposition of subsequent layers is done such that the deposited material does not experience an increase in overall temperature or heat accumulation. This means that an adequate waiting time is available for the previously deposited layers to cool down to close to room temperature before subsequent layers are deposited. Therefore, no significant phase transformation occurs in such a condition, although the temperature profile during deposition passes through the γ′ and γ″ precipitation windows. This is ascribed to the short holding time in the precipitation window. This type of thermal cycle has been observed in [199,200].

Compared to thermal cycle A, thermal cycle B does not experience an adequate waiting time between successive layers. Therefore, the deposited material's overall temperature increases due to heat accumulation from previous layers that does not have enough time to cool down. As the temperature of the thermal cycle is within the precipitation window, the previously deposited material undergoes an *in-situ* aging heat treatment, and with time, γ′

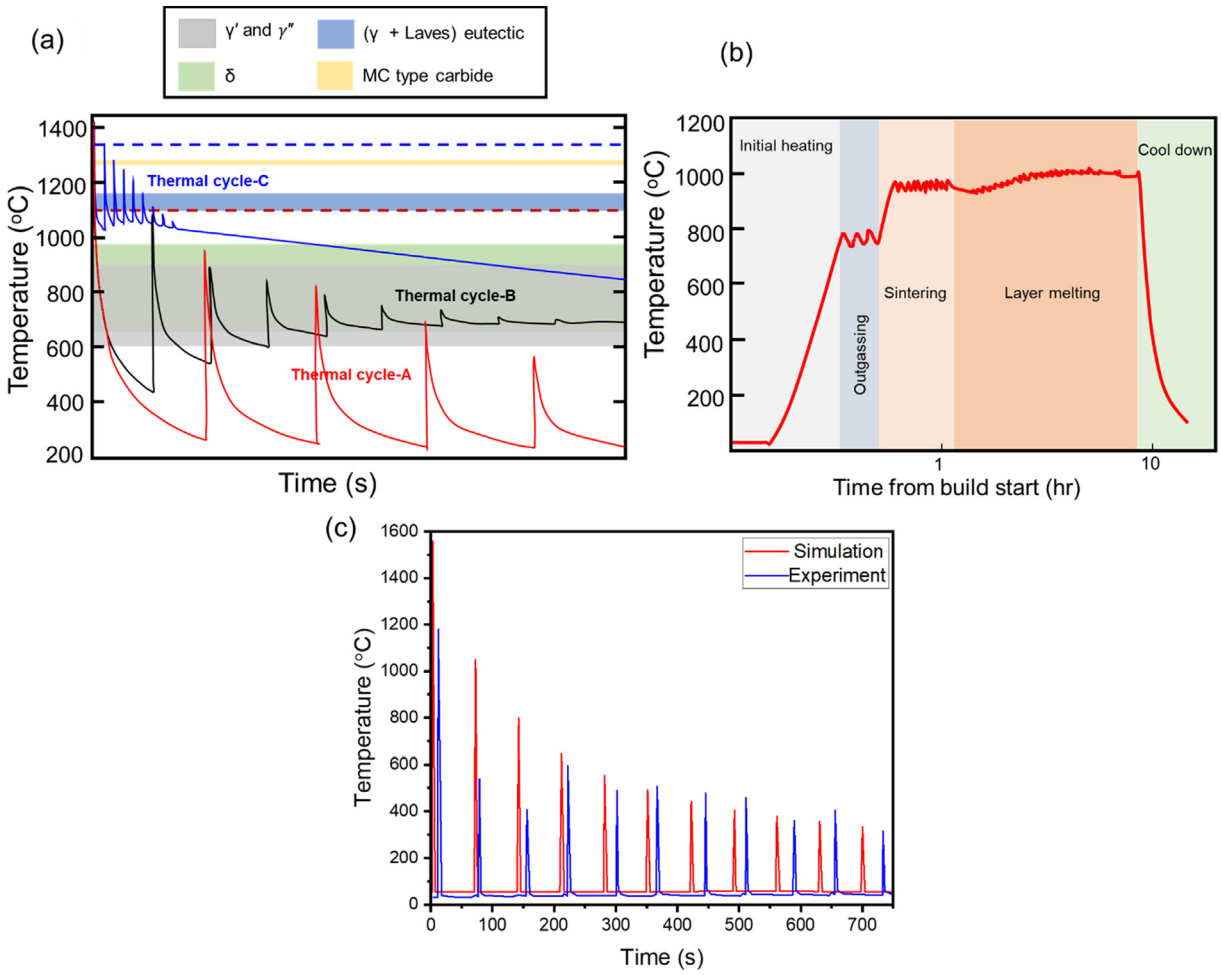

Fig. 15. Thermal cycles usually observed in (a) L-DED process and (b) E-BPF process for IN718. In the L-DED process, deposited material with thermal cycle A (shown in red) experiences little heat accumulation due to longer waiting times between successive layers. Materials deposited with thermal cycle B (shown in black) do not experience an adequate waiting time between successive layers and hence, experience higher heat accumulation. Thermal cycle C (shown in blue) experiences the highest heat accumulation due to a much higher deposition rate and lower waiting time between layers. (c) First seven cycles thermal history comparison between numerical results and experimental measurement of L-PBF IN718. (a) is adapted from Ref. [112], (b) is adapted from Ref. [7], and (c) is adapted from Ref. [210] with permission.

and γ″ begin to precipitate in the material. The growth of these precipitates depends on the duration of in-situ aging. The first 10 cycles in the work of Tian et al. [25] resembles this thermal cycle.

Thermal cycle C elucidates a scenario similar to B, with the difference being an increase in overall temperature resulting from considerable heat accumulation. A DED process with a high deposition rate usually results in such a thermal cycle. The overall temperature is kept above 1000 °C, which decreases slowly during the subsequent printing process, crossing the precipitation windows of both γ′ and γ″ precipitates. The experimentally measured temperature profile in the bottom and middle regions in a build by Li et al. [32] resembles this kind of thermal cycle. The gradual drop in temperature is due to the conduction of heat.

Thermal cycles for electron beam processes begin with the initial heating of the substrate to its outgassing temperature, which is then maintained for about 15–30 min [7,162,201]. After outgassing, heating resumes until the desired temperature for sintering is reached. Melting and deposition of materials then begin. The value for the outgassing and sintering temperature used is dependent on the alloy being fabricated. For most Ni-based superalloys, an outgassing temperature of 750 °C and a sintering temperature of 975–1200 °C are commonly used. Fig. 15b shows a typical thermal profile of IN718 fabricated with E-PBF. The heating process uses a diffuse beam that undergoes an oscillating thermal cycle to maintain the temperature. This is followed by melting of the powder and melt post-heating. Upon melting of the last deposit layer, all processes stop, and the machine starts to cool down. The E-PBF process takes a long time (5–80 hrs) to cool to room temperature after final melting [7]. It can be seen in Fig. 15b that during the deposition process, the overall temperature is high and kept close to constant value by the substrate preheating. Therefore, the melted material undergoes an *in-situ* heat treatment for a longer time than during a DED process. Also, it should be noted that the bottom layers that are closer to the substrate experience additional heating and spend a longer aging time in the desired precipitation temperature window than top layers.

Temperature measurement techniques are used to capture the discussed AM thermal cycles during printing, often for research purposes. This includes thermocouples and IR temperature sensors [202]. The thermocouple is usually connected to the substrate and has been used by different authors to measure the thermal history across AM builds [200,203–205]. For example, Segerstark et al. [200] monitored the thermal profile of L-DED IN718 by implanting thermocouple wires in the substrate. Also, the E-PBF thermal profile in Fig. 15b and thermal cycles A and B in Fig. 15a were experimentally measured using a thermocouple. IR temperature sensors perform a contactless temperature measurement of an object based on the principle that the object's infrared radiation varies

with its temperature [206]. In AM research, IR sensors have been used to monitor the melt pool behavior and the temperature distribution across a build. For example, Lane et al. [207] incorporated a commercial L-PBF machine with a thermal camera, a high-speed visible camera, and a photodiode to study the melt pool behavior of IN625.

An alternative method to obtain AM thermal cycles is through thermal modeling. This involves using various mathematical, numerical, and finite element techniques to predict the thermal cycles of AM builds [208,209]. A typical example of a study where a thermal model is used to simulate AM thermal cycle is reported in the work of Promoppatum et al. [210]. These authors used a three-dimensional finite element analysis package, COMSOL, to simulate the thermal profile and melt pool dynamics of IN718 fabricated with L-PBF. Fig. 15c shows the simulated thermal profile for the first seven cycles compared to the experimental measurement. A good correlation can be seen with slight differences, especially in the first few layers, attributed to the detachment of the thermocouple during deposition as melting occurred. A similar result can also be seen in [211], where a thermal model named simulation of additive manufacturing processes (SAMP) was used to obtain the thermal profile of a L-DED IN718. Further, thermal cycle C in Fig. 15a was acquired by performing a three-dimensional transient thermal analysis [32].

4.3. Heterogeneity in mechanical properties

The mechanical properties of AM Ni-based superalloys are strongly influenced by the resulting microstructure (such as dendritic structure, grain morphology, dislocation cell structures, porosities, chemical composition, phases formed during solidification, and solid-state precipitation) [8,18,55,57]. As heterogeneities are observed in these as-fabricated microstructures, the mechanical properties in the build are also expected to be heterogeneous. The following sub-sections summarize reports from publications on the heterogeneities observed in the mechanical properties of Ni-based superalloys fabricated with AM. The mechanical properties discussed here include hardness, tensile, Young's modulus, creep, and fatigue behavior. Residual stress is also addressed. The section is concluded with a case study. Most of these results are based on alloy IN718, which is the most used alloy in metal AM due to its high weldability.

4.3.1. Hardness

The hardness of AM fabricated Ni-based superalloys has been explored in numerous studies, e.g., after DED [25,32,118], L-PBF [46,212–216], and E-PBF [42–44,47,162]. Most of these studies have attributed the hardness evolution to the presence of strengthening nanoscale precipitates, the grain and dendrite morphology, and the dislocation cell structures. Also, the addition of nanoscale oxides or inoculants to AM microstructures can enhance the hardness [217].

The distribution of strengthening nanoscale phases contributes significantly to the high hardness in AM fabricated superalloys. Several studies report hardness values in the ranges of 300–500 HV in an as-fabricated Ni-based superalloy with in-situ precipitation of γ' particles across the build [42–44,47]. This hardness is higher than most builds without in-situ precipitated γ' particles after fabrication [215,216]. The hardness increases by ~ 30 % when the as-fabricated component is subjected to post-processing aging treatment, owing to the precipitation of more and finer γ' and γ''. In most builds with in-situ precipitated nanoscale particles, the hardness is observed to vary throughout the build height, mainly due to heterogeneity in the microstructure, as elaborated above. Table 2 shows a summary of typical hardness distributions of various AM Ni-based superalloys. For builds fabricated by L-DED and L-PBF, the hardness decreases with increasing build height. The higher hardness at the bottom of the build is ascribed to the high fraction of nanoscale precipitates. The increased precipitation rate at the bottom layers compared to the top is the result of the numerous continuous thermal cycles experienced by the bottom layers as discussed in section 4.2.5.2. Different trends in hardness evolution have been reported in other L-DED and L-PBF studies, whereby only minor changes in hardness throughout the build are observed [118,120,213,214]. This is attributed to the application of high cooling or low laser deposition rate during printing which triggers a shorter holding time in the nanoscale precipitates temperature window [30]. Builds with thermal cycle close to cycle A (Fig. 15a) usually exhibit such microstructure morphology and hardness distribution.

The average hardness of a Ni-based superalloy processed by the E-PBF process is usually higher than that of the same material processed by DED and L-PBF. This is due to the more pronounced precipitation hardening caused by the thermal cycles [16]. This means that evolution of hardening precipitates in E-PBF build is more progressed than that of L-DED and L-PBF (see Table 2). Along the build height, the hardness distribution for some E-PBF studies increases from the bottom to the top of the build. This trend in hardness is similar to that of the L-DED process discussed previously. Examples are depicted in the Refs. [24,43,198] for E-PBF IN718, where several authors report a higher hardness in the bottom regions of builds, which decreases gradually towards the top. This is ascribed to the greater degree of γ' and γ'' precipitation at the bottom compared to the top. Interestingly, in other cases [42,44,47], increases in hardness with build height have been reported. This is mainly seen for high γ' Ni-based superalloys and is attributed to the difference in γ' morphology across the build height. An example is elaborated in [47], where the authors investigated the hardness distribution in a CMSX-4 superalloy fabricated with AM. They report a lower hardness in the bottom layer, which gradually increases with the build height. This was ascribed to the larger size of γ' precipitates at the bottom compared to upper or top layers. Similar results have been reported in [44,218] and our own previous study [42]. Coarser γ' morphologies are usually characterized by a wider interparticle spacing facilitating plastic deformation of the matrix. This explains the bottom region's lower hardness [219,220]. The coarsening of γ' precipitates at the bottom area result from the longer time exposed to the elevated build temperature. The nano-hardness distribution within a specified region, grain, or melt pool may also vary in AM Ni-based superalloys [221]. For example, in the dendrite core, the hardness may be lower than that of the interdendritic region owing to the lower volume fraction of γ' and γ'' precipitates therein.

The grain or dendritic size distribution in AM builds is reported to influence the hardness distribution. According to the well-known Hall-Petch relationship, fine-grained components usually possess higher hardness owing to the higher number of grain boundaries, which hinder dislocation slip [222]. Ni-based superalloy builds with distributions of fine grains or dendrites, achieved by tuning processing parameters, exhibit higher hardness than coarser grained components. Jia et al. [223] reported an increased hardness in L-PBF IN718 after increasing the laser energy density. The main contributions to enhancing microhardness were the grain and dendrite refinement and densification upon increasing the laser energy density. A similar result can be seen in [224]. In another study, Xia et al. [124] attributed the increase in hardness in L-PBF IN718 to the finer dendritic microstructure upon increasing the scan speed. As such, heterogeneities in grain and dendritic structure due to changes in AM process parameters or solidification conditions during deposition will cause hardness variations [17,40,46,134]. The functionally graded IN718 with regions of fine- and coarse-grained microstructure observed in [17] and dis-

Table 2
Summary of hardness properties of various AM fabricated Ni-based superalloys.

Superalloy	AM Process	Load	Position of Measurement	Vickers Hardness (HV)	Reference
IN718	L-DED	200-g	Top	250	[25]
			Bottom	400	
Non-weldable Ni-based superalloy	E-PBF	1-kg	Top	475 ± 15	[44]
			Middle	425 ± 9	
			Bottom	380 ± 10	
IN718	E-PBF	500-g	Top	360 ± 5	[43]
			Middle	385 ± 2	
			Bottom	405–420 ± 5	
CMSX-4	E-PBF	–	Top	460 ± 20	[47]
			Middle	415 ± 15	
			Bottom	400 ± 5	
IN718	L-PBF	200-g	Top	325 ± 5	[46]
			Middle	330 ± 10	
			Bottom	340 ± 15	
K648 Superalloy	L-DED		Top	No variation in hardness	[118]
		500 g	Middle	(220–240)	
			Bottom		
IN718			Top	298	[32]
	L-DED	500 g	Middle	381	
			Bottom	385	
IN738			Top	4.25 ± 0.06 (GPa)	[42]
				4.04 ± 0.04 (GPa)	
	E-PBF	500 g	Middle	3.96 ± 0.04 (GPa)	
			Bottom		
IN718	E-PBF	–	Top	370 ± 5	[198]
			Middle	380 ± 10	
			Bottom	410 ± 5	
Rene-N5	E-PBF	500 g	Top	450 ± 3	[218]
			Middle	420 ± 5	
			Bottom	405 ± 5	
IN718	L-PBF	100 g	Top	250	[196]
			Middle	320	
			Bottom	355	

cussed in section 4.2.2 (Figure 8b) demonstrates this effect. The authors report a lower hardness (~280 HV) in the coarse-grained regions, while a higher hardness (~320 HV) is observed in the fine-grained zones. Additionally, in the melt pool of L-PBF IN718, as shown in Figure 16a-d, a variation in hardness distribution has been observed where authors attribute it to the local grain and dendrite morphology [225]. The top of the melt pool shows a higher average hardness of 388 HV, whereby the microstructure is dominated by fine, cellular dendrites and equiaxed grains Fig. 16b). The hardness decreases to about 335–340 HV at the bottom of each melt pool, whereby the microstructure is composed of unidirectional columnar dendrites (Fig. 16c). The edge of the melt pool averages a hardness of 341–350 HV, with the microstructure mainly characterized by the presence of multidirectional columnar dendrites, as seen in Fig. 16d.

The dislocation cell networks also contribute to the hardness enhancement in as-printed Ni-based superalloys by acting as obstacles for dislocations. This contribution is mainly recognized and appreciated when the build contains little if any γ' or γ'' precipitates in the as-fabricated state. For example, Deng et al. [226] attributed the hardness in L-PBF IN718 which was free of strengthening γ' and γ'' phases to the high density of dislocation cell networks. Also, the hardness observed in new grades of Ni-based superalloys fabricated with L-PBF was attributed to solid-solution hardening and substructural hardening as few γ' precipitates were found in in these builds owing to their sluggish precipitation in this alloy [227]. For a solid-solution forming Ni-based superalloy such as Hastelloy X, the hardness observation in the build after deposition is due to the domination of dislocation and subgrain structures in the microstructure [215,216].

The distribution of porosity in AM builds was believed to affect the hardness in some studies, while others found no direct relationship. Few papers have attributed the lower hardness in builds to the high porosity as pores easily collapse upon loading. Choi et al. [213] observed a decrease in hardness as porosity increased in an L-PBF IN718, and attributed it to the collapse of the relatively large and irregular-shaped pores under loading. Also, as shown in Fig. 16e, Marchese et al. [228] found that the hardness in an IN625 fabricated with L-PBF and L-DED slightly decreased in regions with a high level of porosities. A similar trend is also observed in [229], but the authors attributed the hardness decrease to coarsened microstructure. In E-PBF IN718, no direct correlation between the hardness and porosity was found [230].

4.3.2. Tensile properties

Several studies have investigated the general (macro-scale) tensile behavior of AM Ni-based superalloys at room temperature and have shown these properties to be comparable to their cast and wrought counterparts [16,32,46,173,192,198,231–233]. Similar to hardness, the reported tensile properties have been attributed to the strengthening of nanoscale precipitates, dislocation cell structures, grain morphology, dendrite morphology, and nanoscale oxides present. Also, defects (cracks and pores) and the build orientation which result in anisotropy greatly influence the tensile properties. The high-temperature tensile properties of AM have been studied in several investigations as these alloys, by nature, are used in high-temperature environments. Some of these studies were conducted at temperatures of 538 °C [234], 650 °C [235], 750 °C [137,236], 760 °C [237], and 850 °C [238]. Generally, all studies reported extraordinary strength at the above-mentioned high temperatures which was mainly attributed to the presence of nanoscale precipitates, the ultra-fine solidification microstructure, and the presence of thin and long needles of δ phase at the grain boundaries.

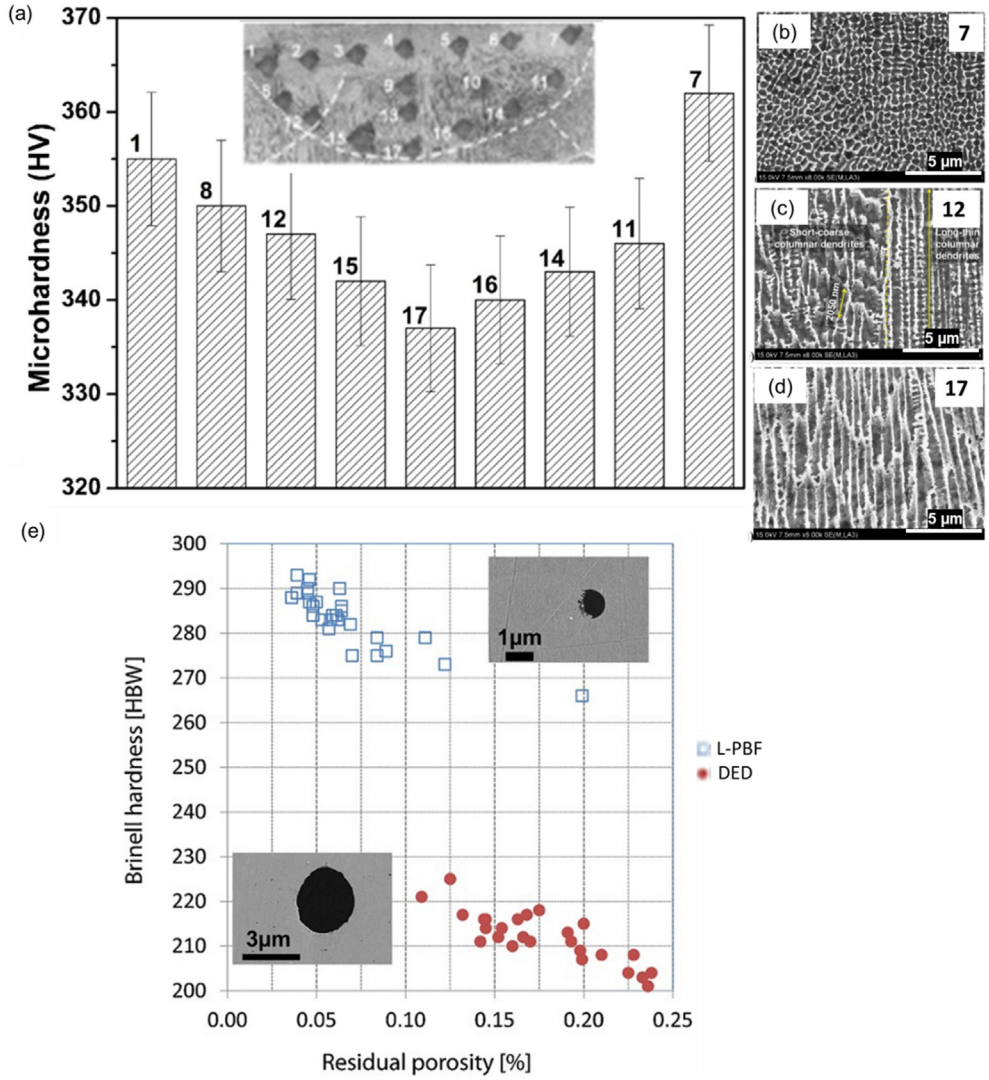

Fig. 16. (a) Typical hardness profile within the melt pool of L-PBF-processed IN718 parts. (b), (c), and (d) show the corresponding microstructure evolution of the hardness positions labeled as 7, 12, and 17, respectively. The inset image in (a) shows the cross-section of the melt pool profile. (e) Hardness vs porosity distribution in L-PBF and L-DED IN718. Inset image shows typical pore sizes. (a-d) are adapted from Ref. [225] and (e), from Ref. [228] with permission.

Precipitation hardening from nanoscale precipitates in the as-built components contributes significantly to their high tensile strength. Several studies report higher tensile strength values in as-built parts with a high percentage of in-situ precipitated nanoscale particles than in those with no or fewer precipitates. For instance, in IN718, most E-PBF fabricated components exhibit higher strength than L-DED or L-PBF components [239]. This is attributed to the higher processing temperature of the E-PBF process, which causes in-situ precipitation of γ' and γ'' phases. Also, builds subjected to full post-processing heat treatments exhibit higher strength and lower ductility than those in their as-fabricated state [30,214,240]. This is due to the significant increase in precipitation of nanoscale phases during aging heat treatments. Since most of the builds with in-situ precipitated nanoscale precipitates exhibited heterogeneities in their morphology and distribution, heterogeneities in the local tensile properties may exist along the build direction. Studies on the heterogeneity in the tensile behavior are limited due to the relatively small size of printed samples, which makes machining tensile specimens from selected regions along the build difficult or sometimes impossible. Table 2 shows a summary of the tensile properties reported along the build direction of typical AM Ni-based superalloys. In Ref. [32], the higher yield and tensile strength at the bottom and middle compared to the top is ascribed to the higher fraction of nanoscale precipitates at the bottom and middle. This trend is similar to that of the hardness observed in the previous section. The study in Ref. [46] attributes the observed variation in yield and tensile strength to the variation of the columnar grain structure in size along the build direction, as no nanoscale precipitates were present. The top region with coarser grains recorded a lower yield and tensile strength than the bottom, which had much finer grains. Generally, the reasons for the observed trend in hardness along the build height for most DED, L-PBF, and E-PBF printed Ni-based superalloys may also apply to the tensile properties.

Further, for alloys such as IN718 and IN625, the presence of Laves and δ phases may influence the tensile properties. For example, in the E-PBF process, Kirka et al. [192] report an increase in tensile and yield strength, along with the ductility of IN718 from the bottom of the build to the top (Table 3). An opposite trend in tensile strength along the build is reported in Refs. [32,46]. The lower tensile strength in the bottom region is ascribed to the coarsening of γ' and γ'' precipitates, together with the presence of a higher amount of detrimental δ phase at the bottom of the build due to over-aging and slower cooling rate induced by the elevated

Table 3
Summary of room temperature tensile properties along the build height of various as-built Ni-based superalloys.

Superalloy	AM Process	Position of Measurement	Tensile axis orientation to build direction	Yield Strength (MPa)	Ultimate tensile strength (MPa)	Elongation (%)	Ref.
IN718	DED	Top		464 ± 44	821	34	[32]
		Middle	Perpendicular	752 ± 12	1074	22	
		Bottom		745 ± 5	1050	31	
IN718	L-PBF	Top		603 ± 2	985 ± 2	38 ± 1	[46]
		Bottom	Parallel	650 ± 9	1023 ± 10	33 ± 1	
IN718	E-PBF	Top		920	1148	21	[192]
		Middle	Perpendicular	900	1075	12	
		Bottom		875	950	5	
IN625	PPAD	Top	Perpendicular	380	680	49	[134]
		Bottom		500	755	47	

build temperature (945 °C). Alongside the Laves phase, the morphology of dendrites can also influence the tensile properties. In the build of IN625 fabricated with an AM technique called pulsed plasma arc deposition (PPAD), the tensile strength throughout build was non-uniform [134]. The yield and tensile strength decrease from the bottom to the top owing to the variations in the size distribution of the precipitates and dendrites. At the bottom, fine columnar dendrites and fine Laves phase particles are discretely distributed in the interdendritic areas and around grain boundaries, which is beneficial to the mechanical properties. However, coarse columnar dendrites are observed in the top region, and the morphology of the Laves phase is coarse and interconnected, leading to a deterioration in tensile properties. It should be noted that no γ' and γ'' phases are precipitated in the build owing to the low deposition rate during printing which causes a short holding time in the precipitation temperature windows. This accounts for the overall low tensile strength of the build compared to those in other studies [32,46,192].

Other studies have attributed the tensile properties to the dislocation cell network present in the microstructure. An example can be seen in [231], where the authors attributed the superior tensile properties of L-PBF Hastelloy X compared to their wrought counterparts to the fine cellular dislocation structure. A similar result can also be seen in [216,241,242], where the cellular dislocation structure enhanced the strength by limiting the slip of dislocations and obstructing the formation of deformation bands. The presence of nanoscale oxides or inoculants is reported to further enhance the tensile properties by promoting grain refinement and hindering dislocation movements. For instance, the intentional addition of TiC nanoparticles in L-PBF Hastelloy X improved the yield and tensile strength [173]. Similarly, the tensile strength of L-PBF IN718 specimens was enhanced by adding TiC nanoparticles [243]. Studies on the strengthening effects of other nanoparticles or inoculants can be found in [217,244,245].

Another critical factor affecting AM Ni-based superalloys' tensile properties is the build orientation (vertical or horizontal). As shown in Table 4, many studies have reported a higher ductility, and lower yield/tensile strength for samples loaded parallel to the build direction. Such anisotropy has been attributed to the columnar grain orientation, crystallographic texture, and processing defects such as LOF defects. In an L-PBF IN718, Ströβner et al. [246] reported a higher yield strength, higher ultimate tensile strength, and lower ductility for samples loaded perpendicular to the build direction than those loaded parallel to it. The anisotropy in strength was ascribed to the usual ⟨001⟩ texture and the columnar grain morphology of AM IN718. Similarly, Ni et al. [247] found that a transversely built IN718 possessed better strength than its longitudinal built counterpart. The Schmid factor of the transverse samples was much smaller than that of the longitudinal samples, explaining the higher yield strength. Similar findings were reported in [169,248]. The anisotropy of ductility has been attributed to the higher tendency of columnar grain boundaries to delaminate (long axes of grains submitted to mode I opening tension) when loads are perpendicular to the columnar grain boundaries than when they are parallel. The directionality of defects such as LOF and cracks play an important role in the anisotropy in an AM builds' tensile properties. The trend in tensile anisotropy behavior is opposite to what was previously discussed. Loaded samples perpendicular to the plane of defects enables crack propagation along the tip of the defect. Several papers have reported a significant reduction in strength in the transverse direction of build owing to LOF pores or cracks with planes aligned parallel to the longitudinal or build direction [116,171,232,239,249,250]. Anisotropic tensile behavior is found to also exist at elevated tempera-

Table 4
Summary of room temperature anisotropic tensile properties of various as-built Ni-based superalloys.

Superalloy	AM Process	Tensile axis orientation to build direction	Yield Strength (MPa)	Ultimate tensile strength (MPa)	Elongation (%)	Ref.
IN738LC		Parallel	765 ± 10	–	–	[253]
	L-PBF	Perpendicular	853 ± 16	–	–	
IN718	L-PBF	Parallel	711 ± 14	1110 ± 11	24.5 ± 1.1	[247]
		Perpendicular	858 ± 12	1167 ± 10	21.5 ± 1.3	
Nimonic 263	L-PBF	Parallel	653 ± 11	860 ± 8	70 ± 1	[29]
		Perpendicular	818 ± 8	1085 ± 11	24 ± 4	
IN718	L-PBF	Parallel	1240	1400	–	[254]
		Perpendicular	1300	1510	–	
IN718	DED	Parallel	1215	–	–	[169]
		Perpendicular	1290	–	–	
IN718	L-PBF	Parallel	572 ± 44	904 ± 22	19 ± 4	[255]
		Perpendicular	643 ± 63	991 ± 62	13 ± 6	
IN718	E-PBF	Parallel	924	1113	31.51	[116]
		Perpendicular	771	1002	40.35	
IN718	E-PBF	Parallel	822 ± 25	1060 ± 26	22	[171]
		Perpendicular	744 ± 44	929 ± 20	5.5	

tures, which was related to the anisotropic texture evolution [122,251,252].

4.3.3. Young's modulus

The Young's or elastic modulus (E) depends mainly on the local texture/crystallographic orientation distribution in the build. Like anisotropy in yield strength, the elastic modulus will vary with build orientation as the texture/crystallographic orientation of AM Ni-based superalloys are different for directions parallel and perpendicular to the build direction.

Some authors have studied the anisotropy in the elastic modulus of AM Ni-based superalloys [256]. Their observation mainly indicated a lower elastic modulus for samples loaded parallel to the build direction. In L-PBF of IN738, Kunze et al. [257] reported a lower elastic modulus at elevated temperatures for samples loaded parallel to the build direction than perpendicular to it. Also, Tayon et al. [258] showed a change in the elastic modulus of E-PBF IN718 with respect to the deposition direction. Samples loaded parallel to the build direction recorded a lower elastic modulus than perpendicular to it. In the build direction, many grains were preferentially aligned with the low-modulus ⟨100⟩ direction in the deposition direction [258]. Similarly, Körner et al. [259] attributed the lower elastic modulus in the build direction to the columnar grain elongation in the crystallographic [100] direction.

Although the elastic property of a material mainly depends on the local texture/crystallographic orientation distribution, a study by some of the current authors on E-PBF INC738 reports a gradient in elastic moduli along the AM build direction while no changes in texture as well as grain size or morphology was observed through the build [42]. This was attributed to variations in γ' chemistry, morphology, and γ/γ' interface densities. In the same report, the authors used nano-indentation test and SEM micropillar compression tests to measure the elastic moduli in the top and bottom region of AM INC738 specimens. Fig. 17 shows the engineering stress–strain curves of the three pillars from {100} grains from the top and bottom layers (x-y) used to measure the elastic moduli. As seen in the plot, the slope of the strain burst regions of the pillars from the top of the build is higher than that of the bottom. This implies a higher elastic modulus at the top of the build compared to the bottom. This is in line with the nano-indentation results showing a 145 % increase in the elastic modulus from the bottom.

4.3.4. Creep

The creep behavior of AM Ni-based superalloys has been investigated in several studies [20,21,121,171,238,257,260–263]. Most of these studies revealed superior creep responses for various reasons, including process-induced subgrain formation, build orientation effects, the small and thin morphology of δ-precipitates (especially in IN718 and IN625), and the presence of a higher number density of finer nanoscale precipitates. Pore formation and surface defects are the main factors that account for the poor creep response in other reports [171,260].

While several studies have been devoted to the response of AM Ni-based superalloys to creep, the studies on heterogeneity in creep behavior in various regions of the build is limited. Similar to tensile testing, this is also attributed to the relatively small size of most printed samples. As the creep rate is reported in most literature to increase with γ' precipitate size, it is expected that the response to creep along the build in AM Ni-based superalloy will be heterogeneous [264–266]. A critical study on the heterogeneity in creep behavior is reported by Burger et al. [121], where they investigated the response of the middle and top section of a CMSX-4 Ni-based superalloy build to creep after E-PBF. The top of the build showed higher rupture strains and slightly longer rupture lives than the middle, which was attributed to a finer γ/γ' microstructure in the top part than close to the middle and bottom.

Anisotropy of creep performance of AM Ni-based superalloys has been widely studied. Most of these studies showed a better creep response for samples loaded parallel to the build directions [171,257,260,267,268], whiles others show no significant change in creep behavior with build orientation [262]. Kunze et al. [257] reported a superior creep behavior of L-PBF IN738 specimens loaded parallel to the build direction than specimens perpendicular to the build direction. The improved creep behavior in the build direction was due to the application of stress primarily parallel to the elongated columnar grains. This phenomenon is similar to the creep resistance strengthening mechanisms in directionally solidified and single crystal superalloys [269]. Similarly, for E-PBF IN738, under creep conditions, Kirka et al. [270] showed that transversely

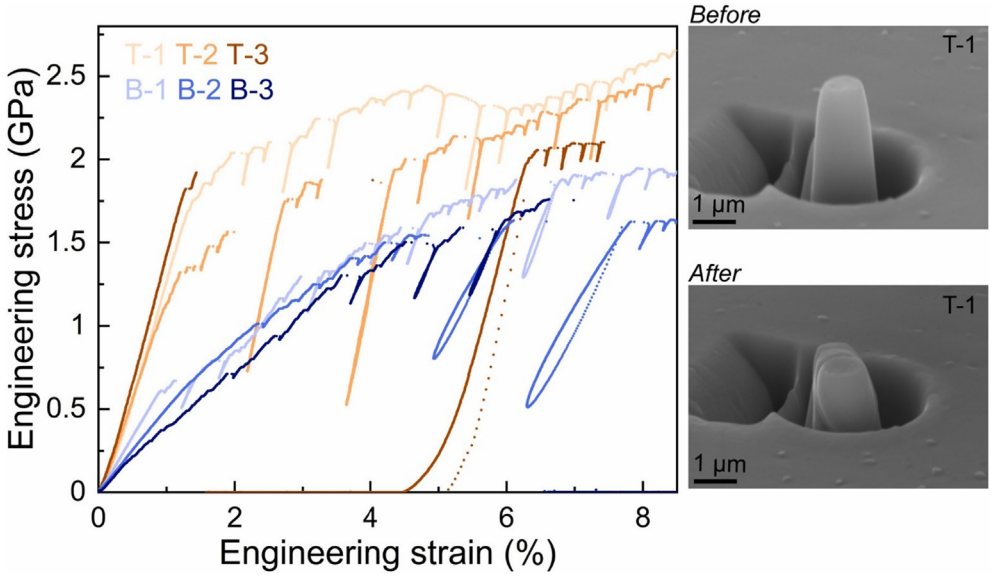

Fig. 17. Engineering stress–strain curves of the three pillars from {100} grains in IN738 from the top and bottom layers which were used to measure the elastic moduli by some of the current authors. Top/Bottom-pillar 1/2/3 were denoted as T/B-1/2/3. SEM micrograph of T-1 before and after compression loading is shown on the right. Adapted from Ref. [42] with permission.

oriented samples exhibited higher deformation rates and decreased rupture strength relative to the longitudinal counterparts. This was attributed to the fact that an externally imposed stress engages more grain boundaries in the transverse orientation, which promotes diffusion along grain boundaries rather than in the longitudinal orientation. In addition, most of the grain boundaries in the transverse orientation were perpendicular to the applied load, which promoted intergranular fracture and decreased the rupture resistance. Most columnar grained specimens exhibit a higher creep resistance than equiaxed grained specimens, especially when the specimen is loaded parallel to the columnar grain growth direction. This explains why most vertically oriented AM samples have superior creep properties compared to their wrought counterparts [238,271]. In IN718, some authors have pointed to the presence of coarser interdendritic δ-phase precipitates to justify the inferior creep life of specimens loaded perpendicular to the build direction [171,260]. These precipitates are mostly perpendicular to the stress axis and, hence, act as sites for rapid creep cavity nucleation and propagation during loading.

4.3.5. Fatigue

The fatigue performance of as-fabricated Ni-based superalloys is generally inferior to those exhibited by wrought samples, causing growing concerns about their applicability in some critical components [272–274]. This is mainly attributed to process-induced pores, lack of bonding between layers, non-equilibrium phases, and rough build surfaces. These features have the potential to increase the local stress level to the point where plastic strains occur. In most L-DED and L-PBF IN718 builds, the inferior fatigue endurance was attributed to AM defects which affected the fatigue crack initiation via stress concentration [273,275]. Residual stresses also affect fatigue performance as they might promote crack initiation and propagation [276]. Post-processing techniques such as heat treatment, hot isostatic pressing, and surface machining can improve the fatigue strength. For instance, a high-cycle fatigue testing on machined L-PBF IN718 behaved similarly to its wrought counterpart plate, but testing with as-fabricated surfaces led to a reduced fatigue life [275]. Also, the use of post-processing heat treatment significantly improved the high-temperature fatigue life of L-PBF IN718 through Laves phase dissolution and formation of fine δ needles at the grain boundaries [277].

Like tensile and creep properties, the effect of build orientation on the fatigue performance of AM Ni-based superalloys has been investigated [249,278–280]. For an L-PBF IN718 build, Konečná et al. [276] and Carter et al. [274] reported a higher fatigue endurance in samples loaded transversely to the build direction (horizontal) than those loaded parallel to it (vertical). Also, the best fatigue strength in L-PBF Hastelloy X was reported for samples loaded perpendicular to the build direction [268]. In terms of fatigue life, L-DED IN718 samples oriented 45° (diagonal) to the build direction had a longer life than samples oriented perpendicular (horizontal) [279]. Authors attributed this to grain shape effects relative to the loading direction. The 45° oriented sample had a longer mean free path for dislocation slip than the horizontal sample. The grain morphology impact on fatigue performance of L-PBF Ni-based superalloys is also revealed in [281], where the authors observed anisotropic low-cycle fatigue properties in columnar grained samples while no noticeable sensitivity to the orientation was exhibited in equiaxed grained samples. The columnar grains oriented parallel to the build direction exhibited on average the highest life when compared to the transverse columnar material. Similar observations can be found in the work of Kirka et al. [249] who studied the impact of texture (columnar/equiaxed grain structure) and material orientation on the low cycle fatigue in E-PBF IN718.

4.3.6. Residual stress

Residual stress in AM parts is undesirable and may lead to a part's distortion and eventual failure. Residual stress is introduced due to the large thermal gradients from localized rapid heating and cooling during the layer-by-layer processing [105,137]. The origins of residual stress in AM is schematically shown in Fig. 18a [282]. During deposition, the already deposited layer restricts the expansion of the subsequent layer, leading to compressive plastic deformation of the new layer at high temperatures. Upon cooling, the newly deposited layer contracts, but it is restricted by the previous layer resulting in tensile residual stress in the new layer [283]. The residual stresses in AM components are studied by numerical simulations and experimental techniques such as X-ray and neutron diffraction as well as Vickers hardness indentation.

In AM Ni-based superalloys, several studies have shown the residual stress distribution to be inhomogeneous and influenced by the AM process parameters such as scan speed/strategy, layer thickness, overlap rate, hatch spacing, and heat input [61,284,285]. These parameters alter the thermal gradient during deposition. Ahmad et al. [206] reported higher compressive residual stress in the central region of L-PBF IN718 and high tensile residual stress at the free edges. This was attributed to the difference in heat dissipation at the center and edges of the build. Lu et al. [107] investigated the effect of the island scanning strategy on the residual stress of IN718 fabricated with L-PBF using different island sizes (3x3, 5x5, and 7x7 mm^2). The residual stress increased with the following sequence: 5x5 < 7x7 < 3x3 mm^2. The smallest island size with a shorter scan vector experienced a larger temperature gradient due to the previous scan pass' higher residual heat. Also, Liu et al. [286] used X-ray diffraction techniques to study the influence of laser energy input and scanning vector on the residual stress distribution on IN718 in different directions. They reported a higher tensile residual stress along the laser scanning direction than in the build direction. Also, applying a shorter scanning vector length and a lower energy input decreased the residual stress at the free edges.

In another study (Fig. 18b), the impact of four different scan strategies (x, y, alternating, and rotational) on residual stress development in L-PBF IN718 was investigated [287]. The × strategy exhibited the highest stress, followed by the y and alternating scan strategies, with the rotating strategy showing the lowest. The × scan strategy sample observed a gradient in stress distribution from the top towards the middle of the sample (along the hatching direction). A gradient in stress distribution was also found for the y strategy but was observed along the width of the build. This can be attributed to the different scanning strategies that result in different local thermal cycles and constraint conditions during the solidification process [108]. Further, in a L-DED fabricated IN718, the adjacent track overlap area, which is determined by the hatch spacing, was reported to affect the residual stress distribution significantly. An increase in the overlap area increased the residual stress. Also, different residual stress distributions were observed in the overlap and inner-pass areas due to different reheating temperatures. The residual stress in the overlap area was much higher than in the inner-pass area. The peak values of the residual stress were located at the overlap area and closer to the previous pass. The hatch spacing influence on residual stress distribution is further seen in [288], where authors reported a change and gradient in the residual stress profile with a change in hatch length in L-PBF IN718. Along the scanning direction, samples with longer hatch length exhibited large gradients in residual stress than those with shorter ones. Also, a change in stress state from tensile in the middle to compression towards the edge was observed with the short hatch length samples being highly compressive. Changes to the thermal gradient due to the hatch length variation affected the residual stress distribution [288].

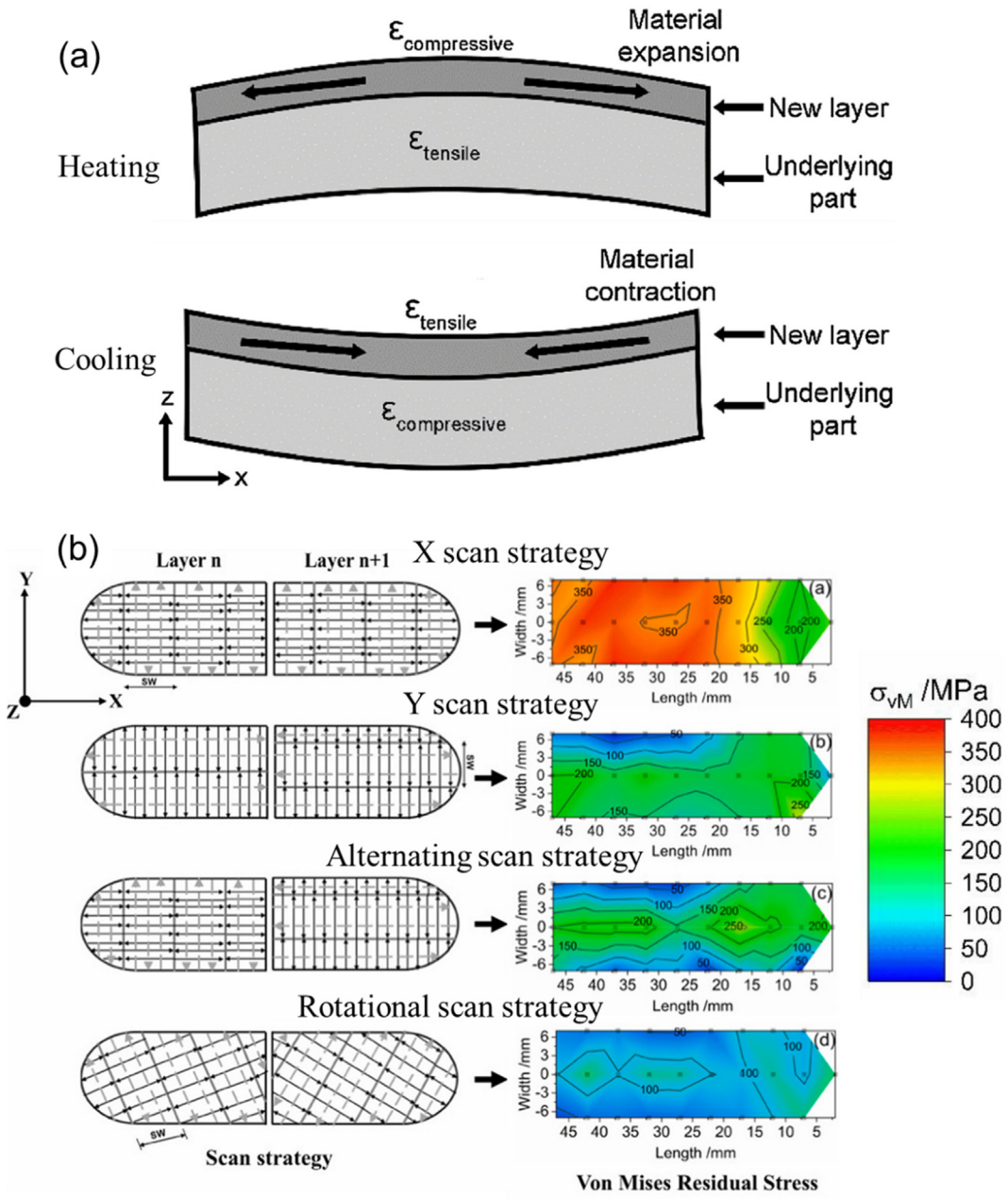

Fig. 18. (a) Stress and plastic strain formation mechanism during heating and cooling of a new layer in AM. (b) Von Mises equivalent stress in the top surface for L-PBF IN718 fabricated using different scan strategies; X, Y, alternating, and rotational scan strategy. (a) is adapted from Ref. [282], and (b) is adapted from Ref. [287] with permission.

The evolution of cyclic thermal stresses during AM can also lead to the accumulation of localized plastic strain gradients in a build [289–292]. The accumulation of plastic strain during AM is reported to significantly affect the response of a material, leading to changes in the local microstructure and properties. A typical example is seen in the work of Foster et al. [293], where the heterogeneity in the hardness of L-PBF fabricated IN718 alloy was ascribed to the accumulated plastic strain that occurred during the transient thermal stress evolution. Also, the presence of cellular networks of dislocations in the dendritic and interdendritic structures of most superalloys are attributed to cyclic thermal stresses [29,125]. Wang et al. [294] have attributed the origin of residual high-density dislocations in AM metals (Ni-based superalloys, stainless steel, high entropy alloys) to several cycles of compression-tension in the build. In other studies, the residual stress development in builds is reported to be the driving force for static recrystallization during a heat treatment which can lead to heterogeneities in the grain structure [240,295,296]. For example, during heat treatment of AM IN718, overlapping regions with higher residual stress had finer recrystallized grains than adjacent areas [240,295].

Cyclic thermal stress-induced plastic strains could also significantly influence the solid-state phase transformation kinetics as confirmed in some AM studies [279,297,298], and most traditional thermo-mechanical processes such as creep, fatigue, and hot deformation. Lopez-Galilea et al. [279] reported that residual stresses generated during L-PBF of CMSX-4 led to a high dislocation density, which affected the nucleation of TCP phases. Also, Lass et al. [297] demonstrated that the application of a stress-relief heat treatment protocol of 1 h at 870 °C promoted the inhomogeneous formation

of δ-phase in L-PBF IN625. δ-phase precipitation was enhanced during the relief of the accumulated residual stress in the build. For traditional thermomechanical processes, a study by Semiatin et al. [299] showed that the concurrent cooling and straining of a low solvus high refractory (LSHR) Ni-based superalloy gives rise to coarse, secondary γ′ precipitates compared to those of similar cooling conditions under no straining or deformation. Also, Radavich and Fort [300] and Mataveli Suave et al. [78] reported faster δ precipitation in IN625 and IN718 after prestraining, respectively. The morphology and spatial occurrence of γ′ precipitates (inter/intragranular) during hot deformation are mainly determined by the strain rate [301,302]. Concerning the dissolution kinetics of γ′ precipitates, plastic strain accumulation greatly enhanced their dissolution rates. This is evident in the work of Giraud et al. [60] in their study of the γ′ dissolution kinetics of CMSX-4 as a function of temperature and applied stress. The morphology of γ′ precipitates under thermomechanical loading may evolve from cubic to plate-like shape in a process known as rafting or directional coarsening. This rafting or coarsening behavior is influenced by the plastic deformation around the γ/γ′ interfaces [303,304]. Engler-Pinto et al. [305] revealed the elongation of γ′ microstructure into rafted platelets while studying the creep and thermomechanical fatigue behavior of CM247LC.

4.3.7. Case study

This section is closed with our own schematic (Fig. 19), summarizing the main microstructure heterogeneities observed along the build height in AM Ni-based superalloy and the relating mechanical properties. Fig. 19a describes the variation in thermal history across an E-PBF build where each region experiences different amount of heat accumulation from the elevated build temperature. The bottom region shows the highest heat accumulation, followed by the middle, and the top. The resulting microstructure in terms of the morphology of nanoscale precipitates along the build is shown in Fig. 19b and c. Different behavior of precipitate is seen in both Figures, and it is mainly dependent on the type of the Ni-based superalloy. Fig. 19b shows an increase in nanoscale precipitates size from the build top to bottom. This is mostly seen in high γ′ Ni-based superalloy in which there is no significant variation in the volume fraction of γ′ [31,42,44,47]. The tensile strength, creep, and hardness decreases from build top to bottom. In Fig. 19c, a decrease in volume fraction from the build bottom to the top is shown. The tensile strength, creep, and hardness increases from build top to bottom. This is commonly seen for most IN718 build [24,43,198]. Also, most L-DED and L-PBF Ni-based superalloy builds exhibit this kind of behavior [25,32,46,196]. The resulting microstructure in terms of the grains and dendrites morphology is shown in Fig. 19d. The width of columnar grain and dendrites increases along the build for some cases [43,44,117,133,134], whereas for others, grain morphology changes from columnar to equiaxed [118,147,148].

5. Mitigating heterogeneity

5.1. Susceptibility of Ni-based superalloys to heterogeneity

Besides processing, the microstructure and mechanical properties of Ni-based superalloys are determined by the elemental composition. Precipitate strengthened alloys with high Al, Ti, or Nb contents usually exhibit more complex microstructures compared to those that gain their strength through solid solution [62,64,65]. Due to the complexity of the microstructure of precipitate strengthened Ni-based superalloys, they are highly susceptible to heterogeneity in AM. Among the precipitation strengthened alloys, those with high Nb content exhibit a greater degree of microstructure heterogeneity due to the high amount of solidification phases and a high degree of elemental segregation [180,183].

For instance, the presence of Laves phase, δ-phase, and Nb segregation at certain interfaces are mostly seen in alloys such as IN718 and IN625 due to their high Nb content. As a result, these alloys are susceptible to heterogeneities in terms of Laves phase distribution, Nb segregation, and Nb content in the matrix. A

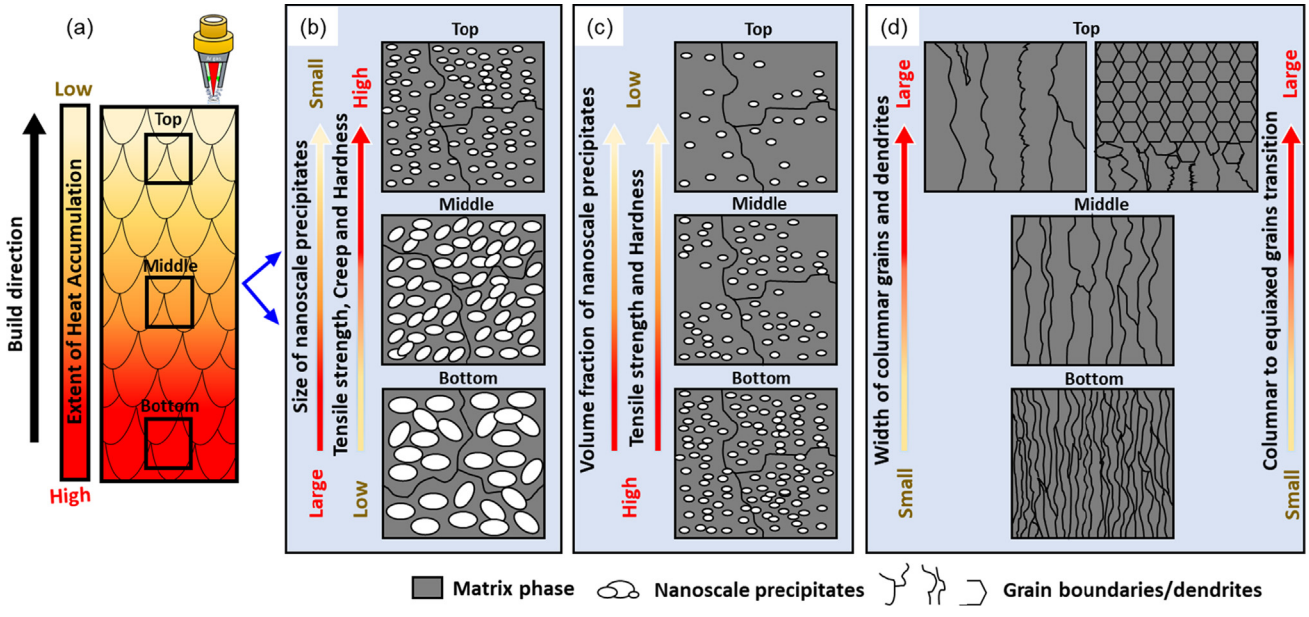

Fig. 19. A schematic summarizing the main microstructure heterogeneities observed in E-PBF Ni-based superalloy and the corresponding gradient in mechanical properties. (a) Typical variation in thermal histories across an E-PBF build which strongly influence the microstructures shown in (b), (c) and (d). (b) and (c) show different behavior of the nanoscale precipitates, which depends mainly on the type of the Ni-based superalloy. (b) Variations in the size of nanoscale precipitates along the build height with no significant variation in the volume fraction. (b) is mainly seen in high γ′ Ni-based superalloys. (c) Variation in volume fraction of nanoscale precipitates along the build height. (c) is commonly seen for most E-PBF IN718 builds, and other Ni-based superalloys fabricated with DED and L-PBF. (d) Variation in width of columnar grains and dendrites. It also shows instances where the grain morphology changes from columnar to equiaxed.

higher volume fraction of Laves phase is usually observed at the top of IN718 and IN625 builds compared to the bottom. In addition, thick and continuous Laves networks are also seen at the top [19,134,183,184]. These are attributed to a higher amount of Nb segregation at the interdendritic regions at the top, which is equivalent to the decrease in Nb content in the dendrite core along the build direction [115]. In terms of the γ' and γ'' phases in the matrix, typical volume fractions of $\sim$ 4 and 16 %, respectively, are usually observed after a complete heat treatment. In the as-fabricated state, the volume fraction is usually lower, and the most observed heterogeneity is a decrease in volume fraction along the build height [24,25,32,196,197]. These are generally observed for DED and L-PBF processes. However, there are instances where a lower deposition rate or faster cooling rate is utilized, and no γ'' forms after deposition [199,200]. γ'' has slow precipitation kinetic and can be suppressed by using a fast cooling rate or a low deposition rate. In E-PBF IN718, due to the low solvus temperature of γ'', the distribution normally depends on the preheat temperature. A preheat temperature above the solvus temperature causes dissolution during deposition, from which upon cooling, fine γ'' precipitates form. Accordingly, in some cases, the volume fraction of γ'' decreases along the build [112,116,162]. A low preheat temperature causes heterogeneity in γ'' size distribution along the build and the precipitation of secondary phases such as Laves and δ [192].

For solid-solution strengthened, high γ' and medium γ' Ni-based superalloys with no or limited amounts of secondary phases and low degree of elemental segregation, the heterogeneity in the solidification microstructure is usually limited to the variations of the dendritic and grain structure along the build [135,147]. No γ' precipitation is observed in solid solution strengthened alloy such as Haynes X during cyclic layer deposition [215,216,231] and hence no heterogeneity. For high γ' Ni-based superalloys such as IN738, CMSX-4, CM247LC, and Rene N5, γ' is distributed throughout the build for most AM processes in the as-fabricated state. This is due to its fast precipitation kinetic, and the higher amounts of Al and Ti. The heterogeneity in γ' morphology is usually dependent on the AM process. Most DED and some L-PBF fabricated alloys show a decrease in γ' volume fraction along the build with a slight variation in size, while for E-PBF, there is a decrease in γ' size along the build with a negligible change in volume fraction [31,42]. It should be noted that the high cooling rate of L-PBF results in γ'-free parts in some alloys [120]. For medium γ' Ni-based superalloy such as Haynes 282 and Rene 41, owing to the sluggish γ' formation kinetics, no sign of γ' formation is usually seen during L-PBF or DED [306,307]. E-PBF however will cause precipitate γ' with a gradient in size or volume fraction along the build [48].

The dependence of microstructure heterogeneities on the type of Ni-based superalloy implies that designing new alloys or modifying the composition of current alloys may help to control heterogeneities. To design an alloy with minimum heterogeneity in the as-fabricated state, it is necessary to consider if any heterogeneities can be controlled during printing by changing the printing method and process parameters. Process parameter optimization to control heterogeneities has been reported in several studies [58,90–93,163,308–310]. Altering the scan speed, beam power, build temperature, and interlayer dwell time, which tends to control the thermal condition, can reduce heterogeneities in the solidification phase, micro-segregation of elements, dendrite and grain morphology, and sometimes γ'' precipitates [58,90–93,163,308]. This is elaborated in the next section. However, if process parameter control is insufficient, the composition must be altered, necessitating the design of new alloys.

The optimization of traditional Ni-based superalloys for AM techniques has been widely studied [311]. Most of these studies focused on improving the crack resistance of non-weldable alloys during AM by modifying the alloy chemistry [227,312]. The heterogeneity in γ' size distribution for high γ' Ni-based superalloys during E-PBF can be difficult to control via process parameter variation. Unlike γ'' in IN718, which requires a preheat temperature of 1000 °C to cause the dissolution during printing and uniform re-precipitation during cooling, high γ' would require a much higher process temperature. This is due to the high solvus temperature of γ'. Increasing the preheat temperature can, however, lead to extensive grain growth, high γ' coarsening, and incipient melting. It is therefore necessary to suppress the γ' solvus via alloy modification whilst retaining a reasonable volume fraction which is needed for the high-temperature properties [227].

5.2. Strategies to minimize microstructure heterogeneity

This section discusses various strategies, such as heat treatment, hot isostatic pressing (HIP), and processing parameter optimization that can be used to minimize microstructure heterogeneity in AM Ni-based superalloys. Heat treatment and HIP are post-deposition treatments, whereas processing parameter optimization is done during deposition.

AM Ni-based superalloys are generally subjected to post-heat treatment processes to improve builds' microstructure and mechanical properties [212,233,313,314]. The typical post-heat treatments include solution annealing, followed by double aging, the heat treatment condition (temperature and time) of which mostly depends on the alloy. For example, AM IN718 undergoes solution annealing at 1000–1080 °C for 1 h followed by double aging at 720 °C for 8 h + 620 °C for 8 h [240]. The standard heat treatment for IN738 involves solution annealing at 1120 °C for 2 h, followed by cooling to 650 °C, and aging at 845 °C for 4–8 h [315]. For additional details about heat treatments of AM Ni-based superalloys, readers are pointed to the AMS2774 standard for heat treatment of wrought Ni-based superalloy alloy components [171], as the heat treatment operation for conventional cast and wrought Ni-based superalloys are usually employed for AM, currently. The purpose of solution annealing is to dissolve solidification phases such as Laves, δ, and other micro-segregate phases and the homogenization of Al, Ti, and Nb distribution in the matrix. This helps eliminate or reduce heterogeneity, e.g., in the distribution of Laves and micro-segregation in the build. Particles such as carbide, nitride and borides are not significantly affected.

Several studies have effectively eliminated the heterogeneity in solidification phases and chemical composition of AM Ni-based superalloy via post AM solution annealing [165,316,317]. A typical example is seen in the work of Xu et al. [317] who reported a complete dissolution of Laves phase and uniform distribution of Nb, thus preventing the formation of Nb-rich regions after employing an AMS 5383 standard heat treatment of cast IN718 on AM. Similar observations can also be seen in Fig. 20a-d, where Zhang et al. [160] achieved compositional homogenization across the microstructure of IN625 by subjecting the build to a heat treatment at 1150 °C for 1 h. Nb and Mo segregation were effectively homogenized. It should be noted that the extent of homogenization, especially for IN718, depends on the particle size (Laves, δ, and other micro-segregates), dendrite arm spacing, heat treatment temperature, and time. γ', γ'', and δ do not precipitate during homogenization as the temperature is higher than their precipitation windows [112]. After solution annealing, the subsequent aging treatment ensures the adequate precipitation and uniform distribution of fine nanoscale precipitates throughout the build. This eliminates or reduces heterogeneity in the distribution of nanoscale precipitates. Kirka et al. [316] employed solution treatment, followed by aging that effectively led to the dissolution of Laves, δ phase, and homogeneous precipitation of nanoscale precipitates

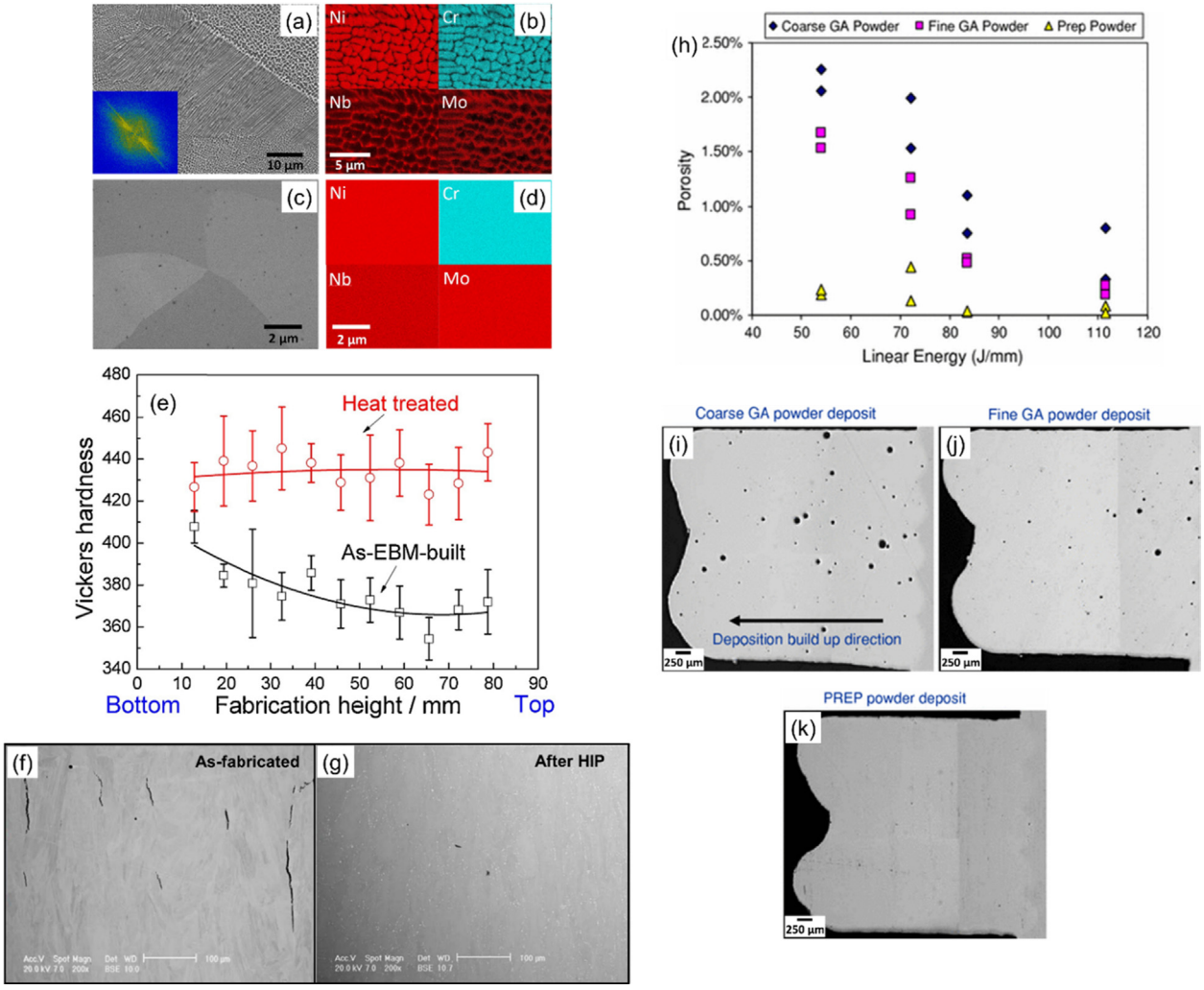

Fig. 20. (a), (b) SEM image and elemental X-ray maps of as-built IN625 sample. (c), (d): SEM image and elemental X-ray maps after homogenization treatment of as-built IN625 at 1150 °C for 1 h. (e) Hardness variations along the build height of an as-built and heat-treated E-PBF IN718. (f), (g) L-PBF CM247LC Ni-based superalloy before and after post-fabrication HIP treatment. (h) Effect of the laser energy input and powder size on the resultant porosity of L-DED IN718. (i-k) Sensitivity of porosity level versus powder type (GA vs PREP) and size of L-DED IN718. (a-d) are adapted from Ref. [160], (e) is adapted from Ref. [198], (f), (g) is adapted from Ref. [328], and (h-k) are adapted from Ref. [9] with permission.

throughout the height of the build of IN718. Similar results have been reported by other authors [214,318,319].

The improvement in the build's overall microstructure during the post-process heat treatment techniques is reflected in the resulting mechanical properties. Several papers have reported an improvement in various mechanical properties such as tensile [9,318], hardness [198], creep [262], and fatigue [272,277] after post-heat treatment of builds. As shown in Fig. 20e, Sun et al. [198] reported a higher hardness, which was uniformly distributed across the build of E-PBF IN718 after the heat treatment. This was attributed to the homogeneous microstructure from the dissolution of Laves and δ-phase during the homogenization treatment, and uniform precipitation of a more significant volume fraction of fine γ′ and γ″ precipitates during the subsequent aging treatment. Also, in an L-PBF IN718, Pröbstle et al. [262] reported an increase in creep performance after subjecting the build to a heat treatment and attributed it to the uniform distribution and higher volume fraction of strengthening γ′ and γ″ phases, and the absence of the δ phase. In terms of tensile properties, Zhang et al. [240] reported that heat treated (homogenization + aging) L-PBF manufactured IN718 yielded superior tensile strength to its as-fabricated counterpart, while the ductility exhibited the reverse trend. This was also explained by the higher volume fraction of strengthening γ′ and γ″ phases and dissolution of Laves and δ phases. Heat treatments are also reported to reduce the residual stress in the build. A typical example can be seen in the work of An et al. [320], where most of the residual stress in an L-PBF IN625 was relieved after a heat treatment. In another study, the maximum absolute compressive residual stress of L-PBF IN718 dropped from 378 to 321 MPa after homogenization of the microstructure [321].

HIP is one of the material processing methods that combines high temperature and pressure simultaneously to eliminate defects such as pores, voids, and internal cracks in solids [322]. It is widely used in the casting and powder metallurgy industry to improve the quality of metal parts. In AM, it has been a crucial process in the production line for aerospace applications [323]. The HIP temperature for Ni-based superalloy ranges from 1150 to 1280 °C, and the pressure, usually within 100–200 MPa [324]. Several authors have reported the effective reduction of pores, voids, and internal cracks in AM builds after HIPing [86,325–327]. Marchese et al. [327] observed the efficacy of using a standard HIP treatment to close the internal cracks and reduce residual porosity in an L-PBF Hastelloy X. Das et al. [326] reported the reduction in average porosity of

L-PBF IN625 after HIPing. A similar observation is reported in [215], where HIP improved the relative density of L-PBF Hastelloy X from 99.2 % to 99.9 %. Another study reports the successful use of HIP to close internal cracks in L-PBF CM24LC using X-ray Computerized Tomography scans [135]. Similar observations can also be seen in Fig. 20f and g, where authors reported eliminating internal cracks after a HIP treatment of CM24LC [328].

In addition to eliminating defects and improving build density, such a high-temperature treatment (>1100 °C) for a long duration (∼4h) can effectively cause the dissolution of second phases (Laves, δ, γ′/γ″, and other microsegregates) back into the matrix phase [8,316,329]. This leads to a highly homogenized chemical composition of the matrix. Additional standard aging steps will then cause the precipitation and uniform distribution of γ′/γ″ phases. As a result of the homogenized composition state of the γ-matrix after HIP treatment of E-PBF IN718 build, Goel [330] observed a uniform distribution of γ′ and γ″ after additional aging steps. Another example is seen in the work of Lopez-Galilea et al. [331], where the alloy was completely homogenized with no segregation upon quenching after HIP treatment of L-PBF CMSX-4. Subsequent aging steps of the HIPed samples resulted in a fine and uniform γ/γ′ microstructure. Similar results can also be seen in [332,333], where authors applied HIP with an integrated heat treatment on an E-PBF CMSX-4. Both observed a homogenized chemical composition in the matrix with no segregation, and a fine and uniform γ/γ′ microstructure.

The impact of HIP on the mechanical properties of Ni-based superalloy builds is widely accepted to be beneficial. Ormastroni et al. [333] observed superior high cycle fatigue properties in E-PBF CMSX-4 after HIP [333], which was attributed mainly to the absence of crack initiation defects such as large pores, stray grains, and non-metallic inclusions. Likewise, the fatigue lifetime of the sample observed in [332] was significantly higher than that of as-built material, owing to an almost defect-free part after HIP. Allowing the alloy to cool slowly after HIP is reported to cause a uniform distribution of nanoscale precipitates. For example, in an E-PBF IN718, during cooling after a HIP treatment, these authors observed a higher hardness than when quenched after HIP or in the as-fabricated state [112]. The increase in hardness is a result of the precipitation and uniform distribution of strengthening γ′ and γ″ phases. In another study, a HIP treatment of an IN738 build led to massive precipitation and uniform distribution of nanoscale precipitates which accounted for a 23 % increase in hardness [334]. In this study, the HIP treatment of the IN738 build lead to the closure of several pores and caused chemical homogenization through melting of segregates at the melt pool boundaries. This facilitated the precipitation of a higher amount of γ′ and its uniform distribution during cooling after HIP treatment. Similar phenomena can also be seen in the work of Sentyurina et al. [335] for a HIP treated Ni-based superalloy with comparable Ti and Al contents.

It should be noted that heat treatment at a high temperature (>1100 °C), especially for homogenization and HIP, may result in significant grain growth and significant changes to the original AM microstructure, such as elimination of cellular dislocation cell structures and deposition layer boundaries [336]. These may deteriorate the mechanical properties achieved via AM. On the other hand, a high temperature may remove the preferential ⟨100⟩ texture along the build direction, leading to a reduction in the anisotropy of microstructure and mechanical properties [337].

Process parameters such as beam power, interpass temperature, idle time, preheat temperatures, scan speed, and scan strategies strongly influence solidification conditions such as thermal gradient and cooling rate during fabrication [58,90–93]. As the microstructure of AM Ni-based superalloy is generally determined by the thermal gradient and cooling rate, careful processing parameter optimization is the key to ensuring effective microstructure control to reduce heterogeneity. For example, experimentally, it is shown that decreasing the energy density by manipulating various parameters leads to a refined equiaxial grain structure throughout the build of Ni-based superalloy [168,223]. Also, by modifying the melting strategy of E-PBF for a non-weldable Ni-based superalloy, Kontis et al. [145] altered the geometry of the melt pool, which changed the coarse-grained columnar heterogenous microstructure into a homogeneous microstructure with equiaxed grains (grain width ∼ 20 μm). In the same study, the authors produced another homogeneous microstructure with fine columnar grains (grain width approximately 50 μm) using a relatively low power and slow scan speed. The low power ensures a reasonably small melt pool that impedes grain growth and limits grain selection [145]. This shows that the melting strategy is critical in determining the microstructure of builds. The raster scan strategy produces builds with coarse columnar grains throughout, whereas a spot melt-scan strategy achieves fine, columnar grains [310]. Similarly, by taking control of the melting strategy, Chauvet et al. [309] grew single crystals of non-weldable Ni-based superalloys by E-PBF without using a crystal selector or a seed, as the melting parameters were suitable to cause the intensification of the competitive grain growth.

Optimizing process parameters such as increasing the heat input to a reasonable level during fabrication has been reported to reduce the porosity level in AM Ni-based superalloys [163,308]. Using a high energy input causes a larger melt pool with lower viscosity and better wettability. This reduces the probability of lack of fusion defect formation. It also reduces the risk of spherical gas-contained pores formation through the increase in the time of the molten metal for gas to escape [8]. An example is seen in Fig. 20h, where the porosity in a L-DED IN718 decreased with higher laser energy input [9]. However, an extremely high energy input may lead to several keyhole porosities [338,339]. The use of plasma rotating electrode processed (PREP) powder rather than gas atomized (GA) powder is also reported to reduce the porosity distribution in AM Ni-based superalloy builds [9,165,170]. This is due to the fact that the degree of entrapped gas in GA powders are significantly higher than in PREP powders; hence, during solidification, most of these pores in the GA powders get locked in the melt pool and form spherical pores [165]. An example of the sensitivity of the powder type (GA vs PREP) and size to porosity formation in AM Ni-based superalloy build is shown in Fig. 20 i, j and k for L-DED IN718 [9]. The powder size may also influence the porosity level in builds, as reported by Qi et al. [9]. As shown in Fig. 20h-k, builds with finer GA powder size have less porosity than those fabricated with coarser powder.

Adding inoculants or nanoparticles to the feedstock powder before printing is another method that can help to reduce microstructure heterogeneities in grain morphology. Nanoparticle additions to superalloys are primarily used in traditional processes such as casting and welding to improve the mechanical properties via grain refinement and via promoting the precipitation of fine carbides [340]. The added particles act as nucleation sites during solidification for the heterogeneous crystallization of the γ phase. In AM of Ni-based superalloys, several authors have reported a remarkable grain refinement that improved the mechanical properties upon introducing nanoparticles such as TiC [341], graphene nanoparticles [342], $CoAl_2O_4$ [217,343], and WC [224] to the powders. One example can be seen in [217], where Ho et al. studied the effects of $CoAl_2O_4$ inoculants on microstructure and mechanical properties of IN718 processed by L-PBF. The addition of nanoparticles enabled a higher proportion of fine, equiaxed grains and a reduction in the degree of crystallographic texture.

With regards to controlling the chemical composition homogenization and distribution of strengthening γ′ and γ″ particles in the build, the preheat temperature plays an important role. For

instance, in E-PBF IN718, using a high preheat temperature $\geq$ 1000 °C may cause chemical composition homogeneity in the build through segregate dissolution [112,116,162]. As higher preheat temperatures are above γ'' solvus, γ'' will not nucleate until after the final layer deposition, where cooling of the build to RT begins. Slow cooling of homogenized builds to RT will result in a uniform distribution of γ''. A study by Deng et al. [116] where a preheat temperature of 1000 °C was used confirmed this. They observed a highly homogeneous chemical composition whereby applying a solution treatment seems redundant. Also, no γ'' formed during deposition until after deposition of last layer, where cooling to RT resulted in a homogenous distribution of γ'' across the build height with high hardness. It should be noted that processing at such high temperatures may result in a heavily sintered powder surrounding the build [344]. Using lower preheat temperatures (slightly below 1000 °C) is reported to cause γ'' precipitation with size and morphology being a function of the build height [192].

The control of other parameters, such as the interlayer dwell time (idle time) and interpass temperature within a reasonable range, can also help mitigate heterogeneity. The strategy for controlling these parameters is to reduce heat accumulation in layers, reduce thermal gradients, and ensure constant thermal conditions (e.g., cooling rate) along the build height. A shorter or no interlayer dwell time usually causes a high thermal gradient and a high variation in thermal conditions along the build compared to a longer time [345]. This is attributed to the increase in heat accumulation of layers with build height as no sufficient time is available for previous layers to cool before deposition of the next layer. A strong influence of interlayer dwell time is observed in the melt pool depth of alloys and reported to increase along the build height for short interlayer dwell time [346]. The dwell time also influences the grain morphology and orientation. During L-DED, Guévenoux et al. [347] compared the microstructure of IN718 with and without interlayer dwell time. They reported a highly textured microstructure with a sharp gradient, which consisted of large columnar grains across layers for samples without dwell time. The application of dwell time caused a negligible gradient in microstructure and a fine grain that did not cross the layers. Increasing dwell time is also reported to decrease the residual stress and defect formation in L-DED IN625 [204] and CM247LC [348], respectively.

The interpass temperature is crucial for wire-based DED processes. Like the preheat temperature in E-PBF, it can reduce the thermal stresses during wire-based DED. Zhao et al. [349] showed that decreasing the interpass temperature via increasing the idle time causes a reduction in residual stress of the wire-based DED process. Also, using the interpass cooling strategy to reduce the interpass temperature has been proven to refine the microstructure. Zhang et al. [350] used interpass cooling to reduce the interpass temperature in IN718 fabricated with wire-based DED. The reduced temperature eliminated the heat influence of the previously deposited layer which ensured a consistent heat input in the top, middle and bottom of the build. This led to a constant solidification rate causing a uniform size distribution of fine dendrite arm spacing along the build. However, it should be noted that adding a dwell time increases production time and cost and hence is not a sustainable option for the industry.

In addition to post-processing heat treatment techniques and process parameter optimization, the use of ultrasonic vibration during AM can help reduce heterogeneity in the microstructure. Ultrasonic vibration is a vibratory treatment technique mainly used in traditional metal solidification processes such as arc welding and casting to refine the microstructure, and decrease porosity and micro-segregation [351,352]. In Ni-based superalloys, this technique has been used by several researchers to control hot crack problems via grain refinements, eutectic phase reduction, and increase in chemical homogeneity [353,354]. However, very few studies have been reported using this method in AM. Li et al. [355] introduced ultrasonic micro-forging treatment (UMFT) during L-DED of GH3039 Ni-based superalloy to achieve homogeneous microstructure, reduce porosities and cracks, and enhance mechanical properties. Additionally, Ning et al. [356] investigated the microstructure of IN718 fabricated by an ultrasonic vibration-assisted L-DED. They reported a reduction in defects, grain and dendrite spacing, fragmentation of detrimental phases, and homogeneous distribution of chemical content. These features enhanced the microhardness of the fabricated parts.

5.3. Potential advantages of heterogeneities

Although the heterogeneities in AM structures tend to limit the extensive use of AM parts for structural purposes without further post-processing techniques, it must be mentioned that heterogeneities may also have some potential benefits. The concept of functionally graded materials (FGMs) is one example where microstructural heterogeneities may be desirable [357]. FGMs are materials that exhibit a variation in properties due to the gradual changes in microstructure (or composition). In AM, this concept has recently gained attention as it can be used to replace sharp interfaces in dissimilar welded structures with gradient interfaces that permit smooth transitions of properties [358,359]. An as-fabricated Ni-based superalloy with a gradient in hardness and strength may be able to replace dissimilar structures requiring higher surface hardness and a softer core. High surface hardness can provide adequate wear resistance, whereas a soft core can absorb stresses without cracking, leading to high fracture resistance. In aerospace, this may be used as a turbine blade to prolong fatigue life as high surface hardness will impede fatigue growth of surface cracks.

6. Concluding remarks

The main conclusions from the comprehensive review of the existing literature on the heterogeneities in the microstructure and mechanical properties of AM Ni-based superalloys can be summarized as follows:

6.1. Microstructural properties

- Microstructural heterogeneities are usually reported to occur throughout the build height of AM Ni-based superalloys. The heterogeneities in the as-fabricated microstructure include the heterogeneity in the chemical composition, phase constitution, porosities, grain and dendrite morphology, and the morphology of the solid-state precipitates.
- The primary reason for the heterogeneity in the as-fabricated parts is the variation in thermal conditions in the build caused by the complex thermal histories of AM. The complex thermal histories experienced in the build may involve rapid heating, cooling, and high thermal gradients that trigger a variation in solidification rates and multiple melting and reheating cycles.
- The heterogeneities are alloy and AM process dependent. Precipitation-hardened superalloys exhibit a higher degree of heterogeneity compared to solid solution strengthened alloys. The high deposition and low cooling rate in DED cause higher heterogeneity in the solidification microstructure compared to PBF. The elevated build temperature in E-PBF is responsible for the high heterogeneity in nanoscale precipitates.
- The main heterogeneity in the dendritic structure is an increase in the dendrite width with build height and a transition from columnar to equiaxed dendrite along the build. These are attrib-

uted to the changes in solidification conditions where a higher cooling rate and steeper thermal gradient are experienced in the bottom of the build compared to the middle and top.

- AM Ni-based superalloys are characterized by heterogeneous grain structures, including competitively grown columnar grains alongside equiaxed grains, a significant increase in size and/or width of the columnar grains along the build height, and a transition in grain morphology from columnar to equiaxed. The typical epitaxially grown columnar grain structure is due to the rapid solidification rate, high thermal gradients, and heat loss towards the substrate. The changes in solidification conditions during deposition is responsible for the heterogeneity in the morphology of grains.
- Heterogeneity in composition originates either from the AM process condition during solidification, or the in-situ heat treatment mainly triggered by the substrate's elevated temperature. The process condition-induced heterogeneity involves the elemental loss in the build via evaporation during deposition upon using a high beam power density. The compositional heterogeneity that occurs during solidification consists of the variation in elemental segregation in the interdendritic regions along the build as it depends on the solidification condition. The elevated substrate temperature in E-PBF acts as *in-situ* heat treatment and changes the matrix composition (especially Nb content) along the build direction of as-fabricated IN625 or IN718 through the melting of phases with low melting points such as Laves.
- Porosities in AM builds are inhomogeneously distributed. Irregular-shaped pores are located along the fusion lines between layers and at the melt pools boundaries, while spherical pores are mostly found closer to the interior of the melt pools. Pore distributions across the build (from edge to edge) and along the build height are inhomogeneous and mainly influenced by the AM process parameters.
- Solidification phases such as Laves in AM builds of IN718 and IN625 are distributed heterogeneously. The Laves phase volume fraction is higher in the middle than the bottom and top layers, and the particles coarsen with the build height. These phenomena are attributed to the high cooling rate at the bottom and top layer compared to the middle, and the intrinsic heat treatment from the elevated build temperature during E-PBF.
- The precipitation and morphology of nanoscale precipitates in the build is heterogeneous and mainly determined by the amount of time each deposited layer spends in the precipitation temperature window during deposition or cooling. A longer holding time in the precipitation window means a high phase fraction and/or larger size of the precipitates. The heterogeneities observed include the increase in the volume fraction of nanoscale precipitates away from the dendrite core, towards the interdendritic regions, and an increase in volume fraction and size along the build direction.

6.2. Mechanical properties

- The mechanical properties of AM Ni-based superalloys are determined by their microstructural features, such as dendritic structure, grain morphology, dislocation cell structure, porosities, chemical composition, phases formed during solidification, solid-state precipitates, and presence of nanoscale oxides.
- The heterogeneity in microstructure causes heterogeneity in the mechanical properties currently limiting the practical applications of the as-fabricated parts. The heterogeneities in the mechanical properties include a gradient in hardness, tensile and yield strength, elastic modulus, and creep behavior along the build height.
- The hardness for most builds fabricated with DED, L-PBF, and E-PBF (especially for IN718) decreases along the build direction. This is attributed to the higher amount (volume fraction) of γ' and γ'' precipitates at the bottom compared to the top. This hardness gradient has also, in part, been attributed to a variation in grain size distribution or dendrite width along the build. The hardness in high γ' Ni-based superalloy such as CMSX-4 and IN738 fabricated with E-PBF increases along the build direction due to the larger size of γ' precipitates at the bottom.
- A gradient in yield strength, tensile strength, and elastic modulus exists throughout the build direction of AM Ni-based superalloys. The variation of these properties for most Ni-based superalloys is similar to that of the hardness distribution, which correlates with γ'/γ'', grain, and dendrite heterogeneity. Also, in IN625 and IN718, the variation of the fraction of detrimental Laves and δ phase along the build strongly influence the tensile property heterogeneity such that regions with a higher fraction of these phases show lower strength.
- The creep behavior of AM Ni-based superalloys changes along the build height in correlation with γ' heterogeneity wherein region with finer γ' precipitates creep faster than those with coarser precipitates.
- The anisotropy in mechanical properties such as creep, tensile, and fatigue for AM Ni-based superalloys is caused by the significantly different microstructural evolutions in directions parallel and perpendicular to the build direction. For most AM Ni-based superalloy samples loaded perpendicular to the build direction, higher tensile strength and elastic modulus, inferior creep behavior, and a higher fatigue endurance were typically observed. Under certain circumstances, such as the presence of string-like pores and coarser interdendritic δ-phase precipitates aligned parallel to the build direction, a different anisotropy behavior, with significant reduction in strength, is observed when loaded perpendicular to the build direction.
- The residual stress distribution in AM Ni-based superalloys is inhomogeneous and mostly influenced by AM process parameters such as scan speed/strategy, hatch spacing, heat input, and build temperature. Its presence, which affects the mechanical property integrity, also leads to heterogeneities in the grain structure by serving as a driving force for static recrystallization during subsequent heat treatments. Residual stress also significantly influences the solid-state phase transformation kinetics by enhancing the nucleation of TCP and other phases in the build.

In conclusion, the heterogeneity in AM Ni-based superalloys remains a major challenge that, if not resolved, will down the more widespread adoption of AM for producing critical parts. So far, the use of post-processing techniques such as heat treatments, hot isostatic pressing (HIP), and processing parameter optimization during deposition have helped to overcome some of the discussed challenges. The post-processing heat treatments employed include solution annealing, followed by double aging. Solution annealing causes the dissolution of several solidification phases such as Laves, δ, and other micro-segregate phases and ensures compositional homogenization. The subsequent aging treatment promotes the adequate precipitation and uniform distribution of fine strengthening nanoscale precipitates throughout a build. HIP eliminates defects such as pores, voids, and internal cracks in the build. It also enables compositional homogenization and, depending on the alloy, may promote the precipitation and uniform distribution fine strengthening nanoscale precipitates throughout the build. Better control of AM processing parameters such as beam power, preheat temperatures, interlayer dwell time and temperature, scan speed, and scan strategies can be used to avoid (or even custom-

design) heterogeneities in the microstructure, such as the grain morphology and reduce porosity and residual stress in the build. The addition of inoculants or nanoparticles to powder and the use of vibratory treatment technique such as ultrasonic vibration can help mitigate microstructure heterogeneities. In the design of functionally graded materials for structural purposes is a potential field where heterogeneity in AM Ni-based superalloys may unlock new properties if it can be harnessed to engineer microstructural gradients.

CRediT authorship contribution statement

Nana Kwabena Adomako: Conceptualization, Investigation, Writing – original draft, Visualization. **Nima Haghdadi:** Conceptualization, Writing – review & editing, Supervision. **Sophie Primig:** Conceptualization, Resources, Writing – review & editing, Supervision, Funding acquisition.

Data availability

No data was used for the research described in the article.

Declaration of Competing Interest

The authors declare that they have no known competing financial interests or personal relationships that could have appeared to influence the work reported in this paper.

Acknowledgements

Funding from the AUSMURI program administered by the Australia's Department of Industry, Science, Energy and Resources is acknowledged. Sophie Primig is supported under UNSW Scientia Fellowship scheme and Nana Adomako by the UNSW Scientia PhD Fellowship scheme. Fruitful discussions with Prof. S.S. Babu (University of Tennessee, Knoxville) and Prof. S.P. Ringer and Prof. X.Z. Liao (The University of Sydney) are acknowledged.

References

[1] J.D. Whittenberger, Superalloys II, Mater. Manuf. Process. 7 (1992) 463–468.
[2] M. Das, P.K. Sen, G. Sahu, R. Sharma, S. Bohidar, Review on High Performance Nickel based Super Alloy, Int. J. Eng. Manag. Res. 5 (2015) 286–291.
[3] M. Durand-Charre, The Microstructure of Superalloys, Gordon Breach Sci. Publ, Amsterdam, 1997.
[4] H. Fecht, D. Furrer, Processing of nickel-base superalloys for turbine engine disc applications, Adv. Eng. Mater. 2 (2000) 777–787, https://doi.org/10.1002/1527-2648(200012)2:12<777::AID-ADEM777>3.0.CO;2-R.
[5] M.M. Attallah, R. Jennings, X. Wang, L.N. Carter, Additive manufacturing of Ni-based superalloys: The outstanding issues, MRS Bull. 41 (2016) 758–764, https://doi.org/10.1557/mrs.2016.211.
[6] M.J. Donachie, S.J. Donachie, Superalloys: a Technical Guide, second ed., ASM Int. (2002).
[7] W.J. Sames, K.A. Unocic, R.R. Dehoff, T. Lolla, S.S. Babu, Thermal effects on microstructural heterogeneity of Inconel 718 materials fabricated by electron beam melting, J. Mater. Res. 29 (2014) 1920–1930, https://doi.org/10.1557/jmr.2014.140.
[8] E. Hosseini, V.A. Popovich, A review of mechanical properties of additively manufactured Inconel 718, Addit. Manuf. 30 (2019), https://doi.org/10.1016/j.addma.2019.100877 100877.
[9] H. Qi, M. Azer, A. Ritter, Studies of standard heat treatment effects on microstructure and mechanical properties of laser net shape manufactured INCONEL 718, Metall. Mater. Trans. A Phys. Metall. Mater. Sci. 40 (2009) 2410–2422, https://doi.org/10.1007/s11661-009-9949-3.
[10] T.M. Pollock, S. Tin, Nickel-based superalloys for advanced turbine engines: Chemistry, microstructure, and properties, J. Propuls. Power. 22 (2006) 361–374, https://doi.org/10.2514/1.18239.
[11] J.F. Radavich, THE PHYSICAL METALLURGY OF CAST AND WROUGHT ALLOY 718 Cast Alloy 718, (1989).
[12] H. Wu, X. Zhuang, Y. Nie, Y. Li, L. Jiang, Effect of heat treatment on mechanical property and microstructure of a powder metallurgy nickel-based superalloy, Mater. Sci. Eng. A. 754 (2019) 29–37, https://doi.org/10.1016/j.msea.2019.03.064.
[13] P. Caron, T. Khan, Improvement of Creep strength in a nickel-base single-crystal superalloy by heat treatment, Mater. Sci. Eng. 61 (1983) 173–184, https://doi.org/10.1016/0025-5416(83)90199-4.
[14] G.R. Thellaputta, P.S. Chandra, C.S.P. Rao, Machinability of Nickel Based Superalloys: A Review, Mater. Today Proc. 4 (2017) 3712–3721, https://doi.org/10.1016/j.matpr.2017.02.266.
[15] T. Debroy, H.L. Wei, J.S. Zuback, T. Mukherjee, J.W. Elmer, J.O. Milewski, A.M. Beese, A. Wilson-heid, A. De, W. Zhang, Additive manufacturing of metallic components – Process, structure and properties, Prog. Mater. Sci. 92 (2018) 112–224, https://doi.org/10.1016/j.pmatsci.2017.10.001.
[16] S. Sanchez, P. Smith, Z. Xu, G. Gaspard, C.J. Hyde, W.W. Wits, I.A. Ashcroft, H. Chen, A.T. Clare, Powder Bed Fusion of nickel-based superalloys: A review, Int. J. Mach. Tools Manuf. 165 (2021), https://doi.org/10.1016/j.ijmachtools.2021.103729.
[17] V.A. Popovich, E.V. Borisov, A.A. Popovich, V.S. Sufiiarov, D.V. Masaylo, L. Alzina, Functionally graded Inconel 718 processed by additive manufacturing: Crystallographic texture, anisotropy of microstructure and mechanical properties, Mater. Des. 114 (2017) 441–449, https://doi.org/10.1016/j.matdes.2016.10.075.
[18] X. Wang, L.N. Carter, B. Pang, M.M. Attallah, M.H. Loretto, Microstructure and yield strength of SLM-fabricated CM247LC Ni-Superalloy, Acta Mater. 128 (2017) 87–95, https://doi.org/10.1016/j.actamat.2017.02.007.
[19] X. Gong, K. Chou, Microstructure of Inconel 718 by Selective Laser Melting, 144th Annu. Meet. Exhib. Orlando, Florida, 15–19 March. (2015) 461–468.
[20] Y.L. Kuo, T. Nagahari, K. Kakehi, The effect of post-processes on the microstructure and creep properties of Alloy718 built up by selective laser melting, Materials (Basel). 11 (2018), https://doi.org/10.3390/ma11060996.
[21] H. Hilal, R. Lancaster, S. Jeffs, J. Boswell, D. Stapleton, G. Baxter, The influence of process parameters and build orientation on the creep behaviour of a laser powder bed fused ni-based superalloy for aerospace applications, Materials (Basel). 12 (2019), https://doi.org/10.3390/ma12091390.
[22] N. Haghdadi, C. Ledermueller, H. Chen, Z. Chen, Q. Liu, X. Li, G. Rohrer, X. Liao, S. Ringer, S. Primig, Evolution of microstructure and mechanical properties in 2205 duplex stainless steels during additive manufacturing and heat treatment, Mater. Sci. Eng. A. 835 (2022), https://doi.org/10.1016/j.msea.2022.142695 142695.
[23] R. DeMott, N. Haghdadi, X. Liao, S.P. Ringer, S. Primig, 3D characterization of microstructural evolution and variant selection in additively manufactured Ti-6Al-4 V, J. Mater. Sci. 56 (2021) 14763–14782, https://doi.org/10.1007/s10853-021-06216-2.
[24] S.S. Babu, N. Raghavan, J. Raplee, S.J. Foster, C. Frederick, M. Haines, R. Dinwiddie, M.K. Kirka, A. Plotkowski, Y. Lee, R.R. Dehoff, Additive Manufacturing of Nickel Superalloys: Opportunities for Innovation and Challenges Related to Qualification, Metall. Mater. Trans. A Phys. Metall. Mater. Sci. 49 (2018) 3764–3780, https://doi.org/10.1007/s11661-018-4702-4.
[25] Y. Tian, D. McAllister, H. Colijn, M. Mills, D. Farson, M. Nordin, S. Babu, Rationalization of microstructure heterogeneity in INCONEL 718 builds made by the direct laser additive manufacturing process, Metall. Mater. Trans. A Phys. Metall. Mater. Sci. 45 (2014) 4470–4483, https://doi.org/10.1007/s11661-014-2370-6.
[26] S. Li, Q. Wei, Y. Shi, C.K. Chua, Z. Zhu, D. Zhang, Microstructure Characteristics of Inconel 625 Superalloy Manufactured by Selective Laser Melting, J. Mater. Sci. Technol. 31 (2015) 946–952, https://doi.org/10.1016/j.jmst.2014.09.020.
[27] M. Gäumann, C. Bezençon, P. Canalis, W. Kurz, Single-crystal laser deposition of superalloys: Processing-microstructure maps, Acta Mater. 49 (2001) 1051–1062, https://doi.org/10.1016/S1359-6454(00)00367-0.
[28] N. Haghdadi, H. Chen, Z. Chen, S.S. Babu, X. Liao, S.P. Ringer, S. Primig, Intergranular precipitation and chemical fluctuations in an additively manufactured 2205 duplex stainless steel, Scr. Mater. 219 (2022), https://doi.org/10.1016/j.scriptamat.2022.114894 114894.
[29] T. Vilaro, C. Colin, J.D. Bartout, L. Nazé, M. Sennour, Microstructural and mechanical approaches of the selective laser melting process applied to a nickel-base superalloy, Mater. Sci. Eng. A. 534 (2012) 446–451, https://doi.org/10.1016/j.msea.2011.11.092.
[30] A. Deshpande, S.D. Nath, S. Atre, K. Hsu, Effect of post processing heat treatment routes on microstructure and mechanical property evolution of haynes 282 Ni-based superalloy fabricated with selective laser melting (SLM), Metals (Basel). 10 (2020) 1–13, https://doi.org/10.3390/met10050629.
[31] M. Ramsperger, R.F. Singer, C. Körner, Microstructure of the Nickel-Base Superalloy CMSX-4 Fabricated by Selective Electron Beam Melting, Metall. Mater. Trans. A Phys. Metall. Mater. Sci. 47 (2016) 1469–1480, https://doi.org/10.1007/s11661-015-3300-y.
[32] Z. Li, J. Chen, S. Sui, C. Zhong, X. Lu, X. Lin, The microstructure evolution and tensile properties of Inconel 718 fabricated by high-deposition-rate laser directed energy deposition, Addit. Manuf. 31 (2020), https://doi.org/10.1016/j.addma.2019.100941 100941.
[33] W. Xu, M. Brandt, S. Sun, J. Elambasseril, Q. Liu, K. Latham, K. Xia, M. Qian, Additive manufacturing of strong and ductile Ti-6Al-4V by selective laser melting via in situ martensite decomposition, Acta Mater. 85 (2015) 74–84, https://doi.org/10.1016/j.actamat.2014.11.028.
[34] S.S. Al-Bermani, M.L. Blackmore, W. Zhang, I. Todd, The origin of microstructural diversity, texture, and mechanical properties in electron beam melted Ti-6Al-4V, Metall. Mater. Trans. A Phys. Metall. Mater. Sci. 41 (2010) 3422–3434, https://doi.org/10.1007/s11661-010-0397-x.

[35] P.L. Stephenson, N. Haghdadi, R. DeMott, X.Z. Liao, S.P. Ringer, S. Primig, Effect of scanning strategy on variant selection in additively manufactured Ti-6Al-4V, Addit. Manuf. 36 (2020), https://doi.org/10.1016/j.addma.2020.101581 101581.
[36] S.H. Sun, Y. Koizumi, S. Kurosu, Y.P. Li, H. Matsumoto, A. Chiba, Build direction dependence of microstructure and high-temperature tensile property of Co-Cr-Mo alloy fabricated by electron beam melting, Acta Mater. 64 (2014) 154–168, https://doi.org/10.1016/j.actamat.2013.10.017.
[37] S.H. Sun, Y. Koizumi, S. Kurosu, Y.P. Li, A. Chiba, Phase and grain size inhomogeneity and their influences on creep behavior of Co-Cr-Mo alloy additive manufactured by electron beam melting, Acta Mater. 86 (2015) 305–318, https://doi.org/10.1016/j.actamat.2014.11.012.
[38] Y.K. Kim, K.A. Lee, Direct energy deposition of high strength austenitic stainless steel matrix nanocomposite with superior ductility: Microstructure, tensile properties, and deformation behavior, Mater. Charact. 179 (2021), https://doi.org/10.1016/j.matchar.2021.111358 111358.
[39] H. Helmer, A. Bauereiß, R.F. Singer, C. Körner, Erratum to: 'Grain structure evolution in Inconel 718 during selective electron beam melting' (Materials Science & Engineering A (2016) 668 (180–187 (S0921509316305536) (10.1016/j.msea.2016.05.046)), Mater. Sci. Eng. A. 676 (2016) 546. 10.1016/j.msea.2016.09.016.
[40] X. Wang, T. Keya, K. Chou, Build Height Effect on the Inconel 718 Parts Fabricated by Selective Laser Melting, Procedia Manuf. 5 (2016) 1006–1017, https://doi.org/10.1016/j.promfg.2016.08.089.
[41] N. Haghdadi, E. Whitelock, B. Lim, H. Chen, X. Liao, S.S. Babu, S.P. Ringer, S. Primig, Multimodal γ′ precipitation in Inconel-738 Ni-based superalloy during electron-beam powder bed fusion additive manufacturing, J. Mater. Sci. 55 (2020) 13342–13350, https://doi.org/10.1007/s10853-020-04915-w.
[42] B. Lim, H. Chen, Z. Chen, N. Haghdadi, X. Liao, S. Primig, S.S. Babu, A. Breen, S.P. Ringer, Microstructure–property gradients in Ni-based superalloy (Inconel 738) additively manufactured via electron beam powder bed fusion, Addit. Manuf. (2021), https://doi.org/10.1016/j.addma.2021.102121 102121.
[43] P. Karimi, E. Sadeghi, P. Åkerfeldt, J. Ålgårdh, J. Andersson, Influence of successive thermal cycling on microstructure evolution of EBM-manufactured alloy 718 in track-by-track and layer-by-layer design, Mater. Des. 160 (2018) 427–441, https://doi.org/10.1016/j.matdes.2018.09.038.
[44] E. Chauvet, P. Kontis, E.A. Jägle, B. Gault, D. Raabe, C. Tassin, J.J. Blandin, R. Dendievel, B. Vayre, S. Abed, G. Martin, Hot cracking mechanism affecting a non-weldable Ni-based superalloy produced by selective electron Beam Melting, Acta Mater. 142 (2018) 82–94, https://doi.org/10.1016/j.actamat.2017.09.047.
[45] P. Krakhmalev, I. Yadroitsava, G. Fredriksson, I. Yadroitsev, In situ heat treatment in selective laser melted martensitic AISI 420 stainless steels, Mater. Des. 87 (2015) 380–385, https://doi.org/10.1016/j.matdes.2015.08.045.
[46] B. Zhang, P. Wang, Y. Chew, Y. Wen, M. Zhang, P. Wang, G. Bi, J. Wei, Mechanical properties and microstructure evolution of selective laser melting Inconel 718 along building direction and sectional dimension, Mater. Sci. Eng. A. 794 (2020), https://doi.org/10.1016/j.msea.2020.139941 139941.
[47] C. Körner, M. Ramsperger, C. Meid, D. Bürger, P. Wollgramm, M. Bartsch, G. Eggeler, Microstructure and Mechanical Properties of CMSX-4 Single Crystals Prepared by Additive Manufacturing, Metall. Mater. Trans. A Phys. Metall. Mater. Sci. 49 (2018) 3781–3792, https://doi.org/10.1007/s11661-018-4762-5.
[48] B. Lim, H. Chen, K. Nomoto, Z. Chen, A.I. Saville, S. Vogel, A.J. Clarke, A. Paradowska, M. Reid, S. Primig, X. Liao, S.S. Babu, A.J. Breen, S.P. Ringer, Additively manufactured Haynes-282 monoliths containing thin wall struts of varying thicknesses, Addit. Manuf. 59 (2022), https://doi.org/10.1016/j.addma.2022.103120 103120.
[49] M.P. Haines, V.V. Rielli, S. Primig, N. Haghdadi, Powder bed fusion additive manufacturing of Ni-based superalloys: a review of the main microstructural constituents and characterization techniques, J. Mater. Sci. 57 (2022) 14135–14187, https://doi.org/10.1007/s10853-022-07501-4.
[50] A.N. Jinoop, C.P. Paul, K.S. Bindra, Laser-assisted directed energy deposition of nickel super alloys: A review, Proc. Inst. Mech. Eng. Part L J. Mater. Des. Appl. 233 (2019) 2376–2400. 10.1177/1464420719852658.
[51] O. Adegoke, J. Andersson, H. Brodin, R. Pederson, Review of laser powder bed fusion of gamma-prime-strengthened nickel-based superalloys, Metals (Basel). 10 (2020) 1–26, https://doi.org/10.3390/met10080996.
[52] Z. Tian, C. Zhang, D. Wang, W. Liu, X. Fang, D. Wellmann, Y. Zhao, Y. Tian, A review on laser powder bed fusion of inconel 625 nickel-based alloy, Appl. Sci. 10 (2020), https://doi.org/10.3390/app10010081.
[53] A. Kulkarni, Additive Manufacturing of Nickel Based Superalloy (2014) 1–12.
[54] S. Pratheesh Kumar, S. Elangovan, R. Mohanraj, J.R. Ramakrishna, A review on properties of Inconel 625 and Inconel 718 fabricated using direct energy deposition, Mater. Today Proc. (2021). 10.1016/j.matpr.2021.02.566.
[55] B. Graybill, D. Malawey, E. Martinez-franco, Additive Manufacturing of Nickel-Based Superalloys (2019) 1–17.
[56] C.K. Yong, G.J. Gibbons, G. West, A Critical Review of the Material Characteristics of Additive Manufactured IN718 for High Temperature Application, (2020) 1–21. 10.20944/preprints202010.0292.v1.
[57] X. Wang, X. Gong, K. Chou, Review on powder-bed laser additive manufacturing of Inconel 718 parts, Proc. Inst. Mech. Eng. Part B J. Eng. Manuf. 231 (2017) 1890–1903. 10.1177/0954405415619883.
[58] Y. Kok, X.P. Tan, P. Wang, M.L.S. Nai, N.H. Loh, E. Liu, S.B. Tor, Anisotropy and heterogeneity of microstructure and mechanical properties in metal additive manufacturing: A critical review, Mater. Des. 139 (2018) 565–586, https://doi.org/10.1016/j.matdes.2017.11.021.
[59] G.M. Karthik, H.S. Kim, Heterogeneous Aspects of Additive Manufactured Metallic Parts: A Review, The Korean Institute of Metals and Materials (2021), https://doi.org/10.1007/s12540-020-00931-2.
[60] R. Giraud, Z. Hervier, J. Cormier, G. Saint-Martin, F. Hamon, X. Milhet, J. Mendez, Strain effect on the γ′ dissolution at high temperatures of a nickel-based single crystal superalloy, Metall. Mater. Trans. A Phys. Metall. Mater. Sci. 44 (2013) 131–146, https://doi.org/10.1007/s11661-012-1397-9.
[61] I. Serrano-Munoz, T. Mishurova, T. Thiede, M. Sprengel, A. Kromm, N. Nadammal, G. Nolze, R. Saliwan-Neumann, A. Evans, G. Bruno, The residual stress in as-built Laser Powder Bed Fusion IN718 alloy as a consequence of the scanning strategy induced microstructure, Sci. Rep. 10 (2020) 1–15, https://doi.org/10.1038/s41598-020-71112-9.
[62] R.C. Reed, The Superalloys (2007), https://doi.org/10.1016/S1369-7021(07)70022-6.
[63] A.K. Jena, M.C. Chaturvedi, The role of alloying elements in the design of nickel-base superalloys, J. Mater. Sci. 19 (1984) 3121–3139, https://doi.org/10.1007/BF00549796.
[64] R. Cozar, A. Pineau, Morphology of gamma prime and gamma double prime precipitates and thermal stability of Inconel 718 type alloys, Metall. Mater. Trans. B. 4 (1973) 47–59. https://link.springer.com/content/pdf/10.1007%2FBF02649604.pdf%0Ahttps://doi.org/10.1007/BF02649604.
[65] J.M. Oblak, J.E. Doherty, A.F. Giamei, B.H. Kear, Precipitation of γ in the γ′of nickel-base superalloys, Metall. Mater. Trans. B Process Metall. Mater. Process. Sci. 5 (1974) 1252–1255, https://doi.org/10.1007/BF02644342.
[66] S. Tin, T.M. Pollock, Nickel-Based Superalloys for Blade Application: Production, Performance and Application, Encycl. Aerosp. Eng. (2010), https://doi.org/10.1002/9780470686652.eae218.
[67] F.L. VerSnyder, M.E. Shank, Development of Columnar Grain and Single Crystal High-Temperature Materials Through Directional Solidification, Mater. Sci. Eng. 6 (1970) 213–247.
[68] R. Buerstmayr, F. Theska, R. Webster, M. Lison-Pick, S. Primig, Correlative analysis of grain boundary precipitates in Ni-based superalloy René 41, Mater. Charact. 178 (2021), https://doi.org/10.1016/j.matchar.2021.111250 111250.
[69] C.M.F. Rae, M.S. Hook, R.C. Reed, The effect of TCP morphology on the development of aluminide coated superalloys, Mater. Sci. Eng. A. 396 (2005) 231–239, https://doi.org/10.1016/j.msea.2005.01.005.
[70] E.J. Pickering, H. Mathur, A. Bhowmik, O.M.D.M. Messé, J.S. Barnard, M.C. Hardy, R. Krakow, K. Loehnert, H.J. Stone, C.M.F. Rae, Grain-boundary precipitation in Allvac 718Plus, Acta Mater. 60 (2012) 2757–2769, https://doi.org/10.1016/j.actamat.2012.01.042.
[71] C.M.F. Rae, R.C. Reed, The precipitation of topologically close-packed phases in rhenium-containing superalloys, Acta Mater. 49 (2001) 4113–4125, https://doi.org/10.1016/S1359-6454(01)00265-8.
[72] S.T. Wlodek, The Structure of IN100, Trans. ASM. 57 (1964) 110–119.
[73] J.D. Nystrom, T.M. Pollock, W.H. Murphy, A. Garg, Discontinuous Cellular Precipitation in a High-Refractory Nickel-Base Superalloy, Metall, Mater. Trans. 28A (1997) 2443–2452.
[74] E.W. Ross, Rene 100-A Sigma-Free Turbine Blade Alloy, J. Met. 19 (1967) 12–14.
[75] F. Theska, A. Stanojevic, B. Oberwinkler, S. Primig, Microstructure-property relationships in directly aged Alloy 718 turbine disks, Mater. Sci. Eng. A. 776 (2020), https://doi.org/10.1016/j.msea.2020.138967 138967.
[76] C.T. Sims, N.S. Stoloff, W.C. Hagel, Superalloys II, Superalloys II. (1987) 615. http://books.google.co.uk/books/about/Superalloys_II.html?id=kqZTAAAAMAAJ&pgis=1.
[77] K. Kawagishi, A. Yeh, T. Yokokawa, T. Kobayashi, Y. Koizumi, H. Harada, DEVELOPMENT OF AN OXIDATION-RESISTANT HIGH-STRENGTH SIXTH-(2012) 189–195.
[78] L.M. Suave, J. Cormier, P. Villechaise, A. Soula, Z. Hervier, D. Bertheau, J. Laigo, Microstructural evolutions during thermal aging of alloy 625: Impact of temperature and forming process, Metall. Mater. Trans. A Phys. Metall. Mater. Sci. 45 (2014) 2963–2982, https://doi.org/10.1007/s11661-014-2256-7.
[79] Additive manufacturing market analysis by material type, (2020) 230.
[80] ResearchAndMarkets.com, $23.75 Billion Additive Manufacturing Market Analysis, 2020-2027, ResearchAndMarkets.Com. (2020). https://www.businesswire.com/news/home/20201221005320/en/23.75-Billion-Additive-Manufacturing-Market-Analysis-2020-2027—ResearchAndMarkets.com.
[81] C.O. Brown, E.M. Breinan, B.H. Kear, METHOD FOR FABRICATING ARTICLES BYSEQUENTIAL LAYER DEPOSITION, United States Pat. 19 (1982) 1–4.
[82] A. Munaz, R.K. Vadivelu, J. St, M. John, H. Barton, N.T.N. Kamble, Three-dimensional printing of biological matters, J. Sci. Adv. Mater. Devices. 1 (2016) 1–17, https://doi.org/10.1016/j.jsamd.2016.04.001.
[83] X. Wu, A review of laser fabrication of metallic engineering components and of materials, Mater. Sci. Technol. 23 (2007) 631–640, https://doi.org/10.1179/174328407X179593.
[84] X. Wang, T. Laoui, To cite this document : Lasers and materials in selective laser sintering 23 (2006) 357–371.
[85] C.L.A. Leung, R. Tosi, E. Muzangaza, S. Nonni, P.J. Withers, P.D. Lee, Effect of preheating on the thermal, microstructural and mechanical properties of selective electron beam melted Ti-6Al-4V components, Mater. Des. 174 (2019), https://doi.org/10.1016/j.matdes.2019.107792 107792.
[86] S. Griffiths, H. Ghasemi Tabasi, T. Ivas, X. Maeder, A. De Luca, K. Zweiacker, R. Wróbel, J. Jhabvala, R.E. Logé, C. Leinenbach, Combining alloy and process

modification for micro-crack mitigation in an additively manufactured Ni-base superalloy, Addit. Manuf. 36 (2020), https://doi.org/10.1016/j.addma.2020.101443.
[87] W.J. Sames, F.A. List, S. Pannala, R.R. Dehoff, S.S. Babu, The metallurgy and processing science of metal additive manufacturing, Int. Mater. Rev. 61 (2016) 315–360, https://doi.org/10.1080/09506608.2015.1116649.
[88] G.Y. Baek, G.Y. Shin, K.Y. Lee, D.S. Shim, Mechanical properties of tool steels with high wear resistance via directed energy deposition, Metals (Basel). 9 (2019), https://doi.org/10.3390/met9030282.
[89] M. Moyle, C. Ledermueller, Z. Zou, S. Primig, N. Haghdadi, Multi-scale characterisation of microstructure and texture of 316L stainless steel manufactured by laser powder bed fusion, Mater. Charact. 184 (2022), https://doi.org/10.1016/j.matchar.2021.111663 111663.
[90] Ø. Grong, Metallurgical Modelling of Welding, (2nd ed.)., 1997.
[91] W. Kurz, D.J. Fisher, Fundamentals of Solidification, CRC Press, 1998.
[92] A.R. Balachandramurthi, J. Olsson, J. Ålgårdh, A. Snis, J. Moverare, R. Pederson, Microstructure tailoring in Electron Beam Powder Bed Fusion additive manufacturing and its potential consequences, Results Mater. 1 (2019), https://doi.org/10.1016/j.rinma.2019.100017 100017.
[93] N. Raghavan, R. Dehoff, S. Pannala, S. Simunovic, M. Kirka, J. Turner, N. Carlson, S.S. Babu, Numerical modeling of heat-transfer and the in fl uence of process parameters on tailoring the grain morphology of IN718 in electron beam additive manufacturing *, Acta Mater. 112 (2016) 303–314, https://doi.org/10.1016/j.actamat.2016.03.063.
[94] M.S. Moyle, N. Haghdadi, W.J. Davids, X.Z. Liao, S.P. Ringer, S. Primig, Evidence of in-situ Cu clustering as a function of laser power during laser powder bed fusion of 17–4 PH stainless steel, Scr. Mater. 219 (2022), https://doi.org/10.1016/j.scriptamat.2022.114896 114896.
[95] N. Haghdadi, R. DeMott, P.L. Stephenson, X.Z. Liao, S.P. Ringer, S. Primig, Five-parameter characterization of intervariant boundaries in additively manufactured Ti-6Al-4V, Mater. Des. 196 (2020), https://doi.org/10.1016/j.matdes.2020.109177 109177.
[96] T. Mukherjee, J.S. Zuback, T. Debroy, Printability of alloys for additive manufacturing (2016) 1–8, https://doi.org/10.1038/srep19717.
[97] N.K. Adomako, G. Shin, N. Park, K. Park, J.H. Kim, Laser dissimilar welding of CoCrFeMnNi-high entropy alloy and duplex stainless steel, J. Mater. Sci. Technol. 85 (2021) 95–105, https://doi.org/10.1016/j.jmst.2021.02.003.
[98] J.P. Oliveira, A.D. LaLonde, J. Ma, Processing parameters in laser powder bed fusion metal additive manufacturing, Mater. Des. 193 (2020) 1–12, https://doi.org/10.1016/j.matdes.2020.108762.
[99] N. Haghdadi, M. Laleh, M. Moyle, S. Primig, Additive manufacturing of steels: a review of achievements and challenges, J. Mater. Sci. 56 (2021) 64–107, https://doi.org/10.1007/s10853-020-05109-0.
[100] M. Ramsperger, C. Körner, Selective Electron Beam Melting of the Single Crystalline Nickel-Base Superalloy CMSX-4®: From Columnar Grains to a Single Crystal, Superalloys, Proc. 13th Intenational Symp, Superalloys. 2016 (2016) 341–349, https://doi.org/10.1002/9781119075646.
[101] I. Gibson, D. Rosen, B. Stucker, Additive manufacturing technologies: 3D printing, rapid prototyping, and direct digital manufacturing, second edition, Addit. Manuf. Technol. 3D Printing, Rapid Prototyping, Direct Digit. Manuf. Second Ed. (2015) 1–498. 10.1007/978-1-4939-2113-3.
[102] I. Gibson, D.W. Rosen, B. Stucker, Additive manufacturing technologies: Rapid prototyping to direct digital manufacturing, Addit. Manuf. Technol. Rapid Prototyp. to Direct Digit. Manuf. (2010) 1–459, https://doi.org/10.1007/978-1-4419-1120-9.
[103] K. Amato, Comparison of Microstructures and Properties for a Ni-Base Superalloy (Alloy 625) Fabricated by Electron Beam Melting, J. Mater. Sci. Res. 1 (2012), https://doi.org/10.5539/jmsr.v1n2p3.
[104] J.-P. Kruth, M.C. Leu, T. Nakagawa, Progress in Additive Manufacturing and Rapid Prototyping, CIRP Ann. 47 (1998) 525–540, https://doi.org/10.1016/S0007-8506(07)63240-5.
[105] R.J. Moat, A.J. Pinkerton, L. Li, P.J. Withers, M. Preuss, Residual stresses in laser direct metal deposited Waspaloy, Mater. Sci. Eng. A. 528 (2011) 2288–2298, https://doi.org/10.1016/j.msea.2010.12.010.
[106] C. Li, Z.Y. Liu, X.Y. Fang, Y.B. Guo, Residual Stress in Metal Additive Manufacturing, Procedia CIRP. 71 (2018) 348–353, https://doi.org/10.1016/j.procir.2018.05.039.
[107] Y. Lu, S. Wu, Y. Gan, T. Huang, C. Yang, L. Junjie, J. Lin, Study on the microstructure, mechanical property and residual stress of SLM Inconel-718 alloy manufactured by differing island scanning strategy, Opt. Laser Technol. 75 (2015) 197–206, https://doi.org/10.1016/j.optlastec.2015.07.009.
[108] J. Song, L. Zhang, W. Wu, B. He, X. Ni, J. Xu, G. Zhu, Q. Yang, T. Wang, L. Lu, Understanding processing parameters affecting residual stress in selective laser melting of Inconel 718 through numerical modeling, J. Mater. Res. 34 (2019) 1395–1404, https://doi.org/10.1557/jmr.2018.504.
[109] T. Hassel, Properties and anisotropy behaviour of a nickel base alloy material produced by robot-based wire and arc additive manufacturing (2020) 1921–1931.
[110] J.P. Oliveira, T.G. Santos, R.M. Miranda, Revisiting fundamental welding concepts to improve additive manufacturing: From theory to practice, Prog. Mater. Sci. 107 (2019), https://doi.org/10.1016/j.pmatsci.2019.100590 100590.
[111] D. Zhang, Z. Feng, C. Wang, W. Wang, Z. Liu, W. Niu, Comparison of microstructures and mechanical properties of Inconel 718 alloy processed by selective laser melting and casting, Mater. Sci. Eng. A. 724 (2018) 357–367, https://doi.org/10.1016/j.msea.2018.03.073.
[112] C. Kumara, A.R. Balachandramurthi, S. Goel, F. Hanning, J. Moverare, Toward a better understanding of phase transformations in additive manufacturing of Alloy 718, Materialia. 13 (2020), https://doi.org/10.1016/j.mtla.2020.100862.
[113] Y.J. Liang, A. Li, X. Cheng, X.T. Pang, H.M. Wang, Prediction of primary dendritic arm spacing during laser rapid directional solidification of single-crystal nickel-base superalloys, J. Alloys Compd. 688 (2016) 133–142, https://doi.org/10.1016/j.jallcom.2016.06.289.
[114] T. Mukherjee, V. Manvatkar, A. De, T. DebRoy, Dimensionless numbers in additive manufacturing, J. Appl. Phys. 121 (2017), https://doi.org/10.1063/1.4976006 064904.
[115] Y.C. Yeoh, G. Macchi, E. Jain, B. Gaskey, S. Raman, G. Tay, D. Verdi, A. Patran, A. M. Grande, M. Seita, Multiscale microstructural heterogeneity and mechanical property scatter in Inconel 718 produced by directed energy deposition, J. Alloys Compd. 887 (2021), https://doi.org/10.1016/j.jallcom.2021.161426 161426.
[116] D. Deng, J. Moverare, R.L. Peng, H. Söderberg, Microstructure and anisotropic mechanical properties of EBM manufactured Inconel 718 and effects of post heat treatments, Mater. Sci. Eng. A. 693 (2017) 151–163, https://doi.org/10.1016/j.msea.2017.03.085.
[117] X. Wang, K. Chou, Effects of thermal cycles on the microstructure evolution of Inconel 718 during selective laser melting process, Addit. Manuf. 18 (2017) 1–14, https://doi.org/10.1016/j.addma.2017.08.016.
[118] K. Wang, D. Du, G. Liu, Z. Pu, B. Chang, J. Ju, Microstructure and mechanical properties of high chromium nickel-based superalloy fabricated by laser metal deposition, Mater. Sci. Eng. A. 780 (2020), https://doi.org/10.1016/j.msea.2020.139185.
[119] D.-G. Ahn, Directed Energy Deposition (DED) Process: State of the Art, Int. J. Precis. Eng. Manuf. Technol. 8 (2021) 703–742, https://doi.org/10.1007/s40684-020-00302-7.
[120] Jose Alberto Muñiz-Lerma, Yuan Tian, Xianglong Wang, R. Gauvin, Mathieu Brochu, Microstructure evolution of Inconel 738 fabricated by pulsed laser powder bed fusion, Prog. Addit. Manuf. 4 (2019) 97–107.
[121] D. Bürger, A.B. Parsa, M. Ramsperger, C. Körner, G. Eggeler, Creep properties of single crystal Ni-base superalloys (SX): A comparison between conventionally cast and additive manufactured CMSX-4 materials, Mater. Sci. Eng. A. 762 (2019), https://doi.org/10.1016/j.msea.2019.138098.
[122] K.A. Unocic, M.M. Kirka, E. Cakmak, D. Greeley, A.O. Okello, S. Dryepondt, Evaluation of additive electron beam melting of haynes 282 alloy, Mater. Sci. Eng. A. 772 (2020), https://doi.org/10.1016/j.msea.2019.138607 138607.
[123] V.V. Rielli, A. Piglione, M.-S.-S. Pham, S. Primig, On the detailed morphological and chemical evolution of phases during laser powder bed fusion and common post-processing heat treatments of IN718, Addit. Manuf. 50 (2022), https://doi.org/10.1016/j.addma.2021.102540 102540.
[124] M. Xia, D. Gu, C. Ma, H. Chen, H. Zhang, Microstructure evolution, mechanical response and underlying thermodynamic mechanism of multi-phase strengthening WC/Inconel 718 composites using selective laser melting, J. Alloys Compd. 747 (2018) 684–695, https://doi.org/10.1016/j.jallcom.2018.03.049.
[125] T.G. Gallmeyer, S. Moorthy, B.B. Kappes, M.J. Mills, B. Amin-Ahmadi, A.P. Stebner, Knowledge of process-structure-property relationships to engineer better heat treatments for laser powder bed fusion additive manufactured Inconel 718, Addit. Manuf. 31 (2020), https://doi.org/10.1016/j.addma.2019.100977 100977.
[126] S. Kou, Welding metallurgy, Wiley Interscience, New Jersey, 2003. https://www.wiley.com/en-us/Welding+Metallurgy%2C+2nd+Edition-p-9780471434917 (accessed October 7, 2018.
[127] R. Trivedi, W. Kurz, Theory of Microstructural Development During Rapid Solidification., NATO ASI Ser, Ser. E Appl. Sci. 34 (1986) 260–267, https://doi.org/10.1007/978-94-009-4456-5_24.
[128] P.N. Quested, M. McLean, Solidification morphologies in directionally solidified superalloys, Mater. Sci. Eng. 65 (1984) 171–180, https://doi.org/10.1016/0025-5416(84)90210-6.
[129] J.J. Blecher, T.A. Palmer, T. Debroy, Solidification map of a nickel-base alloy, Metall. Mater. Trans. A Phys. Metall, Mater. Sci. 45 (2014) 2142–2151, https://doi.org/10.1007/s11661-013-2149-1.
[130] N.M. Seo, J.H. Lee, Y.S. Yoo, C.Y. Jo, H. Miyahara, K. Ogi, Solute redistribution during planar and dendritic growth of directionally solidified Ni-base superalloy CMSX-10, Proc. Int. Symp. Superalloys. (2008) 277–286, https://doi.org/10.7449/2008/superalloys_2008_277_286.
[131] A. Segerstark, Additive Manufacturing using Alloy 718 Powder, 2015. http://hv.diva-portal.org/smash/get/diva2:882458/FULLTEXT01.pdf.
[132] M. Godec, S. Malej, D. Feizpour, M. Donik, D. Balažic, L. Klobčar, M. Pambaguian, A.K. Conradi, Hybrid additive manufacturing of Inconel 718 for future space applications, Mater. Charact. 172 (2021), https://doi.org/10.1016/j.matchar.2020.110842.
[133] F. Liu, X. Lin, H. Leng, J. Cao, Q. Liu, C. Huang, W. Huang, Microstructural changes in a laser solid forming Inconel 718 superalloy thin wall in the deposition direction, Opt. Laser Technol. 45 (2013) 330–335, https://doi.org/10.1016/j.optlastec.2012.06.028.
[134] F. Xu, Y. Lv, Y. Liu, F. Shu, P. He, B. Xu, Microstructural Evolution and Mechanical Properties of Inconel 625 Alloy during Pulsed Plasma Arc Deposition Process, J. Mater. Sci. Technol. 29 (2013) 480–488, https://doi.org/10.1016/j.jmst.2013.02.010.
[135] L.N. Carter, C. Martin, P.J. Withers, M.M. Attallah, The influence of the laser scan strategy on grain structure and cracking behaviour in SLM powder-bed

fabricated nickel superalloy, J. Alloys Compd. 615 (2014) 338–347, https://doi.org/10.1016/j.jallcom.2014.06.172.
[136] A. Mostafa, I.P. Rubio, V. Brailovski, M. Jahazi, M. Medraj, Structure, texture and phases in 3D printed IN718 alloy subjected to homogenization and HIP treatments, Metals (Basel). 7 (2017) 1–23, https://doi.org/10.3390/met7060196.
[137] N.J. Harrison, I. Todd, K. Mumtaz, Reduction of micro-cracking in nickel superalloys processed by Selective Laser Melting: A fundamental alloy design approach, Acta Mater. 94 (2015) 59–68, https://doi.org/10.1016/j.actamat.2015.04.035.
[138] L. Mataveli Suave, J. Cormier, P. Villechaise, D. Bertheau, G. Benoit, G. Cailletaud, L. Marcin, Anisotropy in creep properties of DS200 + Hf alloy, Mater. High Temp. 33 (2016) 361–371, https://doi.org/10.1080/09603409.2016.1159836.
[139] Ø. Grong, Metallurgical modelling of welding, 1997.
[140] W. Kurz, D.J. Fisher, Fundamental of solidification, CRC Press, 1998.
[141] F. Liu, X. Lin, C. Huang, M. Song, G. Yang, J. Chen, W. Huang, The effect of laser scanning path on microstructures and mechanical properties of laser solid formed nickel-base superalloy Inconel 718, J. Alloys Compd. 509 (2011) 4505–4509, https://doi.org/10.1016/j.jallcom.2010.11.176.
[142] X. Wang, N. Read, L.N. Carter, R.M. Ward, M.M. Attallah, Defect Formation and its Mitigation in Selective Laser Melting of High γ′ Ni-Base Superalloys, in, Superalloys 2016 (2016) 351–358, https://doi.org/10.1002/9781119075646.ch38.
[143] R.C. Reed, The Superalloys as High-Temperature Materials (2006).
[144] X.P. Tan, S. Chandra, Y. Kok, S.B. Tor, G. Seet, N.H. Loh, E. Liu, Revealing competitive columnar grain growth behavior and periodic microstructural banding in additively manufactured Ti-6Al-4 V parts by selective electron beam melting, Materialia. 7 (2019), https://doi.org/10.1016/j.mtla.2019.100365 100365.
[145] P. Kontis, E. Chauvet, Z. Peng, J. He, A.K. da Silva, D. Raabe, C. Tassin, J.J. Blandin, S. Abed, R. Dendievel, B. Gault, G. Martin, Atomic-scale grain boundary engineering to overcome hot-cracking in additively-manufactured superalloys, Acta Mater. 177 (2019) 209–221, https://doi.org/10.1016/j.actamat.2019.07.041.
[146] J.D. Hunt, Steady state columnar and equiaxed growth of dendrites and eutectic, Mater. Sci. Eng. 65 (1984) 75–83, https://doi.org/10.1016/0025-5416(84)90201-5.
[147] Q. Li, X. Lin, X. Wang, H. Yang, W. Huang, Morphology evolution of γ′ phase in K465 nickel-base superalloy during laser forming repairing, J. Laser Appl. 28 (2016), https://doi.org/10.2351/1.4943903 022301.
[148] Z. Zhou, L. Huang, Y. Shang, Y. Li, L. Jiang, Q. Lei, Causes analysis on cracks in nickel-based single crystal superalloy fabricated by laser powder deposition additive manufacturing, Mater. Des. 160 (2018) 1238–1249, https://doi.org/10.1016/j.matdes.2018.10.042.
[149] P. Liu, Z. Wang, Y. Xiao, M.F. Horstemeyer, X. Cui, L. Chen, Insight into the mechanisms of columnar to equiaxed grain transition during metallic additive manufacturing, Addit. Manuf. 26 (2019) 22–29, https://doi.org/10.1016/j.addma.2018.12.019.
[150] J. Shinjo, C. Panwisawas, Digital materials design by thermal-fluid science for multi-metal additive manufacturing, Acta Mater. 210 (2021), https://doi.org/10.1016/j.actamat.2021.116825 116825.
[151] M. Elahinia, N. Shayesteh Moghaddam, M. Taheri Andani, A. Amerinatanzi, B. A. Bimber, R.F. Hamilton, Fabrication of NiTi through additive manufacturing: A review, Prog. Mater. Sci. 83 (2016) 630–663, https://doi.org/10.1016/j.pmatsci.2016.08.001.
[152] I. Polozov, A. Kantyukov, V. Popovich, J.N. Zhu, A. Popovich, Microstructure and mechanical properties of tial-based alloy produced by selective laser melting, Met. 2020 - 29th Int. Conf. Metall. Mater. Conf. Proc. (2020) 1037–1041. 10.37904/metal.2020.3604.
[153] A. Klassen, V.E. Forster, V. Juechter, C. Körner, Numerical simulation of multi-component evaporation during selective electron beam melting of TiAl, J. Mater. Process. Technol. 247 (2017) 280–288, https://doi.org/10.1016/j.jmatprotec.2017.04.016.
[154] T. Mukherjee, J.S. Zuback, T. Debroy, A. De, T. Debroy, Printability of alloys for additive manufacturing, Sci. Rep. 6 (2016) 1–8, https://doi.org/10.1038/srep19717.
[155] C. Panwisawas, Y.T. Tang, J. Ghoussoub, R.C. Reed, Additive Manufacturability of Nickel-Based Superalloys: Composition-Process Induced Vapourization, Springer International Publishing (2020), https://doi.org/10.1007/978-3-030-51834-9_100.
[156] S.H. Kang, Y. Deguchi, K. Yamamoto, K. Ogi, M. Shirai, Solidification process and behavior of alloying elements in Ni-based superalloy inconel718, Mater. Trans. 45 (2004) 2728–2733, https://doi.org/10.2320/matertrans.45.2728.
[157] P.K. Sung, D.R. Poirier, Liquid-solid partition ratios in nickel-base alloys, Metall. Mater. Trans. A Phys. Metall. Mater. Sci. 30 (1999) 2173–2181, https://doi.org/10.1007/s11661-999-0029-5.
[158] A. Ostovari Moghaddam, N.A. Shaburova, M.N. Samodurova, A. Abdollahzadeh, E.A. Trofimov, Additive manufacturing of high entropy alloys: A practical review, J. Mater. Sci. Technol. 77 (2021) 131–162, https://doi.org/10.1016/j.jmst.2020.11.029.
[159] W. Zhang, L. Liu, Solidification microstructure of directionally solidified superalloy under high temperature gradient, Rare Met. 31 (2012) 541–546, https://doi.org/10.1007/s12598-012-0554-z.
[160] F. Zhang, L.E. Levine, A.J. Allen, C.E. Campbell, E.A. Lass, S. Cheruvathur, M.R. Stoudt, M.E. Williams, Y. Idell, Homogenization kinetics of a nickel-based superalloy produced by powder bed fusion laser sintering, Scr. Mater. 131 (2017) 98–102, https://doi.org/10.1016/j.scriptamat.2016.12.037.
[161] G. Luo, M. Cheng, L. Zhao, Y. Tang, J. Yao, H. Cui, L. Song, Preferential interdendritic oxidation of laser additively manufactured Inconel 718, Corros. Sci. 179 (2021), https://doi.org/10.1016/j.corsci.2020.109144 109144.
[162] D. Deng, R.L. Peng, H. Söderberg, J. Moverare, On the formation of microstructural gradients in a nickel-base superalloy during electron beam melting, Mater. Des. 160 (2018) 251–261, https://doi.org/10.1016/j.matdes.2018.09.006.
[163] K. Moussaoui, W. Rubio, M. Mousseigne, T. Sultan, F. Rezai, Effects of Selective Laser Melting additive manufacturing parameters of Inconel 718 on porosity, microstructure and mechanical properties, Mater. Sci. Eng. A. 735 (2018) 182–190, https://doi.org/10.1016/j.msea.2018.08.037.
[164] J.A. Slotwinski, E.J. Garboczi, K.M. Hebenstreit, Porosity measurements and analysis for metal additive manufacturing process control, J. Res. Natl. Inst. Stand. Technol. 119 (2014) 494–528, https://doi.org/10.6028/jres.119.019.
[165] X. Zhao, J. Chen, X. Lin, W. Huang, Study on microstructure and mechanical properties of laser rapid forming Inconel 718, Mater. Sci. Eng. A. 478 (2008) 119–124, https://doi.org/10.1016/j.msea.2007.05.079.
[166] L.L. Parimi, M.M. Attallah, J.C. Gebelin, R.C. Reed, DIRECT LASER FABRICATION OF INCONEL-718 : EFFECTS ON DISTORTION AND MICROSTRUCTURE, (2012) 511–519.
[167] M. Valdez, C. Kozuch, E.J. Faierson, I. Jasiuk, Induced porosity in Super Alloy 718 through the laser additive manufacturing process: Microstructure and mechanical properties, J. Alloys Compd. 725 (2017) 757–764, https://doi.org/10.1016/j.jallcom.2017.07.198.
[168] L.L. Parimi, G. Ravi, D. Clark, M.M. Attallah, Microstructural and texture development in direct laser fabricated IN718, Mater. Charact. 89 (2014) 102–111, https://doi.org/10.1016/j.matchar.2013.12.012.
[169] D.H. Smith, J. Bicknell, L. Jorgensen, B.M. Patterson, N.L. Cordes, I. Tsukrov, M. Knezevic, Microstructure and mechanical behavior of direct metal laser sintered Inconel alloy 718, Mater. Charact. 113 (2016) 1–9, https://doi.org/10.1016/j.matchar.2016.01.003.
[170] W.J. Sames, F. Medina, W.H. Peter, S.S. Babu, R.R. Dehoff, Effect of Process Control and Powder Quality on Inconel 718 Produced Using Electron Beam Melting, in: In: 8th Int. Symp. Superalloy 718 Deriv, John Wiley & Sons Inc, Hoboken, NJ, USA, NJ, USA, 2014, pp. 409–423, https://doi.org/10.1002/9781119016854.ch32.
[171] A. Strondl, M. Palm, J. Gnauk, G. Frommeyer, Microstructure and mechanical properties of nickel based superalloy IN718 produced by rapid prototyping with electron beam melting (EBM), Mater. Sci. Technol. 27 (2011) 876–883, https://doi.org/10.1179/026708309X12468927349451.
[172] W.H. Kan, L.N.S. Chiu, C.V.S. Lim, Y. Zhu, Y. Tian, D. Jiang, A. Huang, A critical review on the effects of process-induced porosity on the mechanical properties of alloys fabricated by laser powder bed fusion, J. Mater. Sci. 57 (2022) 9818–9865, https://doi.org/10.1007/s10853-022-06990-7.
[173] Q. Han, Y. Gu, R. Setchi, F. Lacan, R. Johnston, S.L. Evans, S. Yang, Additive manufacturing of high-strength crack-free Ni-based Hastelloy X superalloy, Addit. Manuf. 30 (2019), https://doi.org/10.1016/j.addma.2019.100919 100919.
[174] K. Wang, D. Du, G. Liu, Z. Pu, B. Chang, J. Ju, A study on the additive manufacturing of a high chromium Nickel-based superalloy by extreme high-speed laser metal deposition, Opt. Laser Technol. 133 (2021), https://doi.org/10.1016/j.optlastec.2020.106504.
[175] S. Holland, X. Wang, J. Chen, W. Cai, F. Yan, L. Li, Multiscale characterization of microstructures and mechanical properties of Inconel 718 fabricated by selective laser melting, J. Alloys Compd. 784 (2019) 182–194, https://doi.org/10.1016/j.jallcom.2018.12.380.
[176] E. Amsterdam, Evaluation of the microstructure and mechanical properties of laser additive manufactured gas turbine alloys Ti-6Al-4V and Natl, Aerosp. Lab. NLR. (2009) 1–25.
[177] N. Nudelis, P. Mayr, A novel classification method for pores in laser powder bed fusion, Metals (Basel). 11 (2021) 1–16, https://doi.org/10.3390/met11121912.
[178] C. Qiu, H. Chen, Q. Liu, S. Yue, H. Wang, On the solidification behaviour and cracking origin of a nickel-based superalloy during selective laser melting, Mater. Charact. 148 (2019) 330–344, https://doi.org/10.1016/j.matchar.2018.12.032.
[179] J. Risse, Additive Manufacturing of Nickel-Base Superalloy IN738LC by Laser Powder Bed Fusion, (2019).
[180] Y. Chen, Y. Guo, M. Xu, C. Ma, Q. Zhang, L. Wang, J. Yao, Z. Li, Study on the element segregation and Laves phase formation in the laser metal deposited IN718 superalloy by flat top laser and gaussian distribution laser, Mater. Sci. Eng. A. 754 (2019) 339–347, https://doi.org/10.1016/j.msea.2019.03.096.
[181] S. Tabaie, F. Rézaï-Aria, M. Jahazi, Microstructure evolution of selective laser melted inconel 718: Influence of high heating rates, Metals (Basel). 10 (2020), https://doi.org/10.3390/met10050587.
[182] E.L. Stevens, J. Toman, A.C. To, M. Chmielus, Variation of hardness, microstructure, and Laves phase distribution in direct laser deposited alloy 718 cuboids, Mater. Des. 119 (2017) 188–198, https://doi.org/10.1016/j.matdes.2017.01.031.
[183] K. Wang, Y. Liu, Z. Sun, J. Lin, Y. Lv, B. Xu, Microstructural evolution and mechanical properties of Inconel 718 superalloy thin wall fabricated by pulsed plasma arc additive manufacturing, J. Alloys Compd. 819 (2020), https://doi.org/10.1016/j.jallcom.2019.152936.

[184] K.C. Xibing Gong, Xiaoqing Wang, Vernon Cole, Zachary Jones, Kenneth Cooper, Characterization of microstructure and mechanical property of Inconel 718 from selective laser melting, ASME Int. Manuf. Sci. Eng. Conf. (2015).
[185] Y. Chen, F. Lu, K. Zhang, P. Nie, S.R. Elmi Hosseini, K. Feng, Z. Li, Dendritic microstructure and hot cracking of laser additive manufactured Inconel 718 under improved base cooling, J. Alloys Compd. 670 (2016) 312–321, https://doi.org/10.1016/j.jallcom.2016.01.250.
[186] H. Xiao, S.M. Li, W.J. Xiao, Y.Q. Li, L.M. Cha, J. Mazumder, L.J. Song, Effects of laser modes on Nb segregation and Laves phase formation during laser additive manufacturing of nickel-based superalloy, Mater. Lett. 188 (2017) 260–262, https://doi.org/10.1016/j.matlet.2016.10.118.
[187] Y. Zhao, K. Li, M. Gargani, W. Xiong, A comparative analysis of Inconel 718 made by additive manufacturing and suction casting: Microstructure evolution in homogenization, Addit. Manuf. 36 (2020), https://doi.org/10.1016/j.addma.2020.101404 101404.
[188] P. Nandwana, M. Kirka, A. Okello, R. Dehoff, Electron beam melting of Inconel 718: effects of processing and post-processing, Mater. Sci. Technol. (United Kingdom) 34 (2018) 612–619, https://doi.org/10.1080/02670836.2018.1424379.
[189] S. Sui, Z. Li, C. Zhong, Q. Zhang, A. Gasser, J. Chen, Y. Chew, G. Bi, Laves phase tuning for enhancing high temperature mechanical property improvement in laser directed energy deposited Inconel 718, Compos. Part B Eng. 215 (2021), https://doi.org/10.1016/j.compositesb.2021.108819 108819.
[190] R. M, S. Koppoju, G. Telasang, R. Korla, P. G, Effect of solutionizing temperature on the microstructural evolution during double aging of powder bed fusion-additive manufactured IN718 alloy, Mater. Charact. 172 (2021) 110868. 10.1016/j.matchar.2020.110868.
[191] S. Chandra, X. Tan, R.L. Narayan, M. Descoins, D. Mangelinck, S.B. Tor, E. Liu, G. Seet, Nanometer-scale precipitations in a selective electron beam melted nickel-based superalloy, Scr. Mater. 194 (2021), https://doi.org/10.1016/j.scriptamat.2020.113661.
[192] M.M. Kirka, K.A. Unocic, N. Raghavan, F. Medina, R.R. Dehoff, S.S. Babu, Microstructure Development in Electron Beam-Melted Inconel 718 and Associated Tensile Properties, Jom. 68 (2016) 1012–1020, https://doi.org/10.1007/s11837-016-1812-6.
[193] V.V. Rielli, F. Godor, C. Gruber, A. Stanojevic, B. Oberwinkler, S. Primig, Effects of processing heterogeneities on the micro- to nanostructure strengthening mechanisms of an alloy 718 turbine disk, Mater. Des. 212 (2021), https://doi.org/10.1016/j.matdes.2021.110295 110295.
[194] S. Sui, J. Chen, R. Zhang, X. Ming, F. Liu, X. Lin, The tensile deformation behavior of laser repaired Inconel 718 with a non-uniform microstructure, Mater. Sci. Eng. A. 688 (2017) 480–487, https://doi.org/10.1016/j.msea.2017.01.110.
[195] A. Segerstark, J. Andersson, L.E. Svensson, O. Ojo, Microstructural characterization of laser metal powder deposited Alloy 718, Mater. Charact. 142 (2018) 550–559, https://doi.org/10.1016/j.matchar.2018.06.020.
[196] H. Yang, J. Yang, W. Huang, Z. Wang, X. Zeng, The printability, microstructure, crystallographic features and microhardness of selective laser melted Inconel 718 thin wall, Mater. Des. 156 (2018) 407–418, https://doi.org/10.1016/j.matdes.2018.07.007.
[197] J. Jang, D. Van, S.H. Lee, Precipitation kinetics of secondary phases induced by heat accumulation in the deposit of Inconel 718, Addit. Manuf. 55 (2022), https://doi.org/10.1016/j.addma.2022.102831 102831.
[198] S.H. Sun, Y. Koizumi, T. Saito, K. Yamanaka, Y.P. Li, Y. Cui, A. Chiba, Electron beam additive manufacturing of Inconel 718 alloy rods: Impact of build direction on microstructure and high-temperature tensile properties, Addit. Manuf. 23 (2018) 457–470, https://doi.org/10.1016/j.addma.2018.08.017.
[199] C. Kumara, A. Segerstark, F. Hanning, N. Dixit, S. Joshi, J. Moverare, P. Nylén, Microstructure modelling of laser metal powder directed energy deposition of alloy 718, Addit. Manuf. 25 (2019) 357–364, https://doi.org/10.1016/j.addma.2018.11.024.
[200] A. Segerstark, J. Andersson, L.E. Svensson, Evaluation of a temperature measurement method developed for laser metal deposition, Sci. Technol. Weld. Join. 22 (2017) 1–6, https://doi.org/10.1080/13621718.2016.1169363.
[201] C. Kumara, D. Deng, F. Hanning, M. Raanes, J. Moverare, P. Nylén, Predicting the Microstructural Evolution of Electron Beam Melting of Alloy 718 with Phase-Field Modeling, Metall. Mater. Trans. A Phys. Metall. Mater. Sci. 50 (2019) 2527–2537, https://doi.org/10.1007/s11661-019-05163-7.
[202] Z. Yan, W. Liu, Z. Tang, X. Liu, N. Zhang, M. Li, H. Zhang, Review on thermal analysis in laser-based additive manufacturing, Opt. Laser Technol. 106 (2018) 427–441, https://doi.org/10.1016/j.optlastec.2018.04.034.
[203] C. Zhang, L. Li, A. Deceuster, Thermomechanical analysis of multi-bead pulsed laser powder deposition of a nickel-based superalloy, J. Mater. Process. Technol. 211 (2011) 1478–1487, https://doi.org/10.1016/j.jmatprotec.2011.03.023.
[204] E.R. Denlinger, J.C. Heigel, P. Michaleris, T.A. Palmer, Effect of inter-layer dwell time on distortion and residual stress in additive manufacturing of titanium and nickel alloys, J. Mater. Process. Technol. 215 (2015) 123–131, https://doi.org/10.1016/j.jmatprotec.2014.07.030.
[205] K. Zhang, X. Shang, W. Liu, Realtime measurement of temperature field during direct laser deposition shaping, Adv. Mater. Res. 143–144 (2011) 521–526, https://doi.org/10.4028/www.scientific.net/AMR.143-144.521.
[206] B. Ahmad, S.O. van der Veen, M.E. Fitzpatrick, H. Guo, Residual stress evaluation in selective-laser-melting additively manufactured titanium (Ti-6Al-4V) and inconel 718 using the contour method and numerical simulation, Addit. Manuf. 22 (2018) 571–582, https://doi.org/10.1016/j.addma.2018.06.002.
[207] B. Lane, E. Whitenton, S. Moylan, Multiple sensor detection of process phenomena in laser powder bed fusion, in: J.N. Zalameda, P. Bison (Eds.), 2016: p. 986104. 10.1117/12.2224390.
[208] E. Kundakcioglu, I. Lazoglu, S. Rawal, Transient thermal modeling of laser-based additive manufacturing for 3D freeform structures, Int. J. Adv. Manuf. Technol. 85 (2016) 493–501, https://doi.org/10.1007/s00170-015-7932-2.
[209] M. Chiumenti, M. Cervera, A. Salmi, C. Agelet de Saracibar, N. Dialami, K. Matsui, Finite element modeling of multi-pass welding and shaped metal deposition processes, Comput. Methods Appl. Mech. Eng. 199 (2010) 2343–2359, https://doi.org/10.1016/j.cma.2010.02.018.
[210] P. Promoppatum, S.C. Yao, P.C. Pistorius, A.D. Rollett, P.J. Coutts, F. Lia, R. Martukanitz, Numerical modeling and experimental validation of thermal history and microstructure for additive manufacturing of an Inconel 718 product, Prog. Addit. Manuf. 3 (2018) 15–32, https://doi.org/10.1007/s40964-018-0039-1.
[211] K.T. Makiewicz, Development of simultaneous transformation kinetics microstructure model with application to laser metal deposited Ti-6Al-4V and alloy 718, Thesis, Ohio State Univ. (2013) 259.
[212] W.M. Tucho, P. Cuvillier, A. Sjolyst-Kverneland, V. Hansen, Microstructure and hardness studies of Inconel 718 manufactured by selective laser melting before and after solution heat treatment, Mater. Sci. Eng. A. 689 (2017) 220–232, https://doi.org/10.1016/j.msea.2017.02.062.
[213] J.P. Choi, G.H. Shin, S. Yang, D.Y. Yang, J.S. Lee, M. Brochu, J.H. Yu, Densification and microstructural investigation of Inconel 718 parts fabricated by selective laser melting, Powder Technol. 310 (2017) 60–66, https://doi.org/10.1016/j.powtec.2017.01.030.
[214] Z. Wang, K. Guan, M. Gao, X. Li, X. Chen, X. Zeng, The microstructure and mechanical properties of deposited-IN718 by selective laser melting, J. Alloys Compd. 513 (2012) 518–523, https://doi.org/10.1016/j.jallcom.2011.10.107.
[215] D. Tomus, Y. Tian, P.A. Rometsch, M. Heilmaier, X. Wu, Influence of post heat treatments on anisotropy of mechanical behaviour and microstructure of Hastelloy-X parts produced by selective laser melting, Mater. Sci. Eng. A. 667 (2016) 42–53, https://doi.org/10.1016/j.msea.2016.04.086.
[216] M.L. Montero-Sistiaga, S. Pourbabak, J. Van Humbeeck, D. Schryvers, K. Vanmeensel, Microstructure and mechanical properties of Hastelloy X produced by HP-SLM (high power selective laser melting), Mater. Des. 165 (2019), https://doi.org/10.1016/j.matdes.2019.107598 107598.
[217] I.T. Ho, T.H. Hsu, Y.J. Chang, C.W. Li, K.C. Chang, S. Tin, K. Kakehi, A.C. Yeh, Effects of CoAl2O4 inoculants on microstructure and mechanical properties of IN718 processed by selective laser melting, Addit. Manuf. 35 (2020), https://doi.org/10.1016/j.addma.2020.101328 101328.
[218] C.L. Frederick, A. Plotkowski, M.M. Kirka, M. Haines, A. Staub, E.J. Schwalbach, D. Cullen, S.S. Babu, Geometry-Induced Spatial Variation of Microstructure Evolution During Selective Electron Beam Melting of Rene-N5, Metall. Mater. Trans. A Phys. Metall. Mater. Sci. 49 (2018) 5080–5096, https://doi.org/10.1007/s11661-018-4793-y.
[219] A. Lavakumar, P. Singh, S. Srivastava, Gamma Prime Coarsening Behavior of Nickel Superalloy Super cast 247A after Prolonged Thermal Exposures, Second Natl, Conf. Recent Dev. Mech. Eng. 4 (2013) 37–42.
[220] J.R. Vaunois, J. Cormier, P. Villechaise, A. Devaux, B. Flageolet, Influence of both γ′ distribution and grain size on the tensile properties of UDIMET 720Li at room temperature, 7th Int. Symp. Superalloy 718 Deriv. 2010. 1 (2010) 199–213. 10.1002/9781118495223.ch14.
[221] D. Kong, C. Dong, X. Ni, L. Zhang, C. Man, J. Yao, Y. Ji, Y. Ying, K. Xiao, X. Cheng, X. Li, High-throughput fabrication of nickel-based alloys with different Nb contents via a dual-feed additive manufacturing system: Effect of Nb content on microstructural and mechanical properties, J. Alloys Compd. 785 (2019) 826–837, https://doi.org/10.1016/j.jallcom.2019.01.263.
[222] M. Munther, T. Palma, F. Tavangarian, A. Beheshti, K. Davami, Nanomechanical properties of additively and traditionally manufactured nickel-chromium-based superalloys through instrumented nanoindentation, Manuf. Lett. 23 (2020) 39–43, https://doi.org/10.1016/j.mfglet.2019.09.003.
[223] Q. Jia, D. Gu, Selective laser melting additive manufacturing of Inconel 718 superalloy parts: Densification, microstructure and properties, J. Alloys Compd. 585 (2014) 713–721, https://doi.org/10.1016/j.jallcom.2013.09.171.
[224] T. Rong, D. Gu, Formation of novel graded interface and its function on mechanical properties of WC1-x reinforced Inconel 718 composites processed by selective laser melting, J. Alloys Compd. 680 (2016) 333–342, https://doi.org/10.1016/j.jallcom.2016.04.107.
[225] D. Gu, Q. Shi, K. Lin, L. Xi, Microstructure and performance evolution and underlying thermal mechanisms of Ni-based parts fabricated by selective laser melting, Addit. Manuf. 22 (2018) 265–278, https://doi.org/10.1016/j.addma.2018.05.019.
[226] D. Deng, R.L. Peng, H. Brodin, J. Moverare, Microstructure and mechanical properties of Inconel 718 produced by selective laser melting: Sample orientation dependence and effects of post heat treatments, Mater. Sci. Eng. A. 713 (2018) 294–306, https://doi.org/10.1016/j.msea.2017.12.043.
[227] Y.T. Tang, C. Panwisawas, J.N. Ghoussoub, Y. Gong, J.W.G. Clark, A.A.N. Németh, D.G. McCartney, R.C. Reed, Alloys-by-design: Application to new superalloys for additive manufacturing, Acta Mater. 202 (2021) 417–436, https://doi.org/10.1016/j.actamat.2020.09.023.
[228] G. Marchese, X. Garmendia Colera, F. Calignano, M. Lorusso, S. Biamino, P. Minetola, D. Manfredi, Characterization and Comparison of Inconel 625

Processed by Selective Laser Melting and Laser Metal Deposition, Adv. Eng. Mater. 19 (2017) 1–9, https://doi.org/10.1002/adem.201600635.
[229] T. Rong, D. Gu, Q. Shi, S. Cao, M. Xia, Effects of tailored gradient interface on wear properties of WC/Inconel 718 composites using selective laser melting, Surf. Coatings Technol. 307 (2016) 418–427, https://doi.org/10.1016/j.surfcoat.2016.09.011.
[230] P. Karimi, E. Sadeghi, D. Deng, H. Gruber, J. Andersson, P. Nylén, Influence of build layout and orientation on microstructural characteristics of electron beam melted Alloy 718, Int. J. Adv. Manuf. Technol. 99 (2018) 2903–2913, https://doi.org/10.1007/s00170-018-2621-6.
[231] R. Ghiaasiaan, M. Muhammad, P.R. Gradl, S. Shao, N. Shamsaei, Superior tensile properties of Hastelloy X enabled by additive manufacturing, Mater. Res. Lett. 9 (2021) 308–314, https://doi.org/10.1080/21663831.2021.1911870.
[232] A. Kreitcberg, V. Brailovski, S. Turenne, Elevated temperature mechanical behavior of IN625 alloy processed by laser powder-bed fusion, Mater. Sci. Eng. A. 700 (2017) 540–553, https://doi.org/10.1016/j.msea.2017.06.045.
[233] S. Sun, Q. Teng, Y. Xie, T. Liu, R. Ma, J. Bai, C. Cai, Q. Wei, Two-step heat treatment for laser powder bed fusion of a nickel-based superalloy with simultaneously enhanced tensile strength and ductility, Addit. Manuf. 46 (2021), https://doi.org/10.1016/j.addma.2021.102168 102168.
[234] L.E. Murr, E. Martinez, S.M. Gaytan, D.A. Ramirez, B.I. MacHado, P.W. Shindo, J.L. Martinez, F. Medina, J. Wooten, D. Ciscel, U. Ackelid, R.B. Wicker, Microstructural architecture, microstructures, and mechanical properties for a nickel-base superalloy fabricated by electron beam melting, Metall. Mater. Trans. A Phys. Metall. Mater. Sci. 42 (2011) 3491–3508, https://doi.org/10.1007/s11661-011-0748-2.
[235] V.A. Popovich, E.V. Borisov, A.A. Popovich, V.S. Sufiiarov, D.V. Masaylo, L. Alzina, Impact of heat treatment on mechanical behaviour of Inconel 718 processed with tailored microstructure by selective laser melting, Mater. Des. 131 (2017) 12–22, https://doi.org/10.1016/j.matdes.2017.05.065.
[236] F. Wang, Mechanical property study on rapid additive layer manufacture Hastelloy® X alloy by selective laser melting technology, Int. J. Adv. Manuf. Technol. 58 (2012) 545–551, https://doi.org/10.1007/s00170-011-3423-2.
[237] A. Kreitcberg, V. Brailovski, S. Turenne, Effect of heat treatment and hot isostatic pressing on the microstructure and mechanical properties of Inconel 625 alloy processed by laser powder bed fusion, Mater. Sci. Eng. A. 689 (2017) 1–10, https://doi.org/10.1016/j.msea.2017.02.038.
[238] L. Rickenbacher, T. Etter, S. Hövel, K. Wegener, High temperature material properties of IN738LC processed by selective laser melting (SLM) technology, Rapid Prototyp. J. 19 (2013) 282–290, https://doi.org/10.1108/13552541311323281.
[239] D. Deng, Additively Manufactured Inconel 718: Microstructures and Mechanical Properties, Linköping University Electronic Press, Linköping (2018), https://doi.org/10.3384/lic.diva-144491.
[240] D. Zhang, W. Niu, X. Cao, Z. Liu, Effect of standard heat treatment on the microstructure and mechanical properties of selective laser melting manufactured Inconel 718 superalloy, Mater. Sci. Eng. A. 644 (2015) 32–40, https://doi.org/10.1016/j.msea.2015.06.021.
[241] W. Zhou, Y. Tian, Q. Tan, S. Qiao, H. Luo, G. Zhu, D. Shu, Effect of carbon content on the microstructure, tensile properties and cracking susceptibility of IN738 superalloy processed by laser powder bed fusion, Addit. Manuf. 58 (2022), https://doi.org/10.1016/j.addma.2022.103016 103016.
[242] G. Marchese, M. Lorusso, S. Parizia, E. Bassini, J.W. Lee, F. Calignano, D. Manfredi, M. Terner, H.U. Hong, D. Ugues, M. Lombardi, S. Biamino, Influence of heat treatments on microstructure evolution and mechanical properties of Inconel 625 processed by laser powder bed fusion, Mater. Sci. Eng. A. 729 (2018) 64–75, https://doi.org/10.1016/j.msea.2018.05.044.
[243] X. Yao, S.K. Moon, B.Y. Lee, G. Bi, Effects of heat treatment on microstructures and tensile properties of IN718/TiC nanocomposite fabricated by selective laser melting, Int. J. Precis. Eng. Manuf. 18 (2017) 1693–1701, https://doi.org/10.1007/s12541-017-0197-y.
[244] Y.Y. Wang, J. Shi, S. Lu, Y.Y. Wang, Selective Laser Melting of Graphene-Reinforced Inconel 718 Superalloy: Evaluation of Microstructure and Tensile Performance, J. Manuf. Sci. Eng. Trans. ASME. 139 (2017) 1–6, https://doi.org/10.1115/1.4034712.
[245] P. Wang, B. Zhang, C.C. Tan, S. Raghavan, Y.F. Lim, C.N. Sun, J. Wei, D. Chi, Microstructural characteristics and mechanical properties of carbon nanotube reinforced Inconel 625 parts fabricated by selective laser melting, Mater. Des. 112 (2016) 290–299, https://doi.org/10.1016/j.matdes.2016.09.080.
[246] J. Strößner, M. Terock, U. Glatzel, Mechanical and Microstructural Investigation of Nickel-Based Superalloy IN718 Manufactured by Selective Laser Melting (SLM), Adv. Eng. Mater. 17 (2015) 1099–1105, https://doi.org/10.1002/adem.201500158.
[247] M. Ni, C. Chen, X. Wang, P. Wang, R. Li, X. Zhang, K. Zhou, Anisotropic tensile behavior of in situ precipitation strengthened Inconel 718 fabricated by additive manufacturing, Mater. Sci. Eng. A. 701 (2017) 344–351, https://doi.org/10.1016/j.msea.2017.06.098.
[248] Z. Chen, S. Chen, Z. Wei, L. Zhang, P. Wei, B. Lu, S. Zhang, Y. Xiang, Anisotropy of nickel-based superalloy K418 fabricated by selective laser melting, Prog. Nat. Sci. Mater. Int. 28 (2018) 496–504, https://doi.org/10.1016/j.pnsc.2018.07.001.
[249] M.M. Kirka, D.A. Greeley, C. Hawkins, R.R. Dehoff, Effect of anisotropy and texture on the low cycle fatigue behavior of Inconel 718 processed via electron beam melting, Int. J. Fatigue. 105 (2017) 235–243, https://doi.org/10.1016/j.ijfatigue.2017.08.021.
[250] C. Qiu, N.J.E. Adkins, M.M. Attallah, Selective laser melting of Invar 36: Microstructure and properties, Acta Mater. 103 (2016) 382–395, https://doi.org/10.1016/j.actamat.2015.10.020.
[251] C.H. Yu, R.L. Peng, V. Luzin, M. Sprengel, M. Calmunger, J.E. Lundgren, H. Brodin, A. Kromm, J. Moverare, Thin-wall effects and anisotropic deformation mechanisms of an additively manufactured Ni-based superalloy, Addit. Manuf. 36 (2020), https://doi.org/10.1016/j.addma.2020.101672 101672.
[252] D. Tomus, P.A. Rometsch, M. Heilmaier, X. Wu, Effect of minor alloying elements on crack-formation characteristics of Hastelloy-X manufactured by selective laser melting, Addit. Manuf. 16 (2017) 65–72, https://doi.org/10.1016/j.addma.2017.05.006.
[253] M. Cloots, K. Kunze, P.J. Uggowitzer, K. Wegener, Microstructural characteristics of the nickel-based alloy IN738LC and the cobalt-based alloy Mar-M509 produced by selective laser melting, Mater. Sci. Eng. A. 658 (2016) 68–76, https://doi.org/10.1016/j.msea.2016.01.058.
[254] F. Caiazzo, V. Alfieri, G. Corrado, P. Argenio, Mechanical properties of Inconel 718 in additive manufacturing via selective laser melting: An investigation on possible anisotropy of tensile strength, RTSI 2017 - IEEE 3rd Int. Forum Res. Technol. Soc. Ind. Conf. Proc. (2017) 20–23. 10.1109/RTSI.2017.8065941.
[255] E. Chlebus, K. Gruber, B. Kuźnicka, J. Kurzac, T. Kurzynowski, Effect of heat treatment on the microstructure and mechanical properties of Inconel 718 processed by selective laser melting, Mater. Sci. Eng. A. 639 (2015) 647–655, https://doi.org/10.1016/j.msea.2015.05.035.
[256] C. Kumara, D. Deng, J. Moverare, P. Nylén, Modelling of anisotropic elastic properties in alloy 718 built by electron beam melting, Mater. Sci. Technol. (United Kingdom) 34 (2018) 529–537, https://doi.org/10.1080/02670836.2018.1426258.
[257] K. Kunze, T. Etter, J. Grässlin, V. Shklover, Texture, anisotropy in microstructure and mechanical properties of IN738LC alloy processed by selective laser melting (SLM), Mater. Sci. Eng. A. 620 (2015) 213–222, https://doi.org/10.1016/j.msea.2014.10.003.
[258] W.A. Tayon, R.N. Shenoy, M.R. Redding, R. Keith Bird, R.A. Hafley, Correlation between microstructure and mechanical properties in an inconel 718 deposit produced via electron beam freeform fabrication, J. Manuf. Sci. Eng. Trans. ASME. 136 (2014) 1–7, https://doi.org/10.1115/1.4028509.
[259] C. Körner, H. Helmer, A. Bauereiß, R.F. Singer, Tailoring the grain structure of IN718 during selective electron beam melting, MATEC Web Conf. 14 (2014), https://doi.org/10.1051/matecconf/20141408001.
[260] Y.L. Kuo, S. Horikawa, K. Kakehi, Effects of build direction and heat treatment on creep properties of Ni-base superalloy built up by additive manufacturing, Scr. Mater. 129 (2017) 74–78, https://doi.org/10.1016/j.scriptamat.2016.10.035.
[261] S. Sanchez, C.J. Hyde, I.A. Ashcroft, R. G.A., A.T. Clare, Multi-laser scan strategies for enhancing creep performance in LPBF, Addit. Manuf. 41 (2021). 10.1016/j.addma.2021.101948.
[262] M. Pröbstle, S. Neumeier, J. Hopfenmüller, L.P. Freund, T. Niendorf, D. Schwarze, M. Göken, Superior creep strength of a nickel-based superalloy produced by selective laser melting, Mater. Sci. Eng. A. 674 (2016) 299–307, https://doi.org/10.1016/j.msea.2016.07.061.
[263] J.N. Ghoussoub, Y.T. Tang, W.J.B. Dick-Cleland, A.A.N. Németh, Y. Gong, D.G. McCartney, A.C.F. Cocks, R.C. Reed, On the Influence of Alloy Composition on the Additive Manufacturability of Ni-Based Superalloys, Metall. Mater. Trans. A Phys. Metall. Mater. Sci. 53 (2022) 962–983, https://doi.org/10.1007/s11661-021-06568-z.
[264] M.V. Nathal, Effect of initial gamma prime size on the elevated temperature creep properties of single crystal nickel base superalloys, Metall. Trans. A. 18 (1987) 1961–1970, https://doi.org/10.1007/bf02647026.
[265] P. Caron, Y. Ohta, Y.G. Nakagawa, T. Khan, Creep Deformation Anisotropy in Single Crystal Superalloys (1988) 215–224, https://doi.org/10.7449/1988/superalloys_1988_215_224.
[266] P. Caron, High γ′ Solvus New Generation Nickel-Based Superalloys for Single Crystal Turbine Blade Applications 5 (2000) 737–746, https://doi.org/10.7449/2000/superalloys_2000_737_746.
[267] C. Hautfenne, E. De Bruycker, S. Nardone, Influence of heat treatments and build orientation on the creep strength of additive manufactured IN718 Contact data, Influ, Heat Treat. Build Orientat. Creep Strength Ofadditive Manuf. IN 718 (2017) 1–8.
[268] H. Brodin, O. Andersson, S. Johansson, Mechanical testing of a selective laser melted superalloy, 13th Int. Conf. Fract. 2013, ICF 2013. 3 (2013) 2573–2583.
[269] W. Ren, C. Niu, B. Ding, Y. Zhong, J. Yu, Z. Ren, W. Liu, L. Ren, P.K. Liaw, Improvement in creep life of a nickel-based single-crystal superalloy via composition homogeneity on the multiscales by magnetic-field-assisted directional solidification, Sci. Rep. 8 (2018) 1–17, https://doi.org/10.1038/s41598-018-19800-5.
[270] M.M. Kirka, P. Fernandez-Zelaia, Y. Lee, P. Nandwana, S. Yoder, O. Acevedo, D. Ryan, Mechanical Performance of a Non-weldable Ni-Base Superalloy: Inconel 738 Fabricated by Electron Beam Melting, in (2020) 1075–1084, https://doi.org/10.1007/978-3-030-51834-9_105.
[271] B. Shassere, D. Greeley, A. Okello, M. Kirka, P. Nandwana, R. Dehoff, Correlation of Microstructure to Creep Response of Hot Isostatically Pressed and Aged Electron Beam Melted Inconel 718, Metall. Mater. Trans. A Phys. Metall. Mater. Sci. 49 (2018) 5107–5117, https://doi.org/10.1007/s11661-018-4812-z.

[272] M.E. Aydinöz, F. Brenne, M. Schaper, C. Schaak, W. Tillmann, J. Nellesen, T. Niendorf, On the microstructural and mechanical properties of post-treated additively manufactured Inconel 718 superalloy under quasi-static and cyclic loading, Mater. Sci. Eng. A. 669 (2016) 246–258, https://doi.org/10.1016/j.msea.2016.05.089.
[273] A.S. Johnson, S. Shao, N. Shamsaei, S.M. Thompson, L. Bian, Microstructure, Fatigue Behavior, and Failure Mechanisms of Direct Laser-Deposited Inconel 718, Jom. 69 (2017) 597–603, https://doi.org/10.1007/s11837-016-2225-2.
[274] A. Carter, A. Saigal, P.F. Kelley, Fatigue behaviour of direct metal laser sintered Inconel 718, Int. J. Precis. Technol. 6 (2016) 277, https://doi.org/10.1504/ijptech.2016.10000853.
[275] D.B. Witkin, D.N. Patel, G.E. Bean, Notched fatigue testing of Inconel 718 prepared by selective laser melting, Fatigue Fract. Eng. Mater. Struct. 42 (2019) 166–177, https://doi.org/10.1111/ffe.12880.
[276] R. Konečná, G. Nicoletto, L. Kunz, A. Bača, Microstructure and directional fatigue behavior of Inconel 718 produced by selective laser melting, Procedia Struct. Integr. 2 (2016) 2381–2388, https://doi.org/10.1016/j.prostr.2016.06.298.
[277] V.A. Popovich, E. V. Borisov, V. Heurtebise, T. Riemslag, A.A. Popovich, V.S. Sufiiarov, Creep and Thermomechanical Fatigue of Functionally Graded Inconel 718 Produced by Additive Manufacturing, in: 2018: pp. 85–97. 10.1007/978-3-319-72526-0_9.
[278] T. Brynk, Z. Pakiela, K. Ludwichowska, B. Romelczyk, R.M. Molak, M. Plocinska, J. Kurzac, T. Kurzynowski, E. Chlebus, Fatigue crack growth rate and tensile strength of Re modified Inconel 718 produced by means of selective laser melting, Mater. Sci. Eng. A. 698 (2017) 289–301, https://doi.org/10.1016/j.msea.2017.05.052.
[279] S. Gribbin, J. Bicknell, L. Jorgensen, I. Tsukrov, M. Knezevic, Low cycle fatigue behavior of direct metal laser sintered Inconel alloy 718, Int. J. Fatigue. 93 (2016) 156–167, https://doi.org/10.1016/j.ijfatigue.2016.08.019.
[280] J.R. Poulin, V. Brailovski, P. Terriault, Long fatigue crack propagation behavior of Inconel 625 processed by laser powder bed fusion: Influence of build orientation and post-processing conditions, Int. J. Fatigue. 116 (2018) 634–647, https://doi.org/10.1016/j.ijfatigue.2018.07.008.
[281] Z. Zhou, X. Hua, C. Li, G. Chen, The effect of texture on the low cycle fatigue property of Inconel 718 by selective laser melting, MATEC Web Conf. 165 (2018), https://doi.org/10.1051/matecconf/201816502007.
[282] P. Mercelis, J.P. Kruth, Residual stresses in selective laser sintering and selective laser melting, Rapid Prototyp. J. 12 (2006) 254–265, https://doi.org/10.1108/13552540610707013.
[283] F. Liu, X. Lin, G. Yang, M. Song, J. Chen, W. Huang, Microstructure and residual stress of laser rapid formed Inconel 718 nickel-base superalloy, Opt. Laser Technol. 43 (2011) 208–213, https://doi.org/10.1016/j.optlastec.2010.06.015.
[284] T. Mishurova, S. Cabeza, T. Thiede, N. Nadammal, A. Kromm, M. Klaus, C. Genzel, C. Haberland, G. Bruno, The Influence of the Support Structure on Residual Stress and Distortion in SLM Inconel 718 Parts, Metall. Mater. Trans. A Phys. Metall. Mater. Sci. 49 (2018) 3038–3046, https://doi.org/10.1007/s11661-018-4653-9.
[285] T. Thiede, S. Cabeza, T. Mishurova, N. Nadammal, A. Kromm, J. Bode, C. Haberland, G. Bruno, Residual Stress in Selective Laser Melted Inconel 718: Influence of the Removal from Base Plate and Deposition Hatch Length, Mater. Perform. Charact. 7 (2018) 20170119, https://doi.org/10.1520/MPC20170119.
[286] Y. Liu, Y. Yang, D. Wang, A study on the residual stress during selective laser melting (SLM) of metallic powder, Int. J. Adv. Manuf. Technol. 87 (2016) 647–656, https://doi.org/10.1007/s00170-016-8466-y.
[287] N. Nadammal, T. Mishurova, T. Fritsch, I. Serrano-Munoz, A. Kromm, C. Haberland, P.D. Portella, G. Bruno, Critical role of scan strategies on the development of microstructure, texture, and residual stresses during laser powder bed fusion additive manufacturing, Addit. Manuf. 38 (2021), https://doi.org/10.1016/j.addma.2020.101792 101792.
[288] N. Nadammal, S. Cabeza, T. Mishurova, T. Thiede, A. Kromm, C. Seyfert, L. Farahbod, C. Haberland, J.A. Schneider, P.D. Portella, G. Bruno, Effect of hatch length on the development of microstructure, texture and residual stresses in selective laser melted superalloy Inconel 718, Mater. Des. 134 (2017) 139–150, https://doi.org/10.1016/j.matdes.2017.08.049.
[289] Y.S. Lee, M.M. Kirka, S. Kim, N. Sridharan, A. Okello, R.R. Dehoff, S.S. Babu, Asymmetric cracking in Mar-M247 alloy builds during electron beam powder bed fusion additive manufacturing, Met. Mater. Trans. A Phys. Met. Mater. Sci. 49 (2018) 5065–5079.
[290] B. Dutta, S. Babu, B.H. Jared, Science, Technology and Applications of Metals in Additive Manufacturing, Elsevier (2009).
[291] Q. Wu, T. Mukherjee, C. Liu, J. Lu, T. DebRoy, Residual stresses and distortion in the patterned printing of titanium and nickel alloys, Addit. Manuf. 29 (2019), https://doi.org/10.1016/j.addma.2019.100808 100808.
[292] S. Cabeza, B. Özcan, J. Cormier, T. Pirling, S. Polenz, F. Marquardt, T.C. Hansen, E. López, A. Vilalta-Clemente, C. Leyens, Strain Monitoring During Laser Metal Deposition of Inconel 718 by Neutron Diffraction, in (2020) 1033–1045, https://doi.org/10.1007/978-3-030-51834-9_101.
[293] S.J. Foster, K. Carver, R.B. Dinwiddie, F. List, K.A. Unocic, A. Chaudhary, S.S. Babu, Process-Defect-Structure-Property Correlations During Laser Powder Bed Fusion of Alloy 718: Role of In Situ and Ex Situ Characterizations, Metall. Mater. Trans. A Phys. Metall. Mater. Sci. 49 (2018) 5775–5798, https://doi.org/10.1007/s11661-018-4870-2.
[294] G. Wang, H. Ouyang, C. Fan, Q. Guo, Z. Li, W. Yan, Z. Li, The origin of high-density dislocations in additively manufactured metals, Mater. Res. Lett. 8 (2020) 283–290, https://doi.org/10.1080/21663831.2020.1751739.
[295] J. Cao, F. Liu, X. Lin, C. Huang, J. Chen, W. Huang, Effect of overlap rate on recrystallization behaviors of Laser Solid Formed Inconel 718 superalloy, Opt. Laser Technol. 45 (2013) 228–235, https://doi.org/10.1016/j.optlastec.2012.06.043.
[296] Y.T. Tang, J.N. Ghoussoub, C. Panwisawas, D.M. Collins, S. Amirkhanlou, J.W.G. Clark, A.A.N. Németh, D. Graham McCartney, R.C. Reed, The Effect of Heat Treatment on Tensile Yielding Response of the New Superalloy ABD-900AM for Additive Manufacturing, in: 2020: pp. 1055–1065. 10.1007/978-3-030-51834-9_103.
[297] E.A. Lass, M.R. Stoudt, M.E. Williams, M.B. Katz, L.E. Levine, T.Q. Phan, T.H. Gnaeupel-Herold, D.S. Ng, Formation of the Ni3Nb δ-Phase in Stress-Relieved Inconel 625 Produced via Laser Powder-Bed Fusion Additive Manufacturing, Metall. Mater. Trans. A Phys. Metall. Mater. Sci. 48 (2017) 5547–5558, https://doi.org/10.1007/s11661-017-4304-6.
[298] M.R. Stoudt, E.A. Lass, D.S. Ng, M.E. Williams, F. Zhang, C.E. Campbell, G. Lindwall, L.E. Levine, The Influence of Annealing Temperature and Time on the Formation of δ-Phase in Additively-Manufactured Inconel 625, Metall. Mater. Trans. A Phys. Metall. Mater. Sci. 49 (2018) 3028–3037, https://doi.org/10.1007/s11661-018-4643-y.
[299] S.L. Semiatin, P.N. Fagin, R.L. Goetz, D.U. Furrer, R.E. Dutton, Characterization of Plastic Flow Pertinent to the Evolution of Bulk Residual Stress in Powder-Metallurgy, Nickel-Base Superalloys, Metall. Mater. Trans. A Phys. Metall. Mater. Sci. 46 (2015) 3943–3959, https://doi.org/10.1007/s11661-015-3033-y.
[300] J.F. Radavich, A. Fort, Effects of Long-Time Exposure in Alloy 625 at 12OO F, 1400 F and 1600 F, (2012) 635–647. 10.7449/1994/superalloys_1994_635_647.
[301] N. D'Souza, W. Li, C. Argyrakis, G.D. West, C.D. Slater, On the Evolution of Primary Gamma Prime Precipitates During High Temperature and High Strain Rate Deformation and Subsequent Heat Treatment in the Ni-Based Superalloy, RR1000, Metall. Mater. Trans. A Phys. Metall. Mater. Sci. 50 (2019) 4205–4222, https://doi.org/10.1007/s11661-019-05330-w.
[302] S.L. Semiatin, J.M. Shank, A.R. Shiveley, W.M. Saurber, E.F. Gaussa, A.L. Pilchak, The Effect of Forging Variables on the Supersolvus Heat-Treatment Response of Powder-Metallurgy Nickel-Base Superalloys, Metall. Mater. Trans. A Phys. Metall. Mater. Sci. 45 (2014) 6231–6251, https://doi.org/10.1007/s11661-014-2572-y.
[303] Y. Zhao, H. Zhang, H. Wei, Q. Zheng, T. Jin, X. Sun, Progress of phase-field investigations of γ′ rafting in nickel-base single-crystal superalloys, Chinese Sci. Bull. 59 (2014) 1684–1695, https://doi.org/10.1007/s11434-014-0228-3.
[304] Z. Yu, X. Wang, F. Yang, Z. Yue, J.C.M. Li, Review of γ' rafting behavior in nickel-based superalloys: Crystal plasticity and phase-field simulation, Crystals. 10 (2020) 1–24, https://doi.org/10.3390/cryst10121095.
[305] C.C. Engler-Pinto, Jr, C. Noseda, M.Y. Nazmy, F. Rezai-Aria, Interaction Between Creep and Thermo-Mechanical Fatigue of CM247LC-DS, (2012) 319–325. 10.7449/1996/superalloys_1996_319_325.
[306] S.E. Atabay, O. Sanchez-Mata, J.A. Muñiz-Lerma, R. Gauvin, M. Brochu, Microstructure and mechanical properties of rene 41 alloy manufactured by laser powder bed fusion, Mater. Sci. Eng. A. 773 (2020), https://doi.org/10.1016/j.msea.2019.138849 138849.
[307] A.S. Shaikh, F. Schulz, K. Minet-Lallemand, E. Hryha, Microstructure and mechanical properties of Haynes 282 superalloy produced by laser powder bed fusion, Mater. Today Commun. 26 (2021), https://doi.org/10.1016/j.mtcomm.2021.102038.
[308] Q. Jia, D. Gu, Selective laser melting additive manufactured Inconel 718 superalloy parts: High-temperature oxidation property and its mechanisms, Opt. Laser Technol. 62 (2014) 161–171, https://doi.org/10.1016/j.optlastec.2014.03.008.
[309] E. Chauvet, C. Tassin, J.J. Blandin, R. Dendievel, G. Martin, Producing Ni-base superalloys single crystal by selective electron beam melting, Scr. Mater. 152 (2018) 15–19, https://doi.org/10.1016/j.scriptamat.2018.03.041.
[310] N. Raghavan, S. Simunovic, R. Dehoff, A. Plotkowski, J. Turner, M. Kirka, S. Babu, Localized melt-scan strategy for site specific control of grain size and primary dendrite arm spacing in electron beam additive manufacturing, Acta Mater. 140 (2017) 375–387, https://doi.org/10.1016/j.actamat.2017.08.038.
[311] J.F.S. Markanday, Applications of alloy design to cracking resistance of additively manufactured Ni-based alloys, Mater. Sci. Technol. (United Kingdom). (2022), https://doi.org/10.1080/02670836.2022.2068759.
[312] B.D. Conduit, T. Illston, S. Baker, D.V. Duggappa, S. Harding, H.J. Stone, G.J. Conduit, Probabilistic neural network identification of an alloy for direct laser deposition, Mater. Des. 168 (2019), https://doi.org/10.1016/j.matdes.2019.107644 107644.
[313] Y. Zhang, L. Yang, T. Chen, W. Zhang, X. Huang, J. Dai, Investigation on the optimized heat treatment procedure for laser fabricated IN718 alloy, Opt. Laser Technol. 97 (2017) 172–179, https://doi.org/10.1016/j.optlastec.2017.06.027.
[314] S. Raghavan, B. Zhang, P. Wang, C. Sun, M.L. Sharon, B. Zhang, P. Wang, C. Sun, M.L. Sharon, Effect of different heat treatments on the microstructure and mechanical properties in selective laser melted INCONEL 718 alloy, Mater. Manuf. Process. 32 (2017) 1588–1595, https://doi.org/10.1080/10426914.2016.1257805.
[315] C. Monti, A. Giorgetti, L. Tognarelli, F. Mastromatteo, On the Effects of the Rejuvenation Treatment on Mechanical and Microstructural Properties of IN-

738 Superalloy, J. Mater. Eng. Perform. 26 (2017) 2244–2256, https://doi.org/10.1007/s11665-017-2646-2.
[316] M.M. Kirka, F. Medina, A. Okello, Mechanical behavior of post-processed Inconel 718 manufactured through the electron beam melting process, 680 (2017) 338–346. 10.1016/j.msea.2016.10.069.
[317] Z. Xu, J.W. Murray, C.J. Hyde, A.T. Clare, Effect of post processing on the creep performance of laser powder bed fused Inconel 718 (24) (2018) 486–497, https://doi.org/10.1016/j.addma.2018.10.027.
[318] W. Huang, Z. Wang, J. Yang, H. Yang, X. Zeng, Effects of process parameters and heat treatment on the microstructure and mechanical properties of selective laser melted Inconel 718, Solid Free. Fabr. 2018 Proc. 29th Annu. Int. Solid Free. Fabr. Symp. - An Addit. Manuf. Conf. SFF 2018. (2020) 1268–1276.
[319] Y.L. Kuo, A. Kamigaichi, K. Kakehi, Characterization of Ni-Based Superalloy Built by Selective Laser Melting and Electron Beam Melting, Metall. Mater. Trans. A Phys. Metall. Mater. Sci. 49 (2018) 3831–3837, https://doi.org/10.1007/s11661-018-4769-y.
[320] K. An, L. Yuan, L. Dial, I. Spinelli, A.D. Stoica, Y. Gao, Neutron residual stress measurement and numerical modeling in a curved thin-walled structure by laser powder bed fusion additive manufacturing, Mater. Des. 135 (2017) 122–132, https://doi.org/10.1016/j.matdes.2017.09.018.
[321] X. Wang, K. Chou, The effects of stress relieving heat treatment on the microstructure and residual stress of Inconel 718 fabricated by laser metal powder bed fusion additive manufacturing process, J. Manuf. Process. 48 (2019) 154–163, https://doi.org/10.1016/j.jmapro.2019.10.027.
[322] H. V Atkinson, S. Davies, Fundamental Aspects of Hot Isostatic Pressing : An Overview, m (2000).
[323] W. Tillmann, C. Schaak, J. Nellesen, M. Schaper, M.E. Aydinöz, K. Hoyer, Hot isostatic pressing of IN718 components manufactured by selective laser melting, Addit. Manuf. 13 (2017) 93–102, https://doi.org/10.1016/j.addma.2016.11.006.
[324] G.A. Rao, M. Srinivas, D.S. Sarma, Influence of modified processing on structure and properties of hot isostatically pressed superalloy Inconel 718 (418) (2006) 282–291, https://doi.org/10.1016/j.msea.2005.11.031.
[325] J.H. Boswell, D. Clark, W. Li, M.M. Attallah, Cracking during thermal post-processing of laser powder bed fabricated CM247LC Ni-superalloy, Mater. Des. 174 (2019) 1–12, https://doi.org/10.1016/j.matdes.2019.107793.
[326] S. Das, M. Wohlert, J.J. Beaman, D.L. Bourell, Direct Selective Laser Sintering and Containerless Hot Isostatic Pressing for High Performance Metal Components, Lab. Free. Fabr. (1997) 81–90.
[327] G. Marchese, E. Bassini, A. Aversa, M. Lombardi, D. Ugues, P. Fino, S. Biamino, Microstructural evolution of post-processed Hastelloy X alloy fabricated by laser powder bed fusion, Materials (Basel). 12 (2019), https://doi.org/10.3390/ma12030486.
[328] L.N. Carter, M.M. Attallah, R.C. Reed, Laser powder bed fabrication of nickel-base superalloys: Influence of parameters; characterisation, quantification and mitigation of cracking, Proc. Int. Symp. Superalloys. (2012) 577–586, https://doi.org/10.7449/2012/superalloys_2012_577_586.
[329] B. Ruttert, I. Lopez-Galilea, W. Theisen, An Integrated HIP Heat-Treatment of a Single Crystal Ni-Base Superalloy, in (2020:) 391–399, https://doi.org/10.1007/978-3-030-51834-9_38.
[330] S. Goel, Post-treatment of Alloy 718 produced by electron beam melting, 2019. http://www.diva-portal.org/smash/get/diva2:1289341/FULLTEXT01.pdf.
[331] I. Lopez-Galilea, B. Ruttert, J. He, T. Hammerschmidt, R. Drautz, B. Gault, W. Theisen, Additive manufacturing of CMSX-4 Ni-base superalloy by selective laser melting: Influence of processing parameters and heat treatment, Addit. Manuf. 30 (2019), https://doi.org/10.1016/j.addma.2019.100874 100874.
[332] C. Meid, A. Dennstedt, M. Ramsperger, J. Pistor, B. Ruttert, I. Lopez-Galilea, W. Theisen, C. Körner, M. Bartsch, Effect of heat treatment on the high temperature fatigue life of single crystalline nickel base superalloy additively manufactured by means of selective electron beam melting, Scr. Mater. 168 (2019) 124–128, https://doi.org/10.1016/j.scriptamat.2019.05.002.
[333] L.M. Bortoluci Ormastroni, I. Lopez-Galilea, J. Pistor, B. Ruttert, C. Körner, W. Theisen, P. Villechaise, F. Pedraza, J. Cormier, Very high cycle fatigue durability of an additively manufactured single-crystal Ni-based superalloy, Addit. Manuf. 54 (2022), https://doi.org/10.1016/j.addma.2022.102759.
[334] M. Vilanova, F. Garciandia, S. Sainz, D. Jorge-badiola, T. Guraya, M.S. Sebastian, The limit of hot isostatic pressing for healing cracks present in an additively manufactured nickel superalloy, J. Mater. Process. Tech. 300 (2022), https://doi.org/10.1016/j.jmatprotec.2021.117398 117398.
[335] Z.A. Sentyurina, F.A. Baskov, P.A. Loginov, Y.Y. Kaplanskii, A.V. Mishukov, I.A. Logachev, M.Y. Bychkova, E.A. Levashov, A.I. Logacheva, The effect of hot isostatic pressing and heat treatment on the microstructure and properties of EP741NP nickel alloy manufactured by laser powder bed fusion, Addit. Manuf. 37 (2021), https://doi.org/10.1016/j.addma.2020.101629 101629.
[336] T. Raza, J. Andersson, L.E. Svensson, Microstructure of Selective Laser Melted Alloy 718 in As-Manufactured and Post Heat Treated Condition, Procedia Manuf. 25 (2018) 450–458, https://doi.org/10.1016/j.promfg.2018.06.100.
[337] X. Guo, H. Ling, X. Huang, Effect of HIP treatment on the microstructure and mechanical properties of a Ni-based superalloy fabricated by selective laser melted method, J. Phys. Conf. Ser. 1605 (2020), https://doi.org/10.1088/1742-6596/1605/1/012143.
[338] D.S. Watring, K.C. Carter, D. Crouse, B. Raeymaekers, A.D. Spear, Mechanisms driving high-cycle fatigue life of as-built Inconel 718 processed by laser powder bed fusion, Mater. Sci. Eng. A. 761 (2019), https://doi.org/10.1016/j.msea.2019.06.003 137993.
[339] T. Guraya, S. Singamneni, Z.W. Chen, Microstructure formed during selective laser melting of IN738LC in keyhole mode, J. Alloys Compd. 792 (2019) 151–160, https://doi.org/10.1016/j.jallcom.2019.03.419.
[340] X. Liu, Z. Liu, L. Zhang, Q. Zhao, Q. Jiang, Increased tensile strength and elongation of the Ni–Fe based polycrystalline cast superalloy via the trace addition of TiC nanoparticles, Mater. Sci. Eng. A. 827 (2021), https://doi.org/10.1016/j.msea.2021.141988 141988.
[341] C. Hong, D. Gu, D. Dai, M. Alkhayat, W. Urban, P. Yuan, S. Cao, A. Gasser, A. Weisheit, I. Kelbassa, M. Zhong, R. Poprawe, Laser additive manufacturing of ultrafine TiC particle reinforced Inconel 625 based composite parts: Tailored microstructures and enhanced performance, Mater. Sci. Eng. A. 635 (2015) 118–128, https://doi.org/10.1016/j.msea.2015.03.043.
[342] Z. Chen, P. Wei, S. Zhang, B. Lu, L. Zhang, X. Yang, K. Huang, Y. Huang, X. Li, Q. Zhao, Graphene reinforced nickel-based superalloy composites fabricated by additive manufacturing, Mater. Sci. Eng. A. 769 (2020), https://doi.org/10.1016/j.msea.2019.138484 138484.
[343] D. Tiparti, I.T. Ho, K.C. Chang, T.H. Hsu, A.C. Yeh, S. Tin, Understanding the Effects of CoAl2O4 Inoculant Additions on Microstructure in Additively Manufactured Inconel 718 Processed Via Selective Laser Melting, Metall. Mater. Trans. A Phys. Metall. Mater. Sci. 52 (2021) 2630–2641, https://doi.org/10.1007/s11661-021-06255-z.
[344] C.L. Frederick, Control of Grain Structure in Selective-Electron Beam Melting of Nickel-based Superalloys, University of Tennessee, 2018.
[345] C. Shen, Z. Pan, D. Cuiuri, D. Ding, H. Li, Influences of deposition current and interpass temperature to the Fe3Al-based iron aluminide fabricated using wire-arc additive manufacturing process, Int. J. Adv. Manuf. Technol. 88 (2017) 2009–2018, https://doi.org/10.1007/s00170-016-8935-3.
[346] G. Mohr, S.J. Altenburg, K. Hilgenberg, Effects of inter layer time and build height on resulting properties of 316L stainless steel processed by laser powder bed fusion, Addit. Manuf. 32 (2020), https://doi.org/10.1016/j.addma.2020.101080 101080.
[347] C. Guévenoux, S. Hallais, A. Charles, E. Charkaluk, A. Constantinescu, Influence of interlayer dwell time on the microstructure of Inconel 718 Laser Cladded components, Opt. Laser Technol. 128 (2020), https://doi.org/10.1016/j.optlastec.2020.106218 106218.
[348] A. Mehmeti, P. Bidare, S. Imbrogno, D. Wimpenny, K. Essa, S. Dimov, Surface integrity of hybrid CM247LC/Inconel 718 components produced by laser-directed energy deposition, Int. J. Adv. Manuf. Technol. 121 (2022) 4961–4980, https://doi.org/10.1007/s00170-022-09605-2.
[349] H. Zhao, G. Zhang, Z. Yin, L. Wu, Effects of Interpass Idle Time on Thermal Stresses in Multipass Multilayer Weld-Based Rapid Prototyping, J. Manuf. Sci. Eng. 135 (2013), https://doi.org/10.1115/1.4023363.
[350] C. Zhang, Z. Qiu, H. Zhu, Z. Wang, O. Muránsky, M. Ionescu, Z. Pan, J. Xi, H. Li, On the effect of heat input and interpass temperature on the performance of inconel 625 alloy deposited using wire arc additive manufacturing–cold metal transfer process, Metals (Basel). 12 (2022) 1–16, https://doi.org/10.3390/met12010046.
[351] W. Wu, Influence of vibration frequency on solidification of weldments, Scr. Mater. 42 (2000) 661–665, https://doi.org/10.1016/S1359-6462(99)00416-9.
[352] T. Watanabe, M. Shiroki, A. Yanagisawa, T. Sasaki, Improvement of mechanical properties of ferritic stainless steel weld metal by ultrasonic vibration, J. Mater. Process. Technol. 210 (2010) 1646–1651, https://doi.org/10.1016/j.jmatprotec.2010.05.015.
[353] R. Thavamani, V. Balusamy, J. Nampoothiri, R. Subramanian, K.R. Ravi, Mitigation of hot cracking in Inconel 718 superalloy by ultrasonic vibration during gas tungsten arc welding, J. Alloys Compd. 740 (2018) 870–878, https://doi.org/10.1016/j.jallcom.2017.12.295.
[354] K. Sivaprasad, S.G.S. Raman, Influence of magnetic arc oscillation and current pulsing on fatigue behavior of alloy 718 TIG weldments, Mater. Sci. Eng. A. 448 (2007) 120–127, https://doi.org/10.1016/j.msea.2006.10.048.
[355] Q. Li, Y. Zhang, J. Chen, B. Guo, W. Wang, Y. Jing, Y. Liu, Effect of ultrasonic micro-forging treatment on microstructure and mechanical properties of GH3039 superalloy processed by directed energy deposition, J. Mater. Sci. Technol. 70 (2021) 185–196, https://doi.org/10.1016/j.jmst.2020.09.001.
[356] F. Ning, Y. Hu, Z. Liu, W. Cong, Y. Li, X. Wang, Ultrasonic Vibration-Assisted Laser Engineered Net Shaping of Inconel 718 Parts: A Feasibility Study, Procedia Manuf. 10 (2017) 771–778, https://doi.org/10.1016/j.promfg.2017.07.074.
[357] A. Reichardt, A.A. Shapiro, R. Otis, R.P. Dillon, J.P. Borgonia, B.W. McEnerney, P. Hosemann, A.M. Beese, Advances in additive manufacturing of metal-based functionally graded materials, Int. Mater. Rev. 66 (2021) 1–29, https://doi.org/10.1080/09506608.2019.1709354.
[358] L.D. Bobbio, B. Bocklund, A. Reichardt, R. Otis, J.P. Borgonia, R.P. Dillon, A.A. Shapiro, B.W. McEnerney, P. Hosemann, Z.K. Liu, A.M. Beese, Analysis of formation and growth of the σ phase in additively manufactured functionally graded materials, J. Alloys Compd. 814 (2020), https://doi.org/10.1016/j.jallcom.2019.151729.
[359] J.S. Zuback, T.A. Palmer, T. DebRoy, Additive manufacturing of functionally graded transition joints between ferritic and austenitic alloys, J. Alloys Compd. 770 (2019) 995–1003, https://doi.org/10.1016/j.jallcom.2018.08.197.